SCUOLA NORMALE SUPERIORE

PH. D. THESIS

Interlaced biophysical methods to unveil membrane receptor organization

Barbara Storti

ADVISOR

Dr. Ranieri Bizzarri

2016

To Irene and Lisa

Foreword

This thesis is the result of my research activity at the NEST laborarory of Scuola Normale Superiore in Pisa: I began my studies on the membrane receptor issue in 2007, prompted by the group interest in intracellular nanobiophysics. This research was carried out within a joint PhD program sponsored by Scuola Normale Superiore and Italian Institute of Technology.

SCUOLA
NORMALE
SUPERIORE

ISTITUTO
ITALIANO DI
TECNOLOGIA

List of publications

Abbruzzetti S, Bizzarri R, Luin S, Nifosi R, Storti B, Viappiani C, and Beltram F (2010) Photoswitching of E222Q GFP mutants: "concerted" mechanism of chromophore isomerization and protonation. *Photochem Photobiol Sci* 9(10):1307-1319.

Storti B, Bizzarri R, Cardarelli F, and Beltram F (2012) Intact microtubules preserve transient receptor potential vanilloid 1 (TRPV1) functionality through receptor binding. *J Biol Chem* 287(10):7803-7811.

Storti B, Di Rienzo C, Cardarelli F, Bizzarri R, and Beltram F (2015) Unveiling TRPV1 spatio-temporal organization in live cell membranes. PLoS ONE 10(3):e0116900.

Publications not included in this thesis:

Signore G, Nifosi R, Albertazzi L, Storti B, and Bizzarri R (2010) Polarity-sensitive coumarins tailored to live cell imaging. *J Am Chem Soc* 132(4):1276-1288.

Albertazzi L, Storti B, Marchetti L, and Beltram F (2010) Delivery and subcellular targeting of dendrimer-based fluorescent pH sensors in living cells. *J Am Chem Soc* 132(51):18158-18167.

Albertazzi L, Brondi M, Pavan G M, Sato S S, Signore G, Storti B, Ratto G M, and Beltram F (2011) Dendrimer-based fluorescent indicators: in vitro and in vivo applications. *PLoS One* 6(12):e28450

Battisti A, Digman M A, Gratton E, Storti B, Beltram F, and Bizzarri R (2012) Intracellular pH measurements made simple by fluorescent protein probes and the phasor approach to fluorescence lifetime imaging. *Chem Commun (Camb)* 48(42):5127-5129.

Signore G, Abbandonato G, Storti B, Stockl M, Subramaniam V, and Bizzarri R (2013) Imaging the static dielectric constant in vitro and in living cells by a bioconjugable GFP chromophore analog. *Chem Commun* 49(17):1723-1725.

Albertazzi L, Storti B, Brondi M, Sulis Sato S, Ratto G M, Signore G and Beltram F (2013) Synthesis, Cellular Delivery and *In vivo* Application of Dendrimer-based pH Sensors. *J. Vis. Exp.* (79), e50545, doi:10.3791/50545.

Koenig M, Storti B, Bizzarri R, Guldi D M, Brancato G, and Bottari G (2016) A fluorescent molecular rotor showing vapochromism, aggregation-induced emission, and environmental sensing in living cells *J. Mat. Chem. D* Accepted DOI: 10.1039/C5TC03541D

Table of Contents

Introduction

Cellular plasma membrane is not just a barrier separating inner and outer cellular volumes but it is critical for communication with the extracellular milieu. Indeed, the plasma membrane enables the transfer of many compounds important for the cell metabolism and for chemical and electrical signaling. The capsaicin receptor (Transient Potential Vanilloid 1 or TRPV1) belongs to the fascinating class of polymodal membrane receptors that integrate several physical and molecular stimuli and translate them into intracellular signaling. More specifically, TRPV1 is a nonselective voltage-dependent, temperature-dependent, ligand-dependent cation channel with a preference for Ca^{2+}. Modulators of TRPV1 activity include: noxious heat, low pH, capsaicin, and capsaicin analogues like resiniferatoxin (RTX). TRPV1 is expressed both in sensory neurons, where it is involved in pain signaling, and in many other cell types (e.g. endothelial cells). The research on TRPV1 is driven by its important biological role, but it is also believed that TRPV1 activation mechanism could be relevant to the discovery and design of drugs capable of controlling TRPV1 activity and therefore pain stress in humans. Surprisingly, many molecular properties of TRPV1 are still largely unknown.

Among the unclear aspects of TRPV1 activity, a hot topic is represented by its interactions with the cytoskeleton. TRPV1 was recently proposed to bind to microtubule β-tubulin. Activation of TRPV1 was demonstrated to yield fast disassembly of microtubules, albeit at agonist concentrations much above saturation. This suggests that TRPV1 may regulate some specific cell functions (and possibly neuronal functions) through cytoskeleton reshaping. Yet, the alleged direct binding of TRPV1 to microtubules raises the question: do microtubules also modulate TRPV1 activity? If so, the microtubule-TRPV1 interplay may play a role in tuning cell response to TRPV1 activation upon different factors including noxious stimuli.

The activation of the TRPV1 due to noxious stimulation is followed by the attenuation of nociceptive sensory neuron excitability, making nociceptors partially or totally refractory to subsequent stimuli. Available knowledge is limited to acute,

Ca^{2+}-dependent, desensitization. Conversely, long-term TRPV1 desensitization mechanisms are largely unknown. It was speculated that long-term desensitization could involve TRPV1 withdrawal from the cell surface. Indeed, similar to members of other receptor families, activity-dependent control of plasma membrane-resident receptors may involve TRPV1 endocytosis followed either by receptor recycling to the plasma membrane or by its degradation through the proteosomal or lysosomal pathways. A recent study showed that agonist stimulation promoted receptor internalization via a clathrin-independent endocytotic mechanism. The classical alternative to clathrin-dependent endocytosis of protein is represented by caveolar endocytosis, which is in turn is modulated by lipid rafts, membrane microdomains enriched in cholesterol and saturated lipids. Interestingly, several members of the TRP family were demonstrated to reside near caveolin-1, the main structural protein of caveolae. Thus, I may question whether caveolin-1 is implied in the clathrin-free endocytosis of TRPV1. If so, TRPV1 dynamics and interactions could be influenced by membrane raft regions.

Answering these questions requires high-resolution / high-sensitivity imaging of the receptor to account for its specific dynamics and interaction interplay. In my thesis I set out to address these issues by a toolbox of fluorescence imaging techniques such as Förster Resonance Energy Transfer, Fluorescence Anisotropy Imaging, and Spatio-temporal image correlation spectroscopy. I investigated receptor properties such as membrane mobility, microtubule and caveolin-1 binding, and TRPV1 oligomerization status. My experimental strategies benefited from the use of genetically-encodable fluorescent reporters belonging to the green fluorescent protein family.

The thesis is organized as follow:

- In ***Chapter 1*** I provide a brief review of the biological context of TRPV1, namely the cell plasma membrane. This is important for the full understanding of biological and biophysical aspects of receptor functionality. For this reason I focus on membrane organization with a particular regard to all compartments that may be implied in the regulation of TRPV1.

- In ***Chapter 2*** I introduce all the common tools shared by the imaging methods that were employed in this thesis work. In particular, the chapter presents a short overview on fluorescence microscopy and genetically-encoded fluorescent proteins.

- ***Chapter 3*** is the first chapter dealing with my experimental results. There I present the study of the binding interactions of the TRPV1 receptor in living cells revealed by Förster Resonance Energy Transfer (FRET). A first part of the chapter is devoted to a short description of the FRET imaging technique, whereas in the second part I describe the FRET analysis to reveal that TRPV1 and tubulin mutually interact in the membrane of living cells at rest and under agonist stimulation. Conversely, nocodazole-induced disassembly of microtubules abolishes the FRET signal, indicating the dissociation of TRPV1-microtubule complex. Similarly, FRET analysis demonstrates the binding interaction between TRPV1 and caveolin-1 at rest. Complementary colocalization studies demonstrate that agonist stimulation of the receptor triggers its internalization by caveolar endocytosis.

- In ***Chapter 4*** I show that temporal Image Correlation Spectroscopy (tICS) reveals the average temporal dynamics of membrane TRPV1. tICS is a method based on the correlation analysis of fluorescence fluctuations recorded in the presence of a few moving molecules imaged in a micron-size area. The general features of tICS are described at the beginning of the chapter. Then, I report tICS measurements on TRPV1 alone. I demonstrate that, at basal conditions, TRPV1 dynamics comprises two components with rather different membrane diffusion (fast- and slow-moving pools). Depolymerization of microtubules yields a significant fraction of immobile and aggregated receptor. In the last part of the chapter I describe the combined use of tICS and FRET to identify and to characterize the receptor pool that interacts with microtubules. These experiments show that only the slow-moving TRPV1 pool bind to microtubules, at both basal and agonist-stimulated conditions.

- In ***Chapter 5*** the oligomerization degree of membrane TRPV1 is investigated at basal state or under agonist stimulation. In particular, I describe two complementary techniques: fluorescence anisotropy imaging (FAIM) associated to homo-FRET, and fluctuation analysis (Number and Brightness, abbreviated as N&B). The general aspects of both techniques are discussed prior to describe the experimental data. Our results suggest that TRPV1 likely exists in both a dimer, immature, form, and a tetrameric functional form stabilized by intact microtubules. Microtubules

depolymerization leads to significant increase of the oligomerization degree of the receptor (and a concomitant reduction of the efficiency as ion channel).

- In ***Chapter 6*** I present a comprehensive description of TRPV1 dynamics and microtubule/caveolin interactions obtained by Spatio-Temporal Correlation Spectroscopy (STICS). STICS is a fluorescence fluctuation technique that permits to quantify both the diffusion regime and its quantitative aspects. In particular I applied a novel data interpretation approach that has been recently developed at NEST lab: *i*MSD analysis. *i*MSD is suitable for determining diffusion laws of integral membrane proteins in live cells with high temporal and spatial resolution and no need for the preliminary assumption of a specific interpretative model. At the beginning of the chapter I describe the general aspects of *i*MSD. Then, I focus on the experimental results obtained by applying *i*MSD to the imaging of TRPV1. I demonstrate that basal TRPV1 is mainly split into three populations with rather different properties: 1) a fraction binding to caveolin-1 and therefore confined in caveolar structures, 2) a fraction residing in large, raft-enriched membrane patches whose diffusion is actively modulated by microtubules through selective binding, and 3) a fast isotropically-diffusing fraction. Remarkably, the last pool shows a non-negligible correlation between its relative abundance and the cell expression level of the receptor. This feature suggests its identification with an “immature” form of TRPV1 that acts as “reservoir” of the receptor. In light of previous data on endocytic internalization of TRPV1, I interpret the binding of TRPV1 to caveolin-1 as a biological means to trigger long-term desensitization of the receptor via caveolar endocytosis. It is worth noting that the TRPV1 binding to caveolin-1 is reversible with a characteristic binding time of several seconds. Conversely, the complex of TRPV1 with microtubule does not dissociate within one minute and it appears to move within the membrane in rather large patches with 800-900 nm size. This system is characterized by a motion actively driven by microtubule chains. The "guided" diffusion disappears when microtubules are disassembled. These findings support the identification of microtubules as the essential modulators of TRPV1 activity.

- In ***Chapter 7*** I recast all my data into a model accounting for the molecular interplay among TRPV1, microtubules, and caveolin-1.
- In ***Appendix A*** I present the mathematical background of spatio-temporal correlation spectroscopy and *i*MSD analysis.
- In ***Appendix B*** I present a new approach to obtain images of TRPV1 on the cell membrane with spatial resolution below the optical diffraction barrier. This was made possible by the use of a novel photochromic fluorescent protein, EYQ1, which I contributed to develop and study.

Chapter

1

Biological background

1.1 Organization of the plasma membrane and its functional role

According to the fluid mosaic model proposed by Singer and Nicolson in 1972 (1), the cellular plasma membrane is a two-dimensional liquid where lipid and protein molecules are mixed like a mosaic. Yet, in the last twenty years the fluid mosaic model picture of the membrane bilayer has been seriously challenged by many experiments. For instance, if the Singer–Nicolson model were true, then membrane molecules would always be undergoing simple Brownian diffusion. Several studies, however, continue to uncover evidences showing that this is not the case (2). Additionally, it is recognized that the plasma membrane is a major platform for signal transduction, since it influences how external signals are conveyed into cells' interior by membrane protein receptors. Here, the fluid mosaic model fails in describing the weak and dynamic association of membrane proteins into complexes involved in signal transduction, as well as their heterogeneous distribution across the bilayer. The failure of the Singer-Nicolson model has led to a more accurate description of cell membrane, which takes into account the spatial heterogeneity of the bilayer.

The size of membrane domains with functional roles spans from 2 to 300 nm. In this spatial scale (usually referred to as *mesoscale*) the plasma membrane exhibits transient hierarchical dynamic substructures, all forming and disassembling with

various characteristic times. These mesostructures play key roles in modulating signal transduction processes across the membrane. For example, receptor oligomerization is enhanced by membrane compartmentalization, since the formation of transient protein-protein and protein-lipid complexes generates temporary signaling platforms or reaction chambers. This effect is also believed to prime the place where the extracellular signal was originally received (for 1 s to 1 min). Therefore, the comprehension of any molecular signaling process occurring across the plasma membrane requires the description of the heterogeneous structure of the bilayer.

Current knowledge identifies three hierarchically-ordered domains at mesoscale, which are depicted in Fig. 1.1. Starting from the largest one (first tier), the plasma membrane is partitioned into *actin membrane-skeleton-induced compartments*, with size of 40-300 nm. At the second tier in the hierarchy we find *raft domains*, with average size of 2-20 nm. Rafts are generated by the affinitiy between lipids and proteins, and their size and composition can be modulated by stimulation of membrane receptors (which are in turn involved in signal transduction and molecular trafficking). *Dynamic protein assemblies* of 3-10 nm constitute the smallest domains (third tier), although some protein complexes reach few hundred nm, as in the cases of clathrin-coated pits. In the following the main features of each tier are described in some detail.

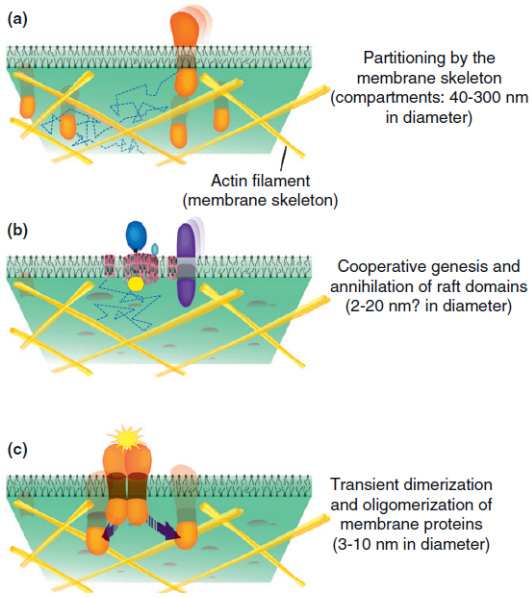

Figure 1.1. Three-tiered hierarchical structure of mesoscale domains in the plasma membrane. (a) Partitioning of the entire plasma membrane by the membrane-associated actin-based membrane skeleton (fence) and TM proteins anchored to the membrane skeleton fence (pickets). (b) Cholesterol-containing raft domains, with sizes limited by the membrane compartments. (c) Dimers and greater oligomers of membrane associated and integral membrane proteins, which might exist only transiently. (Adapted from (3))

1.1.1 The first tier: actin membrane-skeleton-induced compartments

Membrane compartments of 40–300 nm size are created by the interactions of the bilayer with actin-based membrane skeleton (fence) and transmembrane proteins (TM) anchored to the membrane-skeleton fence (pickets) (Fig. 1.2). In fact, most membrane proteins were demonstrated to undergo short-term confined diffusion within a compartment and long term hop movement between compartments (hop diffusion) (4). This phenomenon is rationalized by the collision of protein cytoplasmic domains with the actin-based membrane skeleton, inducing their temporary confinement or corralling within the membrane skeleton mesh (Fig. 1.2A).

This “membrane skeleton fence” model is integrated with the presence of transmembrane proteins anchored to, and aligned along, the membrane skeleton, thereby acting as rows of pickets against the free diffusion of phospholipids (Fig. 1.2B) (5-7). Notably, the diffusion within any of these compartments (short-range diffusion) is as fast as in artificial lipid membranes. Yet, the hop diffusion between adjacent compartments accounts for the 20-fold decrease in long-range molecular diffusion within plasma membrane as compared to artificial lipid membranes (8).

1.1.2 The second tier: raft domains

The plasma membrane is a mixture of several molecules with differing mutual miscibility. Some of them associate to yield transient complexes, with sizes and lifetimes based on the competition between thermal fluctuations and molecular affinities. These transient associations are enhanced by poor molecular miscibility. For example, cholesterol is not readily miscible with unsaturated alkyl chains, owing to the steric incompatibility between its rigid, bulky tetracyclic sterol backbone and the rigid, mandatorily-bent *cis*-double bonds of the unsaturated phospholipids (9-12) (Fig. 1.3 a and b,i). Accordingly, small clusters of several cholesterol molecules with lifetimes of 1–100 ns can be observed in unsaturated lipid domains (10,12) (Fig. 1.3c).

In the presence of domains enriched in saturated alkyl chains of glycosylphosphatidylinositol (GPI)-anchored proteins (GPI-AR), glycosphingolipids and sphingomyelin, a segregation process may take place and cholesterol comes off the unsaturated lipid domains to form transient complexes with the saturated alkyl moieties. These domains are called *lipid rafts* and are characterized by a wide range of characteristic lifetime, owing to the variability of multi-molecular interactions.

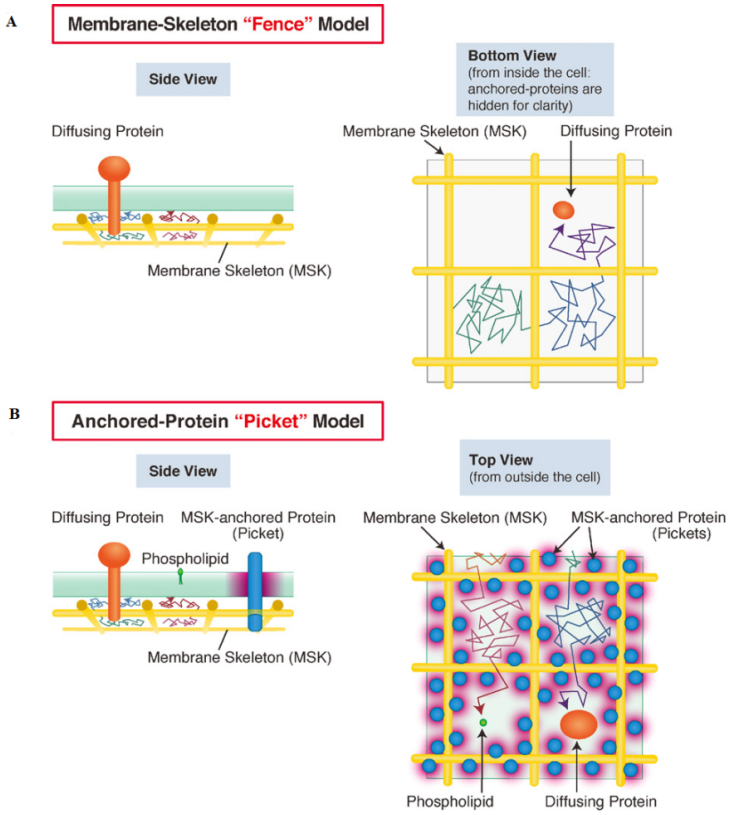

Figure 1.2 The membrane-skeleton fence model and the anchored TM protein picket model. The left column shows the side view (longitudinal cross-section) of the membrane, while the right column shows the bottom view (from the cytoplasm, A) and the top view (from outside the cell, B). In the anchored protein picket model (B), the diffusion of molecules around immobilized proteins (red region) is slower, owing to the hydrodynamic-friction-like-effect at the surface of the immobilized protein. This effect could propagate over distances equivalent to multiple diameters of picket proteins. When such diffusion barriers are aligned along the membrane-skeleton fence, they form effective compartment boundaries. (Adapted from (13)).

Each observation method of lipid-rafts is inevitably related to specific time and space scales and can therefore probe only limited subsets of rafts among those actually occurring in the membrane.

Cytoskeleton-induced membrane compartments and raft domains coexist in the plasma membrane (Fig. 1.1). According to the anchored-protein picket model, the

TM protein pickets induce the temporary confinement of phospholipids, GPI-anchored proteins and TM proteins in the mesh. The TM protein pickets exclude cholesterol from the first annulus in the membrane (Fig. 1.3d), owing to the structural incompatibility between the TM protein surface and bulky cholesterol (9,14). Therefore, the upper size limit of raft domains is slightly less than those of membrane compartments segmented by actin cytoskeleton. This limit is particularly relevant from a biological point of view, on account of the raft propensity to coalesce upon extracellular stimulation (e.g. crosslinking of the ganglioside GM1 by the B subunit of cholera toxin (15,16)).

1.1.3 The third tier: dynamic protein complex domains

The third tier comprises dynamic assemblies of membrane proteins. The stoichiometry of these complexes spans from dimers to oligomers, and they associate and dissociate with time constants in the millisecond range. The formation of molecular complexes is facilitated by membrane compartments delimited by fence and pickets. In fact, once two molecules enter the same compartment, they reside there for a long time (1-100 ms) before hop diffusion will displace them apart. This phenomenon increases the frequency of binding encounters. Once formed, also the molecular complex becomes trapped within compartments. Thus, the first tier of membrane organization is tightly coupled to the third tier. A similar mechanism accounts for the coupling between the second and third tiers of membrane organization (2,17,18). Indeed, ligand-induced GPI-AR homodimers can be aggregation nuclei to assemble cholesterol and other saturated lipids. This leads to aggregates or transient heterocomplexes with TM scaffolding proteins, a relevant feature of downstream signaling (19). According to this molecular framework, signal transduction processes are modulated by the interaction of the third tier with rafts and cytoskeleton-induced membrane compartments.

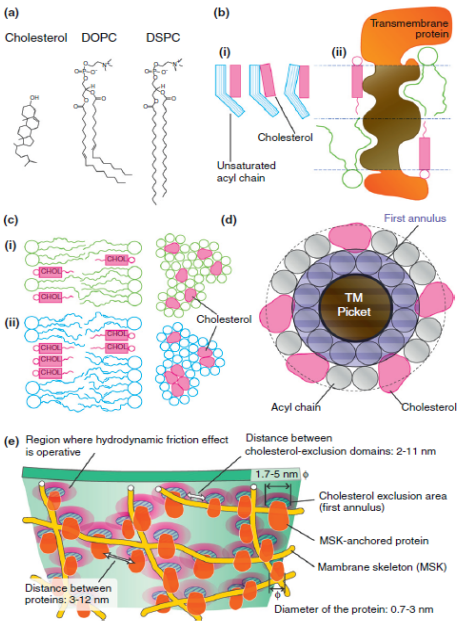

Figure 1.3 The mechanism by which raft domains are excluded from compartment boundaries. (a) Chemical structures of cholesterol, a typical saturated phospholipid (L-α-distearoylphosphatidylcholine, DSPC), and a typical unsaturated phospholipid (L-α-dioleoylphosphatidylcholine, DOPC). (b) Non-conformability of the rigid ring structure of cholesterol (rectangles) with the rigid, mandatory bend at the C9–C10 cis-double bond in the unsaturated alkyl chain (bent rods, i) and with the rough surface of the TM domain of TM proteins (ii), which generates vacant pockets (packing defects) in the membrane. In (i), three possible configurations placing cholesterol and an unsaturated chain next to each other are indicated, but none shows good packing. The TM proteins with raft affinities are expected to be well miscible with cholesterol. (c) Schematic snapshot drawings of the membrane domains enriched in saturated lipids and cholesterol (i) or unsaturated lipids and cholesterol (ii). Cross-section (top views) of the membrane are also shown. In the top view, open circles represent alkyl chains and solid structures indicate cholesterol molecules (20). Note that cholesterol tends to be segregated out of the domains of unsaturated lipids, forming small clusters of several cholesterol molecules with lifetimes of 1–100 ns, whereas it mixes with saturated lipids, and particularly well at cholesterol:phospholipid molar ratios of 1:1, 1:2 and 1:4. (d) Likewise, cholesterol is excluded from the 'first annulus' of the TM domain of the picket protein, owing to the steric incompatibility as shown in (b,i). (e) The majority of raft domains would be contained within a compartment rather than spread across the compartment boundaries, because the compartment boundaries are probably formed by cholesterol-excluding zones (first annular lipids or boundary lipids, shown by diagonal lines) of 1.7–5 nm in diameter (surrounding the TM picket proteins) located 2–11 nm away from each other. (Adapted from (3))

Importantly, signal transduction is finely tuned by the establishment of multi-molecular assemblies in/on the plasma membrane, beside the classical bimolecular collision or interaction of two protein partners (21-23). In this context, much attention is given to the role of coat and scaffolding proteins in signal transduction. Coat proteins such as caveolin-1, and scaffolding proteins such as tubulin, were recognized to modulate subtly the function of several receptors, including some proteins belonging to the TRP family (24,25). Given their relevance in this work, the role of caveolin-1 and tubulin in plasma membrane organization and function are sketched in the next two paragraphs.

1.1.4 Caveolae as plasma membrane nanodomains

Caveolae are submicroscopic, plasma membrane pits with a size of about 60–80 nm that are abundant in many mammalian cell types. Caveolae are extremely widespread and abundant among several cell type, including smooth-muscle cells, fibroblasts, endothelial cells, and adipocytes. Caveolae were recognized as relevant for endocytosis, transcytosis, calcium signaling, and numerous other signal transduction events (26,27). The main structural features of caveolae are summarized in Fig. 1.4. The integral membrane protein family of caveolins has been the main focus of caveolae research, and caveolins are undisputedly the best markers of caveolae since their discovery (28,29). There are three mammalian caveolins that form caveolae: CAV1, CAV2 and CAV3. CAV1 and CAV2 are generally expressed together in cells other than skeletal muscle, whereas CAV3 is predominantly expressed in striated muscle. The fundamental role of caveolins in driving membrane curvature of caveolar vesicles was shown by their expression in prokaryotic hosts lacking any intracellular membrane systems (30). Furthermore, caveolins reside in regions of the membrane whose lipid composition is similar to membrane rafts. The relative amount of cholesterol in caveolae may be more than 100 times higher than the bilayer average, reaching as much as 20,000 molecules in immuno-isolated caveolae (31). Some glycosphingolipids (for example, GM1 and GM3) and sphingomyelin are also enriched in caveolae as compared to the bulk plasma membrane.

Several receptor proteins, including G protein-coupled receptors (GPCRs) and ion channels belonging to the TRP family are known to coexist with caveolin in caveolae (32-34). Indeed, one of the most important roles of caveolae is to colocalize receptors and effectors within microdomains (35,36). The second

important role of caveolae is the internalization via endocytosis, although many issues are still controversial in this field (37-39).

Electron microscopy revealed complex interactions between caveolae and the cytoskeleton (40). Microtubules promote trafficking of caveolae forth and back from the cell surface. This is thought to occur through local stabilization of microtubules by β1 integrins and integrin-linked kinase (ILK) signaling (41).

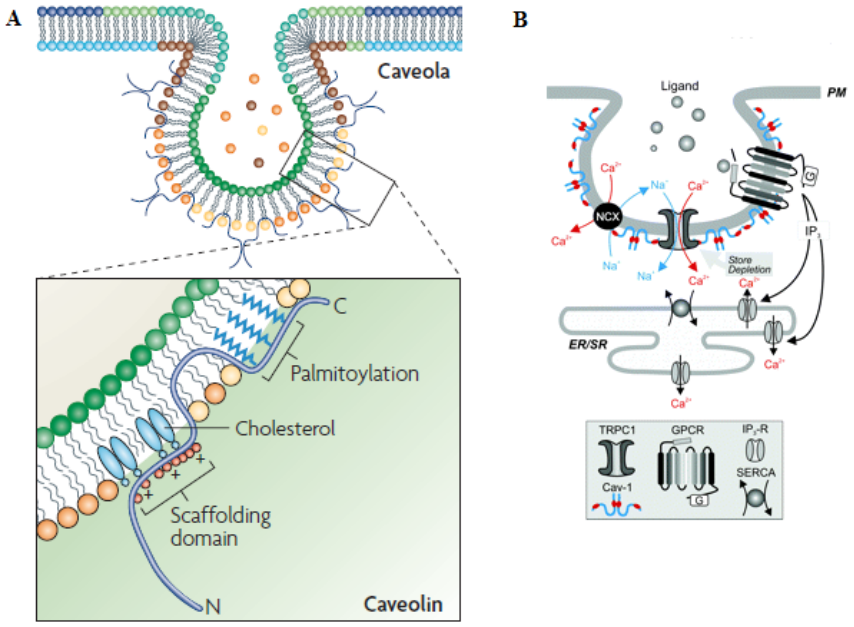

Figure 1.4 Caveolae and caveolins. (A) Caveolin-1 is inserted into the caveolar membrane, with the N and C termini facing the cytoplasm and a putative 'hairpin' intramembrane domain embedded within the membrane bilayer. The scaffolding domain, a highly conserved region of caveolin, might have a role in cholesterol interactions through conserved basic (+) and bulky hydrophobic residues (red circles). The C-terminal domain, which is close to the intramembrane domain, is modified by palmitoyl groups that insert into the lipid bilayer. (B) Schematic diagram depicting the caveolin-1 and some receptor and ion channel participating in caveolae protein complex formation. (Adapted from (38))

1.1.5 Tubulin and microtubules as modulators of membrane and membrane receptors

Tubulin is an abundant, hydrophilic, heterodimeric protein that is present in all eukaryotes. It is the chief component of microtubules, ciliary axonemes, basal bodies, and centrioles. The bulk of tubulin consists of a dimeric assembly of two similar but not identical subunits, α- and β- tubulin. αβ-tubulin heterodimers are protein scaffolds of about 4.6 nm × 8.0 nm × 6.5 nm size (42). The head-to-tail association ("polymerization") of the αβ-tubulin heterodimers yields microtubule protofilament. A single microtubule comprises 10–15 protofilaments, each one made of dimers that associate laterally to form a 24 nm wide hollow cylinder (43). The lateral interaction between subunits of adjacent protofilaments was described as a B-type lattice with a seam (long arrow, Fig. 1.5A). A third tubulin isoform, γ-tubulin, is the template for the correct assembly of microtubules (43).

Microtubules undergo cycles of rapid growth and disassembly. This is known as dynamic instability and was observed both *in vitro* and *in* vivo (44,45). Individual microtubules do not reach a steady-state length, but exist in either polymerization (growth) or depolymerization (shrinkage) states. Notably, the two ends of each microtubule chain are characterized by two different growing/disassembly rates. This non-equilibrium state depends on the binding of GTP at the nucleotide exchangeable site (E site) on β-tubulin during polymerization. The polymerization dynamics of microtubules is central to their biological function: (a) microtubules can rapidly reorganize in order to differentiate spatially and temporally in accordance with the cell context (46), and (b) pushing and pulling forces are established during polymerization and depolymerization, respectively (47).

The interaction of tubulin with biological membranes has been investigated since the pioneeristic study of Blitz and Fine forty years ago (48). Tubulin can bind directly to membrane lipids, and is called in this case "membrane tubulin". The interaction between the microtubules and the plasma membrane was also confirmed by electron microscopy studies (49). The apparent affinity constant measured for tubulin-membrane interaction is 1.5-3.0 x 10^7 M^{-1} (by observing the tubulin-binding affinity of erythrocyte membranes known to be devoid of membrane tubulin (50)). This implies that tubulin interaction with the membrane can be observed at physiological concentrations within cells. This affinity constant is much lower than concentration of tubulin dimers able to trigger polymerization. Additionally, the direct interaction of tubulin and/or microtubules with several trans-membrane

proteins such as ion channels and G-protein coupled receptors (51) was repeatedly assessed. These findings led to the qualitative concept of sub-membranous microtubule cytoskeleton. Yet, no general features of tubulin-mediated receptor function have been highlighted insofar.

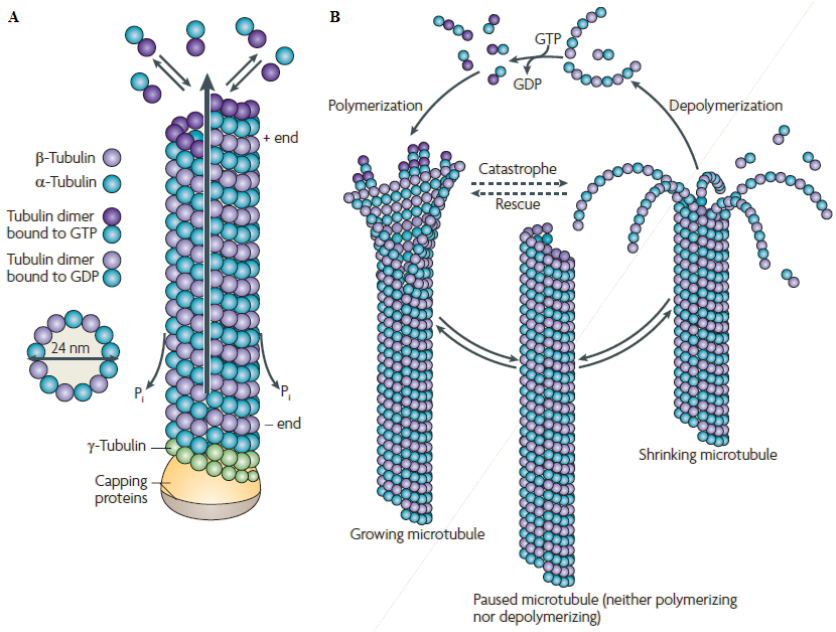

Figure 1.5. Microtubules dynamics. (A) *S*tructure of microtubules. (B) Cycle of polymerization and depolymerization of microtubules. (Adapted from (43))

1.2 Membrane-modulated neurotransmitter signaling: Transient Receptor Potential Vanilloid 1 (TRPV1)

Recently, several studies highlighted the pivotal role of membrane heterogeneity for signal transduction in neurons and other cells of the nervous system (52). Coherently with the new hierarchical vision of membrane structure, the most recent models of neurotransmission attribute great relevance to the arrangement of

signaling molecules in nanodomains to either increase or dampen signaling. In this context, some of the most interesting results concern the interplay between lipid rafts, coat proteins such caveolins, and cytoskeletal components. This interaction is relevant since, in several cases, neurotransmitter signaling is associated with cytoskeletal modification (52). This effect provides a feedback to finely tune the signaling response, besides affecting the global cell morphology. Actually, tubulin and microtubules were early recognized as dynamic partners of many neurotransmitters and they are thought to help sequestering and anchoring specific neurosignaling proteins in raft domains (53-55).

The regulating role of membrane heterogeneity appears particularly intriguing when receptors that integrate a large number of stimuli come into play. In this context, the components of the Transient Receptor Potential (TRP) cation channel family are among the most interesting examples of signal integrators that may be modulated by membrane features. Beside voltage, TRP channels are activated by a wide range of stimuli including intra- and extracellular ligands, temperature, and osmotic stress (56). Membrane state, composition, and compartmentalization were demonstrated to influence the gating behavior of several TRP channels (57). Some members of the TRP family form signal complexes in lipid rafts (32). TRPC1 (transient receptor potential channel 1) is regulated by caveolin-1, and caveolae account for its exocytic trafficking on plasma membrane(58). Phosphatidylinositol 4,5-bisphosphate (PIP2), a lipid found mostly in raft regions (59), is believed to regulate strongly the activation and de-sensitation of many components of the TRP family (60).

Intriguingly, little is known on the interplay between membrane features and the Transient Receptor Potential Vanilloid 1 (TRPV1), also known as the capsaicin receptor. TRPV1 is a nonselective voltage-dependent cation channel (with preference for Ca^{2+}) that is expressed in sensory neurons and in many other cell types (e.g. endothelial cells) (61,62). Many studies highlighted TRPV1 as a pivotal protein for signal transduction in neurons (63-66), with a specific role in pain signaling (nociception) (67). TRPV1 integrates several stimuli, including: pH, heat, capsaicin or its analogs, and a variety of lipid metabolites such as anandamide, lipoxygenase products and dopamine derivative (68). TRPV1 function is also augmented by phosphorylation via protein kinase C downstream of PIP_2 hydrolysis and diacylglycerol formation (69). Notably, the molecular framework overseeing the modulation of TRPV1 function represents a hot topic in biology and biomedicine. In fact, sensitization of TRPV1 during chronic pain is associated to the transduction of

noxious signaling, and consequently the search for novel anti-pain therapeutics addressing TRPV1 is intense. A recent study pointed out that TRPV1 might be active only if localized in cholesterol-rich domains of the membrane, presumably rafts (70). The connection with rafts was supported by the inhibition of the opening properties of TRPV1 by sphingomyelin or gangliosides. Cholesterol depletion by incubation with methyl-β-cyclodextrin (MβCD) led to significant decrease of the capsaicin-evoked response (70,71). In addition, TRPV1 was found to contain a cholesterol-binding site in its membrane-embedded chain (72). Parallel researches highlighted the role of TRPV1 in microtubule remodeling, suggesting the presence of one microtubule-binding site along the receptor sequence (73,74). Yet, no comprehensive picture of the relationships between TRPV1 caveolins/rafts or tubulin is available. TRPV1 stands, therefore, as a perfect model of protein signal integrator to unveil its subtle modulation by membrane determinants.

1.2.1 Structure of TRP

Similarly to voltage-gated K^+ channels (Kv), TRPV1 structure comprises six transmembrane sections (1–6), with both the N- and C-termini on the cytosolic side of the cell membrane (75) and a short, pore-forming hydrophobic region between transmembrane section 5 and 6 (Fig. 1.6). Notably, the N- and C-termini of TRPV1 include “ankyrin” repeats (76) and the ‘oligomerization domain’ (77), respectively.

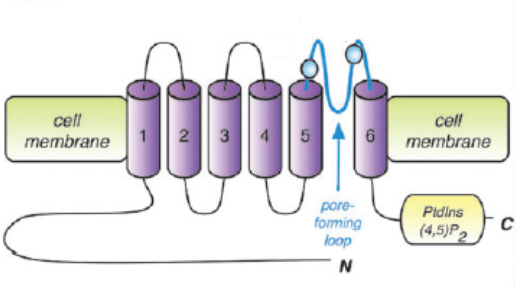

Figure 1.6. A cartoon representation of a single TRPV1 protein, highlighting the six transmembrane domains (Adapted from (78))

Single-particle electron cryo-microscopy suggested that TRPV1 assembles into a tetrameric complex in reconstructed unilamellar vesicles devoid of native lipid rafts (79). This finding is consistent with the biochemical studies in living cells that demonstrated a tetrameric stoichiometry for functional TRPV1 (80-82). The 3D structure of TRPV1 is 150 Å tall and consists of a smaller domain (~60 Å width and 40 Å height) embedded into the lipid bilayer, together with an intracellular larger domain that forms a basket-like structure (often referred to as "hanging gondola"). Within the TRPV1 tetramer, cryo-microscopy clearly identifies two major channel regions with respect to the membrane (Fig. 1.7).

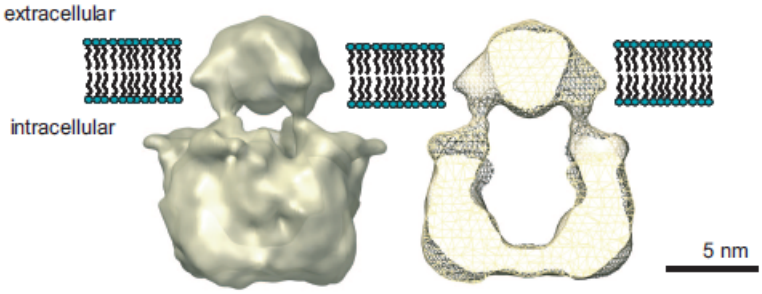

Figure 1.7. The proposed location of the 3D structure of TRPV1 in the plasma membrane. A vertical cut-away view shows the internal mass distribution of the protein. (Adapted from (79))

1.2.2 Function: agonists

TRPV1 integrates a number of physical and molecular stimuli. Beside voltage, modulators of TRPV1 activity include: temperature (83), pH (84) capsaicin and capsaicin analogues (Fig. 1.8) (85).

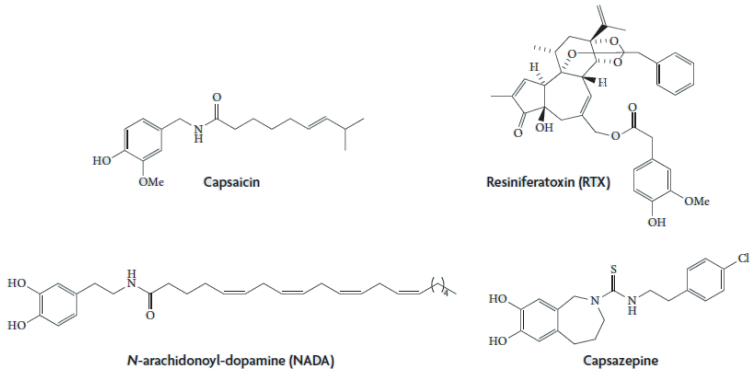

Figure 1.8. Chemical structures of selected TRPV1 ligands. Capsaicin, the pungent ingredient in hot-chilli peppers; resiniferatoxin, a powerful capsaicin analogue isolated from the cactus-like plant *Euphorbia resinifera Berg*; *N*-arachidonoyl-dopamine, an endogenous lipid mediator in brain nuclei; capsazepine the first generation of TRPV1 antagonist,. (Adapted from (86))

Resiniferatoxin (RTX, Fig. 1.8) is a strong TRPV1 agonist isolated from the latex of the perennial *Euphorbia resinifera Berg* (87). A recent model of TRPV1 structure and function proposes a "paddle structure" in which the transmembrane 3 and 4 regions form a gating paddle, and residues such as 547 constitute an intracellular vanilloid-binding site (88). Figure 1.9 shows a simulation of RTX and capsaicin bound to TRPV1 in the binding cleft (85). Significantly, activation of TRPV1 leads to an increase in the relative permeability to large cations and Ca^{2+} in dependence of time and agonist concentration. Using the substituted cysteine accessibility method, these changes were attributed to alterations in the TRPV1 selectivity filter. Thus, TRPV1 permeability characteristics are not static, at odds with most ion channels (89).

The dependence of TRPV1 from temperature is particularly interesting. TRPV1 is activated upon depolarization, and changes in temperature result in graded shifts of its voltage-dependent activation curve. Above 42 °C the receptor is mostly activated at resting membrane potential. This thermal sensitivity guarantees prompt cellular response to noxious heat (83). Kinetic analysis of gating at different temperatures indicates that temperature sensitivity in TRPV1 arises from a tenfold difference in the activation energies associated with voltage-dependent opening and closing (90). Chemical agonists of TRPV1 work as gating modifiers that potentiate the thermal

response. Two possible mechanisms for temperature-dependent channel gating may be envisaged on the basis of available data. The channel protein may undergo temperature-dependent structural rearrangements, thereby facilitating channel opening, or, alternatively, TRPV1 may be able to sense changes in membrane tension due to temperature-dependent lipid bilayer rearrangements. In absence of agonists, at 37 °C and at a membrane potential of -70 mV (typical of the resting state of CHO cells), only a minor fraction of TRPV1 (~ 15%) is in the open form (90), consistently with a thermal activation at around 42°C (91).

1.2.3 Function: antagonists and desensitization

TRPV1 antagonists fall into two categories: class A antagonists, which block the effects of both capsaicin and protons, and class B compounds, which are more selective for capsaicin, such as capsazepine 49 (Fig. 1.8). Notably, TRPV1 exhibits agonist-induced (acute and tachyphylactic) channel desensitization that should be distinguished from de-functionalization of the whole neuron by TRPV1 antagonists. This enables the neuron to adapt to specific stimuli by diminishing its overall response to a sustained chemical or physical signal (92).

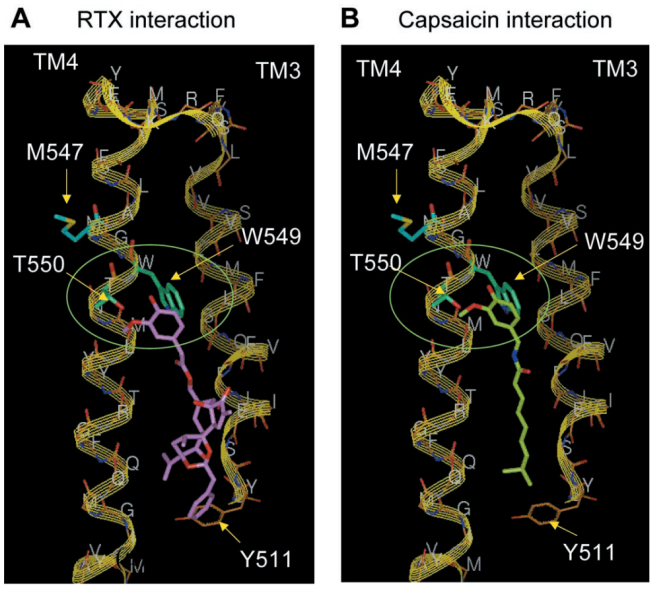

Figure 1.9. Structural model of RTX (*A*) and capsaicin (*B*) interacting with transmembrane helices TM3 and TM4 of TRPV1. The backbone of the complete structural model along with the side chains of residues considered to be involved in interactions is shown. The side chains of Met547, Trp549, and Thr550 are shown as *sticks* (*thick lines*). Specific interactions of vanillyl moiety with Thr550 and Trp549 are highlighted in the *green ellipses*. Residues considered being involved in interactions with the substituted phenyl portions of the two ligands are shown in *cyan*. Modeled hydrophobic contacts of Tyr511 with the hydrophobic ends of RTX and capsaicin are shown. RTX and capsaicin are displayed in *pink* (*A*) and *green* (*B*), respectively.

Several authors highlighted how agonist-induced TRPV1 desensitization is related to the increase of intracellular Ca^{2+}, which in turn activates calcineurin and leads to de-phosphorylation of TRPV1 (93). Thus, the role of TRPV1 phosphorylation and de-phosphorylation is pivotal to the biological function of the receptor. It is accepted that TRPV1 can be phosphorylated by several kinases, including PKA, PKC, Ca^{2+}/CaM-dependent kinase II (CaMKII) or Src kinase (94).

Reversal of capsaicin-induced desensitization of TRPV1 is regulated by PKC in both sensory neurons and heterologous expression systems (93). TRPV1 has two putative phosphorylation sites: S502 and S800. S502 is a non-specific substrate for TRPV1 phosphorylation by kinases like PKC, PKA or CAMKII, whereas S800 is a specific substrate of PKC. Importantly, S800 is located in the cytoplasmic C-

terminus of TRPV1 where several regulatory motifs of the receptor can also be found. PKC-dependent phosphorylation of Ser800 was demonstrated to potentiate agonist-evoked changes in channel permeability (94)

Chapter

2

Fluorescence imaging tools

2.1 Optical sectioning in fluorescence microscopy

2.1.1 Confocal laser scanning fluorescence microscopy

Conventional wide-field, epi-fluorescence microscopy offers sub-micrometer spatial resolution and excellent temporal resolution (down to a few ms) for the observation of biological structures and molecular dynamics in live cells. Epi-fluorescence microscopes, however, do not have any element other than the objective to discriminate between focal plane signal and background fluorescence originating from out-of-focal plane fluorophores. This results in a rather blurry image when 3D objects, for example cells, are observed (95). This issue was solved by the advent of confocal microscopy. In confocal fluorescence microscopy, single spot illumination is used while spatially scanning the sample; placing a "pinhole" before the detector at a conjugate plane to the illumination focal plane effectively rejects out-of-focal fluorescence. A simple schematic of an optical path in a fluorescence confocal microscope demostrating this concept is shown in Fig. 2.1. Notably, in most applications of confocal microscopy the sample is scanned across point-by-point by using a spatially-modulated laser beam (i.e. in a raster fashion):

these systems are referred to as Confocal Laser Scanning fluorescence Microscopes (CLSMs).

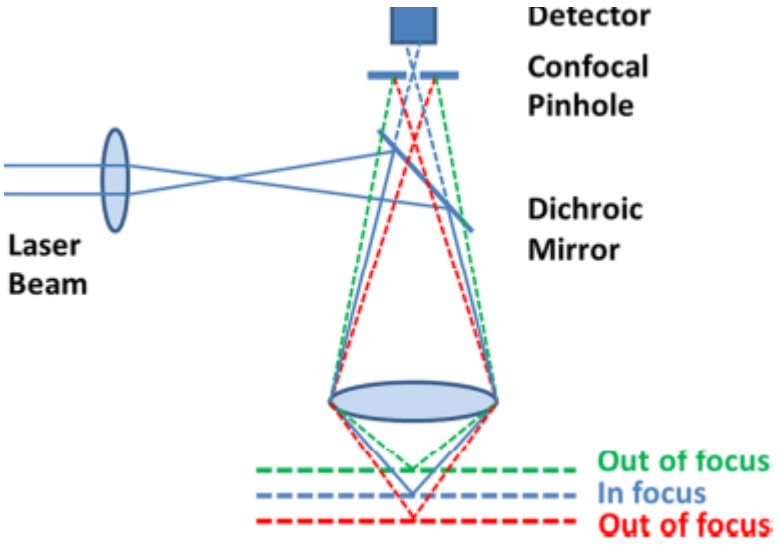

Figure 2.1. A schematic representation of the optical path in a point scanning confocal fluorescence microscope. The collimated excitation beam (solid blue) is directed to the microscope objective by a dichroic mirror and focused onto the sample. The fluorescence signal (dashed blue) emanating from the sample in focus is collected by the same objective and imaged through a pinhole onto a detector. The off-focal plane signal (dashed red and green) is rejected by the pinhole. Adapted from (95)

The sectioning capability of confocal microscopy yields an improved axial resolution over alternative strategies. Resolution here refers to the minimum distance between distinguishable objects in an image. Resolution is set by the spatial distribution of the light intensity generated and collected by the objective, which is called Point Spread Function (PSF). The image of any object is the convolution of the spatial feature of the object itself $S(x,y,z)$ with the PSF

$$I(x,y,z) = S(x,y,z) \otimes PSF(x,y,z). \qquad [2.1]$$

The PSF in confocal systems is usually well approximated by a 3D Gaussian distribution (96):

$$PSF(x,y,z) = I_0 \exp\left(-2\frac{x^2+y^2}{\sigma_{xy}^2}\right)\cdot\exp\left(-2\frac{z^2}{\sigma_z^2}\right), \quad [2.2]$$

where σ_{xy}^2 and σ_z^2 are known as the radial and axial resolutions of the optical setup, respectively, and I_0 is the maximum light intensity at focal point. It can be show that:

$$\sigma_{xy} = 0.43\cdot\frac{\lambda_{ex}}{NA}, \quad [2.3]$$

$$\sigma_z = 0.75\cdot\frac{\lambda_{ex}}{n-\sqrt{n^2-NA^2}}, \quad [2.4]$$

where n is the refraction index of the objective lens and λ_{ex} is the excitation wavelength. For a typical case such as λ_{ex} = 488 nm, NA=1.2, n=1.33 (water immersion objective), we have $\sigma_{xy} = 175\,\text{nm}$ and $\sigma_z = 483\,\text{nm}$. In some cases, the Full Width at Half Maximum (FWHM) of the PSF is the parameter of interest; these relationships hold for a Gaussian PSF:

$$FWHM_{xy} = \sigma_{xy}\cdot\sqrt{2\ln(2)}, \quad [2.5]$$

$$FWHM_z = \sigma_z\cdot\sqrt{2\ln(2)}. \quad [2.6]$$

2.1.2 Total internal reflection microscopy

Light propagating through a transparent medium will undergo total internal reflection (TIR) when it hits, at an angle greater than a critical value (θ_c), the interface with a second medium with a lower refraction index. Whenever TIR occurs, an evanescent field (EF) is generated at the interface and decays

exponentially into the second medium (97). This EF can be used to excite selectively fluorophores within a distance of a few hundred nanometers from the interface, rejecting concomitantly the out-of-focus fluorescence background. This is the underlying principle of Total Internal Reflection Fluorescence Microscopy (TIRFM). In modern TIRFM setups, the EF is obtained by passing the excitation light through an objective lens with a very high refractive index (1.4-1.5) as compared to water (the main component of the biological sample). To ensure total reflection at the objective-water interface, only a small annulus in the objective aperture plane is illuminated, yielding excitation beams that hit at the interface with angles $> \theta_c$ (Figure 2.2) (98). On account of its high axial sectioning capability (100-250 nm), TIRFM has excelled in the study of cellular organization and dynamic processes within or close to the cellular plasma membrane. Notably, in TIRFM the laser beam is not scanned across the sample but all the points are excited simultaneously, allowing for the use of highly-sensitive CCD detectors (e.g. Electron Multiplied CCD).

2.2 Genetically-encoded fluorescent probes for live cell imaging: autofluorescent proteins

The discovery of a fluorescent protein taking part in the bioluminescence system of jellyfish Aequorea Victoria dates back the early 60s (99). This protein was named Green Fluorescent Protein from its bright green fluorescence obtained by UV-blue light excitation; hereafter it will be simply referred to as wild-type GFP or wtGFP, in keeping with the scientific nomenclature in use. Thirty years later, with the cloning of the gene (100) and the demonstration that its expression in other organisms still produces fluorescence (101,102), the interest in wtGFP started to rise dramatically and eventually led to a revolution in fluorescence microscopy bioimaging (103). In the same years, many other fluorescent and non-fluorescent GFP homologues were discovered in a variety of organisms (104,105). Additionally, protein engineering by sequence mutagenesis has produced several Fluorescent Proteins (FPs) with optical properties spanning almost all regions of the visible spectrum (106).

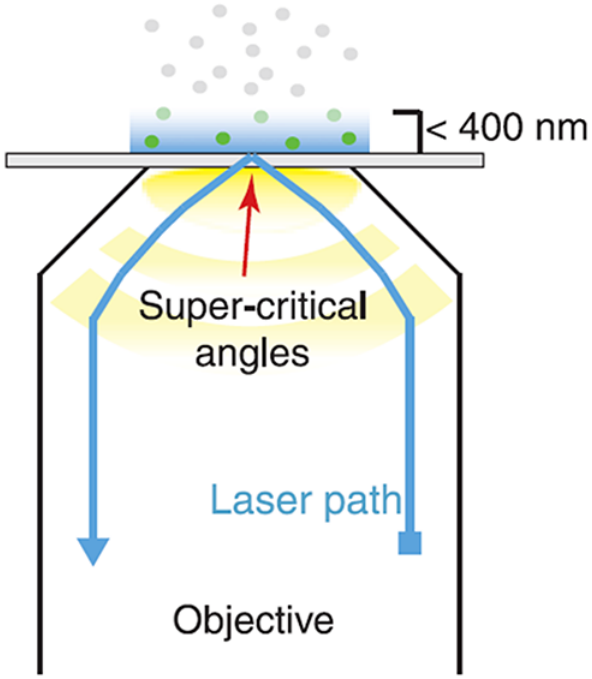

Figure 2.2. TIRFM configuration. Scheme of objective-based TIRFM. For description, see text. Adapted from (95)

The singular success of FPs in fluorescence microscopy owes to the genetic encoding of fluorescence that does not require any additional cofactor (eg. enzymes) from the host organism. This allows for the expression of any fluorescent chimera in living cells. FPs do not usually perturb the biological processes of the target protein. Hence, FPs represent a nearly perfect bio-nanodevice to unveil cell mechanisms at the molecular level (107-109).

wtGFP is constituted by a peptide chain of 238 aminoacids and 27 kDa molecular weight (103). X-ray spectroscopy displayed that this sequence folds in a compact cylindrical three-dimensional structure (referred to as β-barrel, Fig. 2.3), laterally-enclosed by 11-stranded β-sheet, and with a base diameter of 24 Å and a height of 42 Å (110). Remarkably, all FPs share thus β-barrel fold, regardless of the degree of

homology of their primary sequences (107). Differences can be found in quaternary structure, since several natural FPs arrange as tightly bound tetramers or dimers, a feature that initially hampered their applications. Primary sequence mutagenesis was applied to reverse association and yield monomeric variants of the parent proteins (111).

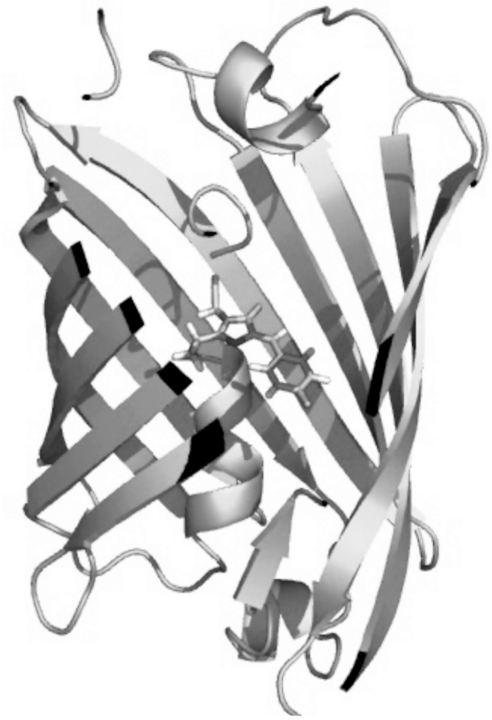

Figure 2.3. 3D structure of wtGFP from X-ray analysis The frontal part of the barrel is removed to show the protein chromophore buried at the center of the tertiary structure. Adapted from (110).

In wtGFP, the chromophore (Chrom) is a 4-(*p*-hydroxybenzylidene) imidazolinone. Structurally, Chrom is constituted by two conjugated aromatic rings, one being a six-member aromatic phenol and the other being a five-member imidazolidinone (Fig. 2.4) (103). The alternating single and double bonds in the bridge region of Chrom extend the electron delocalization from the phenolate to the

carbonyl of the imidazolinone. Accordingly, efficient visible-light absorption takes place due to this π-conjugated system. Chrom originates from the post-translational autocatalytic modification of three consecutive aminoacids: Ser^{65}-Tyr^{66}-Gly^{67} (112,113) (Fig. 2.4). Several FPs share the Chrom structure of wtGFP. Instead, Red Fluorescent Proteins (RFPs) are characterized by further post-translational processing of the chromophore that leads to more extended electron conjugation.

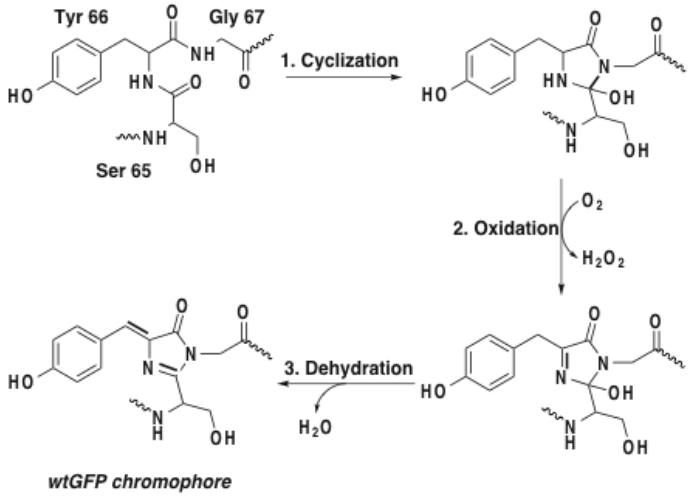

Figure 2.4. Formation of wtGFP chromophore. The cyclization-oxidation-dehydratation post-translational processing of the aminoacid triplet Ser^{65}-Tyr^{66}-Gly^{67}. Adapted from (114)

For all FPs sharing the wtGFP Chrom, the phenol group can exist either as neutral (protonated phenol) or anionic (deprotonated phenol). The absorption of the neutral form (**A** state) is always significantly blue-shifted with respect to the anionic form **(B** state): indeed, in wtGFP **A** peaks at 398 nm, whereas **B** peaks at 475 nm (Fig. 2.5). The **A**/**B** population ratio is around 6/1, and it is nearly unaffected by changes of proton concentration in the 5-11 pH range (115). This rather unexpected phenomenon was explained by means of the presence of a second ionizable residue near the chromophore, namely Glu222, which buffers the chromophore ionization (116).

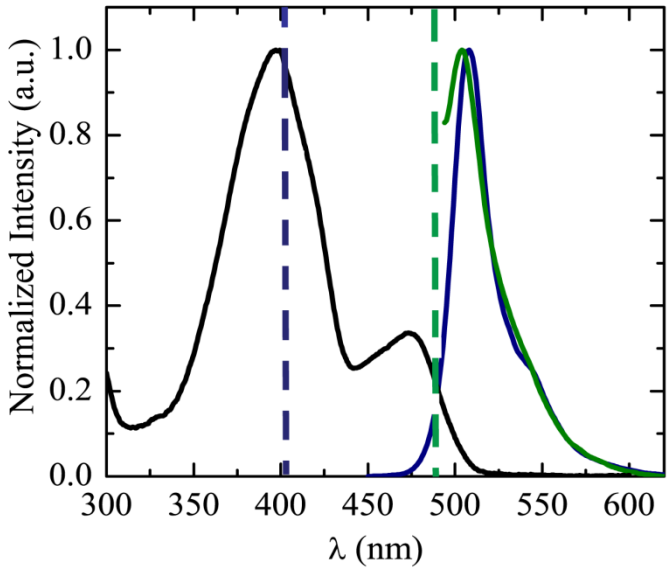

Figure 2.5. Optical properties of wtGFP. Normalized absorption (black line) and emission of state A (blue line) excited at 405 nm (dashed blue line) and emission of state B (green line) excited at 488 nm (dashed green line).

Fluorescence emission of wtGFP was extensively studied at very high temporal resolution (117,118). The rigid β-barrel structure is responsible for the significant protein fluorescence emission. In wtGFP $\Phi_A \approx \Phi_B = 0.78$ (119,120). Photon absorption by **B** leads to excited state **B*** that has a single emission channel at 503 nm. Conversely, upon excitation of **A** two competing photoprocesses leading to emission are triggered: i) direct emission from **A*** (at 440-480 nm) and ii) Excited State Proton Transfer (ESPT) from **A*** to Glu^{222} through a proton wire of H-bonds involving one water molecules and Ser^{205} (117,118,121) eventually leading to 507 nm emission. ESPT takes place in a few picoseconds on account of the strongly increased acidity of the phenol group (122), and it represents a much more efficient depletion channel of **A*** than direct fluorescence emission (123). Many other GFP variants share these photophysical properties.

Five main families of FPs can be identified: blue (BFPs), cyan (CFPs), green (GFPs), yellow (YFPs), and red emitting (RFPs). In the following, I shall briefly describe the properties of GFPs, YFPs, and RFPs because FPs belong to these families were employed in this work.

GFPs. The proteins belonging to this class have optical properties similar to those displayed by wtGFP, although in most cases only the bright anionic form of the chromophore is optically active. Indeed, the most popular green variant, Enhanced Green Fluorescent Protein (F64L/S65T GFP or EGFP) owes its high brightness to a predominantly anionic tyrosin-based Chrom (Y-Chrom) above pH 6 (116,124). In several GFPs (e.g. EGFP), the change of the external pH enables the reversible population shift from the neutral to the anionic states of the chromophore; this phenomenon is associated with a pH-titration curve clearly observable both in absorption and in fluorescence(125).

YFPs. YFPs share an aromatic moiety (from Tyr, Phe, or His) π-stacked to GFP Chrom. In this configuration, the excitation and emission energies of Chrom are reduced by increasing the polarizability of the environment around the chromophore (126). Best results were obtained with T203Y GFPs. Variants EYFP (S65G/V68L/T203Y GFP) and 10C (S72A EYFP) display possibly the highest extinction coefficients (> 75,000 $M^{-1}cm^{-1}$), emission quantum yields ($\Phi > 0.8$), and fluorescence lifetimes ($\tau > 3$ ns) that can be found in FPs. In most cases, YFPs show pH-dependent absorption and fluorescence response, owing to chromophore ionization. Additionally, the fluorescence of many YFPs is quenched by chloride ion, on account of a binding equilibrium with dissociation constant > 10 μM at physiological pH (127-131).

RFPs. As already stated, the strong red-shift of RFPs compared to wtGFP is mainly attributable to the enlargement of the π-conjugated system by the additional double bond. Representative RFPs display absorption shifts from +71 to +133 nm, and emission shifts from +54 to +142 nm, compared to the **B** state (anionic) of wtGFP (Table 1). Additionally, the anionic chromophore is the prevalent form in the 5-9 pH range. Interestingly, many RFPs display deviation from coplanarity of the two aromatic rings in the protein chromophore, resulting in a reduced quantum yield of fluorescence. As an example, the widely-used mCherry variant is characterized by a particularly distorted chromophore and a rather low fluorescence quantum yield (0.22) (109). For high-sensitivity imaging, a much better choice is represented by TagRFP, a monomeric red (orange) fluorescent protein generated from the wild-type RFP from sea anemone *Entacmaea*

quadricolor (132). It possesses bright fluorescence (Φ=0.66 (133)) with excitation/emission maxima at 555 and 584 nm, respectively.

.

Chapter

3

Binding interactions of TRPV1 in living cells

Recent literature data highlighted that, besides acting as a ligand-gated voltage-dependent ion channel, the TRPV1 receptor could participate to a complex network of binding interactions at cell membrane level. For instance, colocalization measurements in fixed cells suggested that microtubules could represent binding partners of TRPV1. The relevance of this interaction stems from the observed disassembly of microtubules, and possible cytoskeletal remodeling, upon receptor activation. Additionally, the clathrin-independent endocytotic mechanism that underlines the TRPV1 long-term desensitization evokes the binding interaction of the receptor with biomolecules involved in vesicular trafficking.

In this chapter we demonstrate for the first time in living cells that the TRPV1 receptor effectively binds to both microtubules and caveolin-1, the latter being the molecular hallmark of caveolar internalization mechanism. Notably, our results are based on Fluorescence (Förster) Resonance Energy Transfer (FRET) measurements. Indeed, FRET is among the most efficient techniques to reveal biomolecular complexes in living cells. For this reason, section 3.1 is devoted to a comprehensive description of FRET imaging. Sections 3.2 and 3.3 report on the interaction between TRPV1 and integer microtubules and caveolin-1, respectively. The experimental procedures are described in section 3.4.

3.1 Imaging biomolecular interactions: Fluorescence (Förster) Resonance Energy Transfer (FRET)

3.1.1 General description

Fluorescence (Förster) Resonance Energy Transfer (FRET) is a spectroscopic technique easily implementable in fluorescence microscopy that is ideally suited to study biomolecular interactions in solution, live cells, and tissues (134). FRET is based on the non-radiative transfer of energy from an excited molecular fluorophore (donor, D) to a chromophore (acceptor, A) via long-range dipole-dipole coupling (135). A necessary condition for FRET is the partial overlap of the emission spectrum of D with the absorption spectrum of A, to ensure conservation of energy in the non-radiative exchange process (Fig. 3.1).

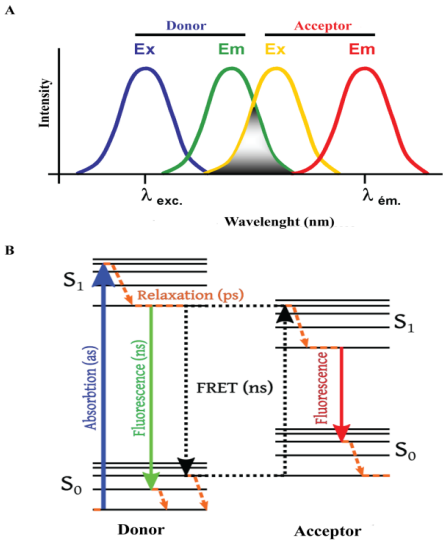

Figure 3.1. FRET mechanism. (A) Illustration of the overlap between the emission spectrum of the donor and the absorption of the acceptor. (B). Energy level scheme of donor and acceptor molecules showing the coupled transitions in the case where vibrational relaxation is faster than energy transfer (very weak coupling).

In most applications the acceptor is fluorescent, although this is not required for FRET to take place. According to Förster's theory (135,136), the rate of energy transfer is expressed by:

$$k_{FRET} = \frac{1}{\tau_{FRET}} = \frac{1}{\tau_D^0}\left[\frac{R_0}{r}\right]^6, \qquad [3.1]$$

where τ_D^0 is the emission lifetime of D in absence of acceptor, τ_{FRET} is the time required for the energy transfer to take place, r is the separation between D and A, and R_0 (Förster radius) is the distance at which transfer and spontaneous decay of the excited D are equally probable ($\tau_D^0 = \tau_{FRET}$). R_0 can be determined from spectroscopic data, following:

$$R_0 = 2.108\times10^{-2}\left[n^{-4}\cdot\kappa^2\cdot\Phi_D\cdot J(\lambda)\right]^{1/6} \text{ nm}, \qquad [3.2]$$

where κ^2 represents the angle between the two transition dipoles of D and A, Φ_D is the donor quantum yield, and $J(\lambda)$ is the so-called spectral overlap integral between D and A (135):

$$J(\lambda) = \frac{\int F_D(\lambda)\cdot\varepsilon_A(\lambda)\cdot\lambda^4 d\lambda}{\int F_D(\lambda)\cdot d\lambda}. \qquad [3.3]$$

In Eq. 3.3 $F_D(\lambda)$ is the area-normalized emission spectrum of the donor and $\varepsilon_A(\lambda)$ is the molar absorption spectrum of the acceptor. κ^2 modulates deeply FRET emission. Its values can range between 0 and 4. A value of 0 corresponds to a perpendicular orientation of donor and acceptor transition dipole moments, yielding no FRET. A value of 4 corresponds to a collinear orientation between the two dipoles, leading to maximal FRET. If the fluorophores possess complete rotational freedom, the statistical average over all sampled orientations leads to κ^2=2/3 (137). This value is typically used for the calculation of R_0 of FRET pairs. Yet, great care must be taken whenever steric restrictions could invalidate the above assumption.

Good D/A couples are characterized by a large overlap integral associated with R_0 in the 3-10 nm range. Accordingly, FRET requires nm-scale proximity between

molecules for a time comparable to the emission lifetime of donor, i.e. in the ns range (see Eq. 3.1). This combination is possible only when D and A are engaged in a complex or they are confined close to each other by the surrounding matrix. In fact, pure statistical collisions would take place in ps time scale or shorter, not allowing FRET to take place. Conventionally, FRET is measured through its "efficiency" (*E*), i.e.:

$$E = \frac{k_{FRET}}{k_{FRET} + \left(1/\tau_D^0\right)} = \frac{R_0^6}{R_0^6 + r^6}. \qquad [3.4]$$

Quantitative determination of *E*, combined with knowledge of R_0 for the D/A couple would provide structural information on the distance between the binding partners (eq. 3.4). It is worth noting the steep dependence (inverse of sixth power) of *E* from the distance *r* (Fig. 3.2) that makes *E* exquisitely sensitive to the separation among the partners. Accordingly, FRET provides a tools for resolving molecular interactions up to 10-12 nm far exceeding the optical diffraction limit (138).

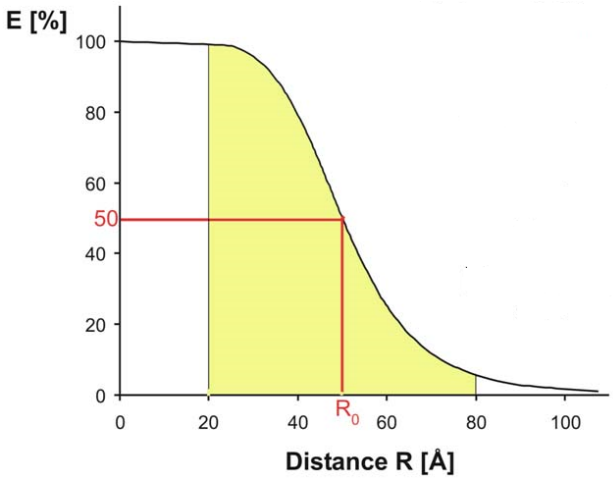

Figure 3.2. Distance-dependency of FRET-efficiency.

3.1.2 FRET via sensitized emission

In the last twenty years FRET has been widely applied to probe interactions among biomolecules (139). Several methods were proposed to combine FRET with fluorescence imaging, in view of obtaining maps of FRET efficiency at submicron scale (140).

In principle, *E* could be obtained in each pixel from the ratio of D fluorescence in presence or in absence of the acceptor (ratio-imaging FRET):

$$E = \left(1 - \frac{F_{DA}}{F_D}\right) \qquad [3.5]$$

The main drawback of ratio-imaging FRET is its inability to correct for D cross-talk (i.e. D emission at A emission wavelength) and acceptor bleed-through (non-FRET residual A excitation at D excitation wavelength). Cross-talk and bleed-through are particularly severe for D/A couples with extensive spectral overlap. In order to remove these two spurious contributions, two correction coefficients α and β are introduced:

$$\alpha = \frac{F\left(\lambda_D^{ex}, \lambda_A^{em}\right)}{F\left(\lambda_A^{ex}, \lambda_A^{em}\right)} \quad \beta = \frac{F\left(\lambda_D^{ex}, \lambda_A^{em}\right)}{F\left(\lambda_D^{ex}, \lambda_D^{em}\right)}, \qquad [3.6]$$

where λ_D^{ex} = D excitation wavelength, λ_D^{em} = D emission wavelength interval, λ_A^{ex} =A excitation wavelength, λ_A^{em} = D excitation wavelength interval. α and β can be calculated by inspecting samples containing only the acceptor and the donor, respectively.

In samples containing both A and D, FRET emission is measured in the $\left(\lambda_D^{ex}, \lambda_A^{em}\right)$ setting and then corrected according to:

$$F_{corr}\left(\lambda_D^{ex}, \lambda_A^{em}\right) = F\left(\lambda_D^{ex}, \lambda_A^{em}\right) - \alpha F\left(\lambda_A^{ex}, \lambda_A^{em}\right) - \beta F\left(\lambda_D^{ex}, \lambda_D^{em}\right) \qquad [3.7]$$

Then, an apparent FRET efficiency *E* is calculated upon normalizing $F_{corr}\left(\lambda_D^{ex}, \lambda_A^{em}\right)$ by either D or A emission. For donor normalization we have:

$$E_{app} = \frac{F_{corr}\left(\lambda_D^{ex}, \lambda_A^{em}\right)}{F\left(\lambda_D^{ex}, \lambda_D^{em}\right)}. \quad [3.8]$$

It can be easily demonstrated that $E_{app} = E$ for $I(\lambda_A^{ex}) = I(\lambda_D^{ex})$ and/or α=0, where *I* stands for excitation intensity. Even if these conditions do not apply, E_{app} is a robust estimate of *E* whenever donor and acceptor excitation intensities are of the same order of magnitude.

3.1.3 Optimized fluorescent proteins as FRET couples

Fluorophores for FRET must fulfill a number of criteria. First the spectral overlap between donor fluorescence and acceptor excitation wavelengths should be as large as possible. Additionally, the donor and the acceptor should be associated with large quantum yields and extinction coefficients. In recent years, a considerable effort was devoted to developing fluorescent protein couples for FRET. In particular, the engineering of new bright and photostable RFPs allowed the use of popular GFP and YFP variants as donors in GFP/RFP or YFP/RFP FRET couples.

Among RFP acceptors, an excellent choice is represented by TagRFP, a monomeric red fluorescent protein derived from the wild-type RFP extracted from sea anemone *Entacmaea quadricolor* (132). It possesses bright fluorescence (Φ=0.66 (141)) with excitation/emission maxima at 555 and 584 nm, respectively (Fig. 3.3). TagRFP displays good R_0 values in tandem with popular EGFP and YFP variants (Fig. 3.3). For these reasons TagRFP was selected as common acceptor partner in all FRET measurements carried out in this thesis.

As for donors, an interesting member of GFP family is E^0GFP. E^0GFP differs from wtGFP for the F64L mutation, which increase the folding efficiency such as in EGFP (142), and the silent mutation H231L. Very much alike to wtGFP, E^0GFP displays: 1) a major absorption peak at 400 nm and a minor peak at 476 nm corresponding to the protonated and the anionic forms of the chromophore (Fig. 3.3), respectively; 2) efficient ESPT upon 400 nm excitation, yielding green light peaked at 508 nm with Φ=0.6 (143). This pronounced Stokes shift (108 nm, 5315 cm^{-1}) can be exploited for FRET measurements with TagRFP acceptor. Indeed, this couple is associated with a large separation between donor and acceptor excitation frequencies and a negligible acceptor bleed-through (Fig. 3). Minimizing bleed-through in FRET couples is necessary to avoid cumbersome data manipulation in

sensitized emission measurements. E^0GFP displays a large Forster radius when coupled with TagRFP (5.4 nm) and $\alpha < 1\%$.

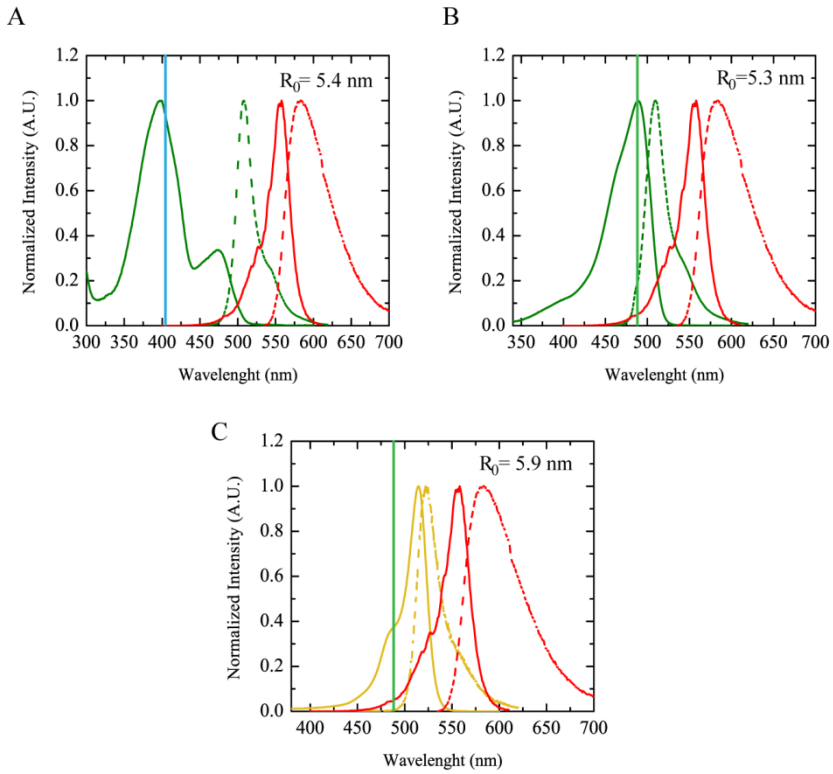

Figure 3.3. Spectroscopic properties of typical FRET pairs. (A) Normalized absorption (solid lines) and emission (dashed lines) of E^0GFP (green) and TagRFP (red). (B) Normalized absorption (solid lines) and emission (dashed lines) of EGFP (green) and TagRFP (red). (C) Normalized absorption (solid lines) and emission (dashed lines) of YFP (yellow) and TagRFP (red). The straight line in each graphic indicates the typical wavelength of excitation for FRET measurement.

3.2 Detection of TRPV1 interactions with microtubules

Recently, a few groups demonstrated the interaction of TRP channels with microtubule cytoskeleton (144-146). Using tests on fixed cells, as well as

biochemical essays, the interaction of TRPV1 with tubulin dimer was proposed and attributed to two short sequences in the cytoplasmic tail of the receptor (73,147,148). To shed light on the putative interaction between microtubule and TRPV1, we carried out sensitized emission FRET measurements in living cell. Our results are described and discussed in the following sections.

3.2.1 Localization and functionality of transiently transfected TRPV1-FP chimeras

For the imaging studies reported in this section and, more generally, in the whole thesis work, we prepared a toolbox of TRPV1 chimeras with different FPs, namely: E^0GFP and EGFP (green), YFP (yellow), and TagRFP (red). The first three constructs were prepared from a common plasmid by several runs of single-point mutagenesis; TRPV1-TagRFP was obtained by cloning the TRPV1 sequence into a commercial plasmid expressing TagRFP. In all the experiments, TRPV1 was transiently expressed and imaged in Chinese Hamster Ovary cells (CHO) because this line does not express endogenously the TRPV1 channel.

TRPV1 at basal state showed non-homogeneous localization in the plasma membrane (Fig. 3.4) and in the ER. Previous reports on fixed cells indicated similar localization patterns (149). Likely, the heterogeneous distribution of TRPV1 is relevant for its biological function. The nature of FP reporter did not affect the TRPV1 distribution (Fig. 3.4).

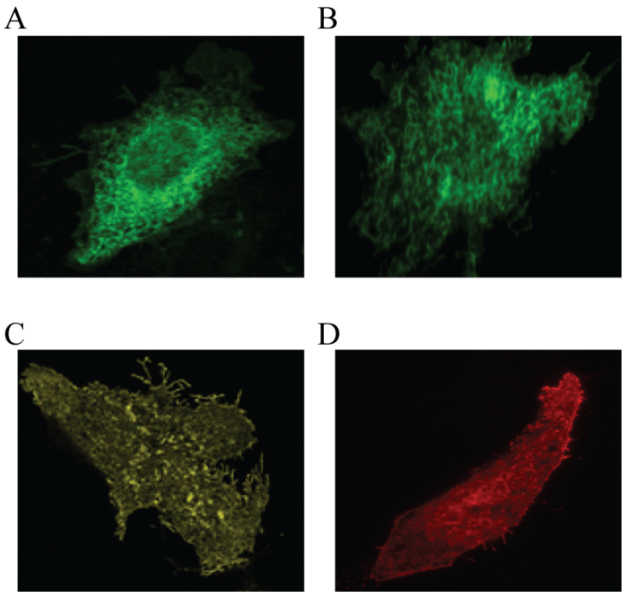

Figure 3.4. TRPV1 localization. CHO K1 transfected with TRPV1-E^{0}GFP (A), TRPV1-EGFP (B), TRPV1-YFP (C) and TRPV1-TagRFP (D) imaged by using confocal microscopy (A and C) or TIRFM (B and D)

Next, we tested the ion channel functionality of the TRPV1-FP constructs. In particular, we assessed the ability of the labeled receptor to activate inward calcium flux upon RTX stimulation at 20 nM.. This concentration was selected because it ensured full saturation of membrane receptors while preserving cell viability (EC50 of RTX is 0.15 nM (150)). The variations of intracellular calcium were monitored by the fluorescent indicator *Calcium Crimson*. Similarly to what observed for physiological TRPV1 (150), RTX induced a gradual increase of intracellular Ca^{2+} that leveled off about 100 s after administration (Fig. 3.5).

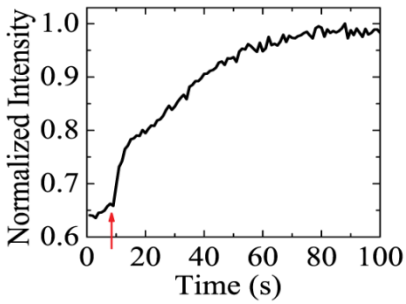

Figure 3.5 TRPV1 functionality. Calcium signals registration in cell upon activation by RTX at 20 nM concentration.. The arrow indicated the time when RTX is added.

Accordingly, in this thesis work all the subsequent biophysical measurements that entailed receptor activation were carried out after an induction time of 100 s.

3.2.2 Effect of microtubules disassembly on TRPV1 activation

To verify the effect of microtubule integrity on TRPV1 activation, we tested the receptor functionality upon treatment with 10 μM nocodazole. This concentration affords the total disassembly of microtubules after 1-5 minutes from administration, as clearly showed by the radical change of the fluorescence pattern given by TagRFP-α-Tubulin (Fig. 3.6).

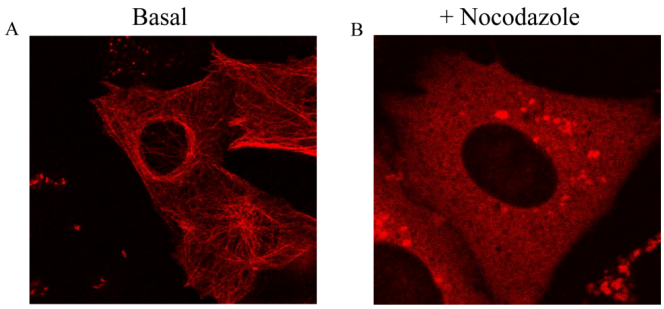

Figure 3.6 Effect of nocodazole administration on microtubules. (A) Microtubules show typical filament structure at basal state. (B) Microtubule disassembly results in a rather homogeneous distribution of fluorescence.

The concomitant effects of nocodazole and RTX agonist were assessed by measuring the change in intracellular calcium concentration by following an imaging procedure analogous to that reported in §3.2.1 (Fig. 3.7).

Notably, disassembly of microtubules decreased the maximum amplitude of Ca^{2+} concentration by about 40% and they slowed significantly the influx kinetics. Therefore, microtubule integrity is relevant for TRPV1 functionality. This conclusion is specular to the recognized role of TRPV1 activation in promoting microtubule remodeling through disassembly (25). This effect suggests that a complex molecular interplay holds for TRPV1 and microtubules.

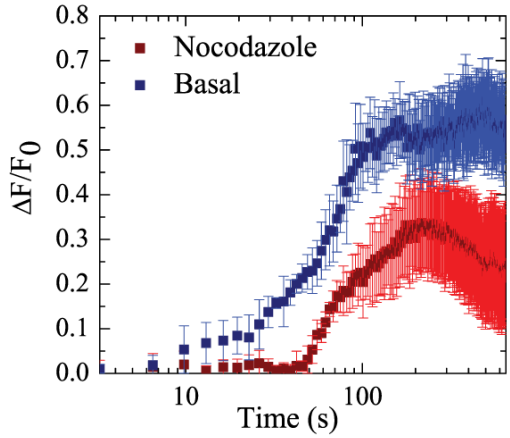

Figure 3.7 Calcium signals registration after RTX administration in cells expressing TRPV1-YFP. Plot of fluorescence variation of *calcium crimson* following RTX administration to cells, treated with (red curve) and without (blue curve) nocodazole. Each curve represents the average of ten acquisitions and for each point the standard deviation is reported.

3.2.3 FRET imaging of TRPV1-microtubule binding

Literature data on the binding interaction between TRPV1 and microtubules are based on *in vitro* biochemical assays (73) and colocalization analysis on fixed cells (151). In this thesis the binding interaction between TRPV1 and microtubules was explicitly imaged by FRET in the membrane of living cells. FRET measurements were carried out in CHO cells co-expressing TagRFP-α-Tubulin (TagRFP-αT) as

acceptor and TRPV1-E^{0}GFP or TRPV1-EGFP or TRPV1-YFP as donor. Inspection of Fig. 3.3 highlights that all FRET couples are associated with negligible levels of cross-talk/bleed-through when FRET emission is collected above 600 nm and donor excitation below 490 nm takes place. All couples are characterized by large Forster radii (Fig. 3.3), as calculated under the assumption of free mutual rotation of transition dipoles ($\kappa^2 = 2/3$, § 3.1.1). Large R_0 values allow for FRET detection over large inter-protein distances such as those expected when one or both partners are multimeric receptor proteins. Accordingly, the sensitized emission mode of measuring FRET (§ 3.1.2) was adopted.

At first, confocal imaging experiments were carried by using TRPV1-E^{0}GFP or TRPV1-YFP as donors, and TagRFP as acceptor. Remarkably, significant FRET emission was revealed in the membrane of cells in basal state. Both couples yielded similar donor-normalized E_{app}: 0.25±0.03 for TRPV1-E^{0}GFP/TagRFP-αT (10 cells) and 0.27±0.03 for TRPV1-YFP/TagRFP-αT (20 cells). From Eq. 3.4, these figures indicate a 6.5-7.0 nm distance between FP chromophores. Taking into account the size of the FP β-barrel (2-2.5 nm), one can calculate a 5-6 nm distance between TRPV1 and α-tubulin.

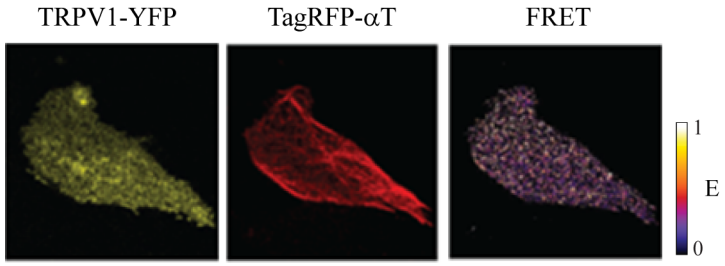

Figure 3.8 FRET measurements on cells expressing TRPV1-YFP and TagRFP-αT. Left panels: donor emission images (λ_{exc}= 488 nm λ_{em}= 500-530 nm); middle panels: acceptor emission images (λ_{exc}= 561 nm λ_{em}= 600-640 nm): right panels: maps of donor-normalized, apparent FRET efficiency (λ_{exc}= 488 nm λ_{em}= 600-640 nm).

We should stress that these results are compatible with TRPV1 binding to either component of α,β-tubulin dimers, since each dimer has an average size of 4.6x8.0x6.5 nm. Nonetheless, previous biochemical assays suggest that TRPV1 more preferably interacts with β-tubulin.

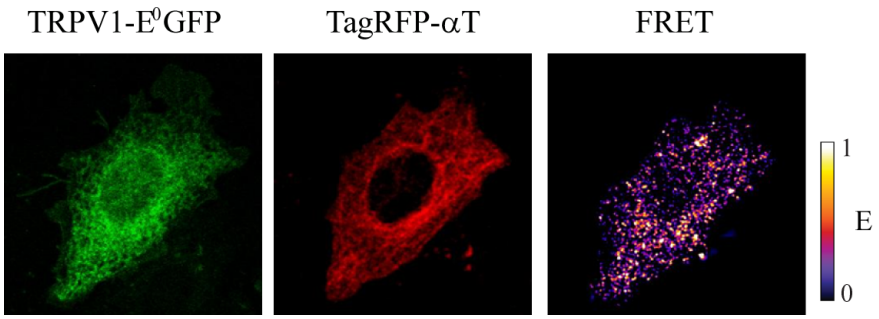

Figure 3.9. FRET measurements on cell expressing TRPV1-E^{0}GFP and TagRFP-αT. Left panel: donor (TRPV1-E^{0}GFP) emission image (λ_{exc}= 405 nm, λ_{em}= 500-530 nm); *middle panel:* acceptor (TagRFP-αT) emission image (λ_{exc}= 561 nm λ_{em}= 600-640 nm); right panel: FRET map of donor-normalized apparent FRET efficiency (λ_{exc}= 405 nm λ_{em}= 600-640 nm).

The membrane localization of binding interaction was confirmed by sensitized emission FRET experiments carried out in TIRF mode (Fig. 3.9). Interestingly, TIRF-FRET images highlighted the existence of 500-1000 nm-domains where the binding interaction was prevalent.

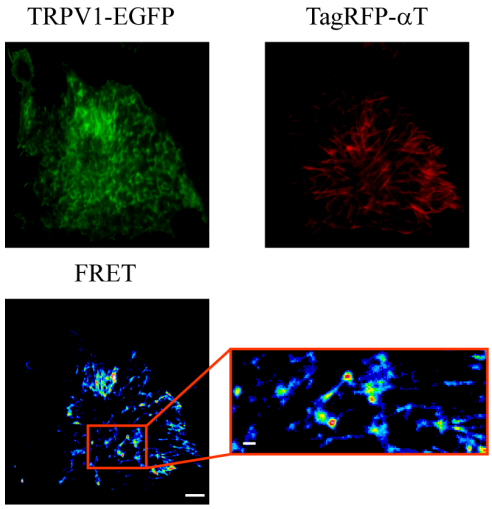

Figure 3.10. FRET imaging of TRPV1-microtubules interaction. Upper left panel: donor emission image; upper right panel, acceptor emission image; lower left panel, donor-normalized apparent FRET image; scale bar: 5 μm. Lower right: zoom of a region of the FRET image; scale bar: 1 μm.

Sensitized emission FRET images pointed out that receptor stimulation had no effect on the complex (E_{app}=0.26±0.06, YFP/TagRFP couple, 10 cells). Vice-versa, nocodazole treatment led to complete disappearance of FRET. This finding supports the notion of direct interaction with microtubules, i.e. binding between TRPV1 and a tubulin dimer belonging to integer microtubule protofilaments.

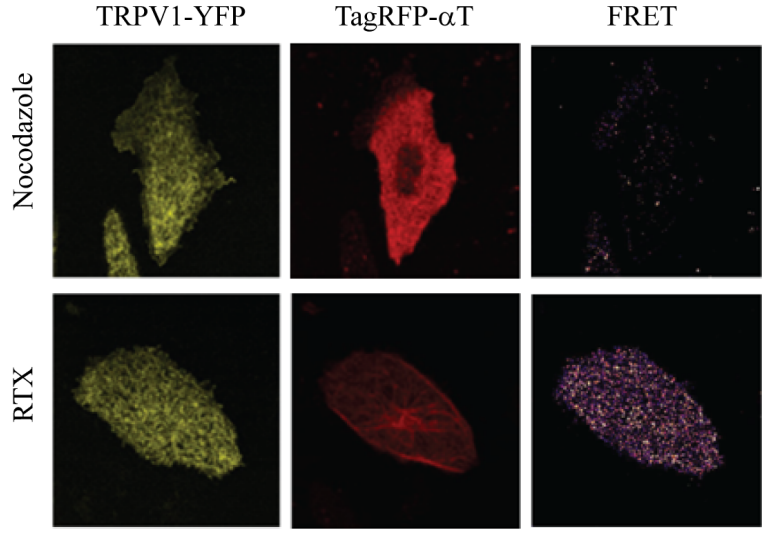

Figure 3.11. FRET measurements on cells expressing TRPV1-YFP and TagRFP-αT upon RTX or nocodazole administration. Left panels: donor emission images (λ_{exc}= 488 nm λ_{em}= 500-530 nm); middle panels: acceptor emission images (λ_{exc}= 561 nm λ_{em}= 600-640 nm): right panels: maps of donor-normalized apparent FRET efficiency (λ_{exc}= 488 nm λ_{em}= 600-640 nm.

3.3 TRPV1 interaction with caveolin-1

Sanz-Salvador et al. (152) reported that agonist exposure of DRG neurons and TRPV1-expressing cells promotes receptor endocytosis and down-regulation through lysosomal degradation. This process requires Ca^{2+} entry and appears mediated by an endocytotic mechanism that is clathrin-independent. Caveolar endocytosis represents a major internalization pathway of membrane proteins and it

is clathrin-independent (153). As already stated at §1.14, caveolin-1, the main structural protein in caveolae, plays a crucial role in the membrane localization of several members of TRP family (24,154,155). Furthermore, caveolae-enriched regions of the membrane usually coincide with raft domains (156). Lipid rafts are in turn the preferential membrane locations of TRPV1 (70). Thus, we hypothesized that TRPV1 activity could be connected to caveolin-enriched membrane regions and their endocytotic pathway. In this framework, caveolar endocytosis could be responsible for TRPV1 down-regulation after activation. Accordingly, we set out to determine if caveolin-1 and TRPV1 mutually interact.

3.3.1 FRET imaging of TRPV1-caveolin-1 binding

The existence of molecular interaction between TRPV1 and caveolin-1 was investigated by colocalization and sensitized emission FRET. Measurements were carried out in CHO cells transiently expressing TRPV1-TagRFP and caveolin-1-EGFP. At first, we tested the colocalization of the two proteins at basal state and after agonist stimulation. At basal state, caveolin-1-EGFP and TRPV1-TagRFP showed limited colocalization in the internal regions of CHO cells (Fig. 3.12), as witnessed by the value of Pearson coefficient $\langle r \rangle = 0.47 \pm 0.05$ (average of #5 cells). We should remind that positive colocalization holds for $r \geq 0.5$ (157).

Yet, a few minutes after agonist administration, caveolin-1-EGFP was found to colocalize, although not completely, with TRPV1-TagRFP ($\langle r \rangle = 0.70 \pm 0.09$, #10 cells) in intracellular regions that should be identified as caveolar vesicles and caveosoma (Fig. 3.12). This finding suggests a role for caveolin in the control (through internalization) of membrane TRPV1 concentration following agonist stimulation. The statistical difference between basal and activated states was confirmed also by *t*-test between the two relevant datasets, for which we calculated $p < 10^{-4}$.

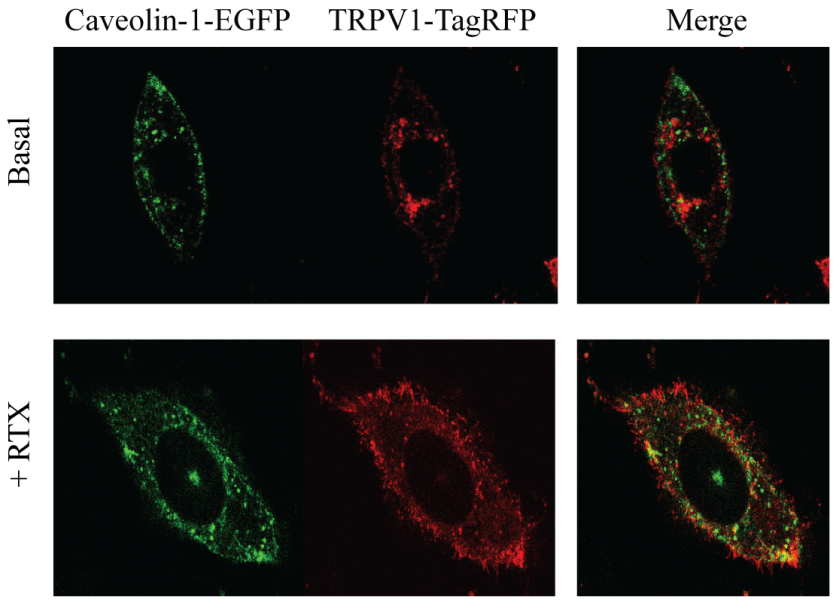

Figure 3.12. Colocalization experiments between caveolin-1-EGFP and TRPV1-TagRFP inside the cells. Colocalization between caveolin-1-EGFP and TRPV1-TagRFP in CHO cell before (upper panels) and after RTX administration (lower panels).

To determine whether caveolin-1 and TRPV1 bind at membrane level in basal condition, we performed sensitized emission FRET experiments (§ 3.1.2) on the caveolin-1-EGFP/TRPV1-TagRFP couple in TIRF configuration. Excitation was set at 488 nm and FRET emission was collected above 600 nm. In this spectral configuration negligible spectral cross-talk and bleed-through (<4%) affect the FRET measurements (§ 2.2.2). Consequently, photons collected in the acceptor channel upon donor excitation were attributed to FRET alone. Remarkably, we obtained a positive sensitized-emission FRET signal, which witnesses protein-protein binding.

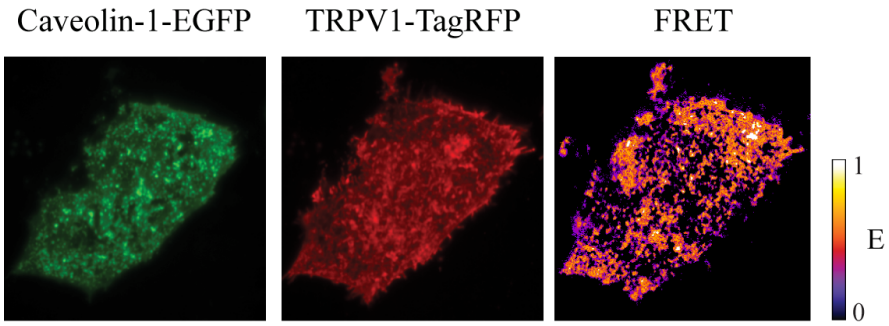

Figure 3.13. FRET imaging of TRPV1-microtubules interaction. Left panel, donor emission image; middle panel, acceptor emission image; right panel, donor-normalized apparent FRET efficiency.

Quantitatively, we recorded E = 0.38±0.05 (10 cells). From Eq. 3.4, this value afforded a 5.7 nm distance between FP chromophores, which in turn suggests a 3-3.5 nm distance between TRPV1 and caveolin-1 by removing the contribution of the FP β-barrel (§3.2.2). TIRF-FRET images highlighted the existence of 200-300 nm "confined" regions where the binding interaction takes place (Fig. 3.14).

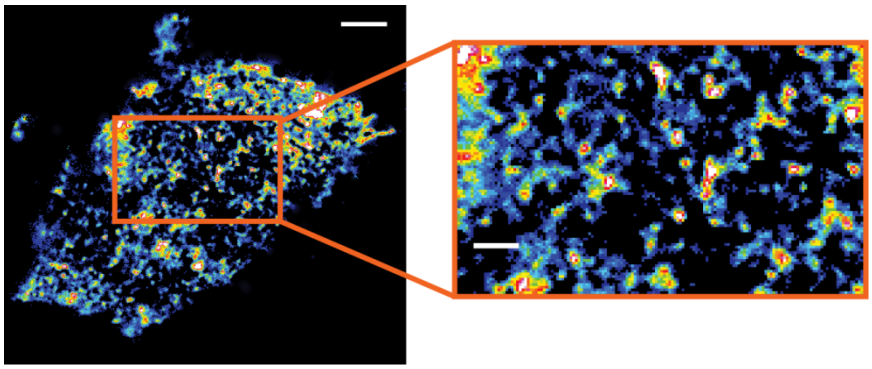

Figure 3.14. Zoom of cell region on FRET imaging between caveolin-1-EGFP and TRPV1-TagRFP. Scale bar in FRET image: 5 μm; zoom of the cellular region; scale bar: 2 μm

3.4 Experimental procedures

3.4.1 Engineering of labeled-TRPV1 vectors

We constructed a series of GFP-mutant of TRPV1 for FRET measurements with commercial plasmids target to microtubules and caveolin-1. The expression vector TRPV1-E^0GFP was generated by site-direct mutagenesis of p-TRPV1- EYQ1 (158) using the following primers:

Y203T: 5'- CAACCACTACCTGAGCACCCAGTCCGCCCTGAGCAAA-3'

Q222E:5'-CGCGATCACATGGTCCTGCTGGAGTTCGTGACCGCCGCCGGG-3'

For the construction of the plasmid encoding for TRPV1-EGFP chimera was generated by site direct mutagenesis of p-TRPV1-E^0GFP (described in ref.(145)) using the following primer:

S65T: 5'-GTGACCACCCTGACCTACGGCGTGCAGTGCTTC-3'

The TRPV1-TagRFP plasmid was constructed by cloning TRPV1 from TRPV1-YFP (a kindly gift from Wei Cheng, Department of Physiology and Membrane Biology, University of California, Davis, CA) and its activity upon transfection was tested according to Ref. (159). We performed a cut and paste cloning by using HindIII-SmaI sites on TRPV1-YFP plasmid and TagRFP vector (provided by Evrogen). Then we inserted the TagRFP fragment into plasmid encoding for TRPV1. An additional round of single point mutation was performed for remake the TagRFP gene in frame.

3.4.2 Cell culture and transfections.

Transfections of all constructs were performed in CHO K1 cells. CHO K1 were provided from the American Type Culture Collection (CCL-61 ATCC) and were grown in Ham's F1"K medium supplemented with 10% of Fetal Bovine Serum at 37°C and in 5% CO_2. Transfection of all constructs was carried out using Lipofectamine reagent (Invitrogen,) according to the manufacturer's instructions. For live imaging cells were plated 24h before transfection onto 35-mm glass bottom dish (WillCo-dish GWSt-3522)

3.4.3 Fluorescence imaging by confocal laser scanning microscopy (CLSM) and by Total Internal Reflection Fluorescent microscopy (TIRFM)

Cell fluorescence was analyzed using a confocal microscope Olympus FluoView 1000-ASW-2.0 (Japan) or a Leica TCS SP2 both equipped with an Ar-Laser for excitation at 458, 476 (only for Leica SP2) 488 and 514 nm and with a HeNe-laser for excitation at 543, 561 (only for Leica SP2) and 633 nm. A diode laser was used for excitation at 405 nm. Glass bottom Petri dishes containing transfected cells were mounted in a thermostated chamber and viewed with a 63x 1.4 NA planApo oil-immersion objective (Olympus) or 40x 1.25 NA oil-immersion objective (Leica) while setting the confocal pinhole at 1 Airy unit.

Cell membrane fluorescence was analyzed using a Leica AF6000 microscope in total internal reflection fluorescence mode, with a penetration depth of the evanescent wave below 100 nm. Images were acquired by laser-exciting the green-emitting fluorophores at 488 nm and the red-emitting TagRFP at 561 nm. In all cases, a 100x oil-immersion objective (NA 1.47) was employed. Fluorescence detection was ensured by a cooled EM-CCD Hamamatsu C1900-13. Glass bottom Petri dishes containing transfected cells were mounted in a thermostated chamber.

Live cell imaging was always performed at 37°C in a 5% CO_2 atmosphere.

3.4.4 Cell calcium measurement.

The fluorescent calcium indicator Calcium Crimson was adopted for all the measurements. The fluorescence indicator was dissolved in Pluronic F-127 to facilitate cell loading. We added the Pluronic solution to cells kept in PBS buffer to obtain a final loading concentration of 10 μM. Then we incubated the cell with the indicator at room temperature for 1 hour. The effect of receptor activation was evaluated by CLSM by exciting at 545 nm and collecting the emission in the 560-660 nm wavelength range. Temporal stacks were acquired with 1 s frame rate in both basal and agonist-stimulated conditions.

3.4.5 FRET measurements and data analysis.

FRET measurements between TRPV1-E^0GFP or TRPV1-TagRFP and TagRFP-αT were carried with a Leica TCS SP2 inverted confocal microscope (Leica Microsystems AG, Wetzlar, Germany). 63x (NA 1.4) planApo oil immersion objectives were used while setting the confocal pinhole at 1 Airy unit. FRET was performed by the sensitized emission technique under 488 nm for donor TRPV1-

YFP excitation and 405 nm for donor TRPV1-E^0GFP. Fluorescence emission of the RFP-αT acceptor was detected at 600-640 nm.

FRET imaging between caveolin-1-EGFP and TagRFP-αT was carried out by a Leica AF6000 fluorescence microscope in Total Internal Reflection mode (TIRFM), with a penetration depth of the evanescent wave less than 100 nm. Fluorescence was collected by using a 100x (NA 1.47) oil-immersion objective and was recorder cooled EM-CCD (Hamamatsu C1900-13). Acquisition settings were as in the following: in cell co-transfected with TRPV1-TagRFP and caveolin-1-EGFP we excited EGFP (donor) at 488 nm and we collected the RFP emission (acceptor) at 604-620nm and 660-679 nm. FRET analysis was carried out with a custom-made plugin of the ImageJ software (145)

3.4.6 Colocalization experiments.

Imaging was carried out with a Leica SP5 inverted confocal microscope. 40x (NA 1.25) planApo oil immersion object was used while setting the confocal pinhole at 1 Airy unit. Excitation of caveolin-1-EGFP was performed at 458 nm and fluorescence emission was collected in the range 470-520 nm. Excitation of TRPV1-TagRFP was performed at 561 nm and fluorescence emission was collected in the range 570-700 nm.

Chapter

4

Temporal Image Correlation Spectroscopy: temporal dynamics of TRPV1 and TRPV1-microtubule complex on membrane

In chapter 3 we demonstrated by FRET the binding between membrane TRPV1 and tubulin dimers belonging to integer microtubule protofilaments. FRET, however, offers a still picture of this interaction and does not provide details on the interplay between TRPV1 diffusion and binding. To address this point, in this chapter we investigate the average diffusion properties of TRPV1 on the membrane by temporal Image Correlation Spectroscopy (tICS). tICS is a correlation technique particularly suitable for measuring average dynamic properties of membrane proteins (160-162),. The theoretical background of tICS is sketched in section 4.1. In section 4.2 we demonstrate that membrane TRPV1 is subdivided in at least two components, which differ significantly in terms of average diffusion rates. The slower component is identifiable with the functional receptor, since it becomes predominant upon agonist stimulation. Finally, in section 4.3 we combine tICS with FRET to unveil the average diffusion properties of the complex between microtubules and TRPV1. By this strategy we demonstrate that only the slower

receptor pool does interact with microtubules. This finding links unequivocally the functional state of the receptor with microtubule binding.

4.1 Correlation spectroscopy: general concept and application to imaging

In the last decades, a remarkable progress in the comprehension of dynamics and interactions of fluorescently-labeled biomolecules was brought about by Fluorescence Correlation Spectroscopy (FCS) (163). FCS monitors the spontaneous fluctuations of fluorescence intensity arising from any process that changes the number or brightness of fluorophores in a very small volume. Fluctuations are produced by molecular transit across the observation volume and/or any chemical reaction that modifies the photophysical properties of the fluorophores (Fig. 4.1). The observation volume must be small in order to contain only a few fluorophores at a time, thus limiting dynamic averaging effects that would damp fluctuation intensities (164). An observation volume of about 1 femtoliter (fl) can be produced by focusing a laser beam through a high numeric aperture objective and collecting the emitted fluorescence through a pinhole, as realized in confocal microscopy setups (Fig. 4.1). A volume of 1 fl would contain on average one molecule at any time when the solution concentration is about 60 nM. In FCS the diffusion dynamics is recovered by calculating the autocorrelation of fluorescence emission, in order to reveal the recurrence of intensity fluctuations in the time domain.

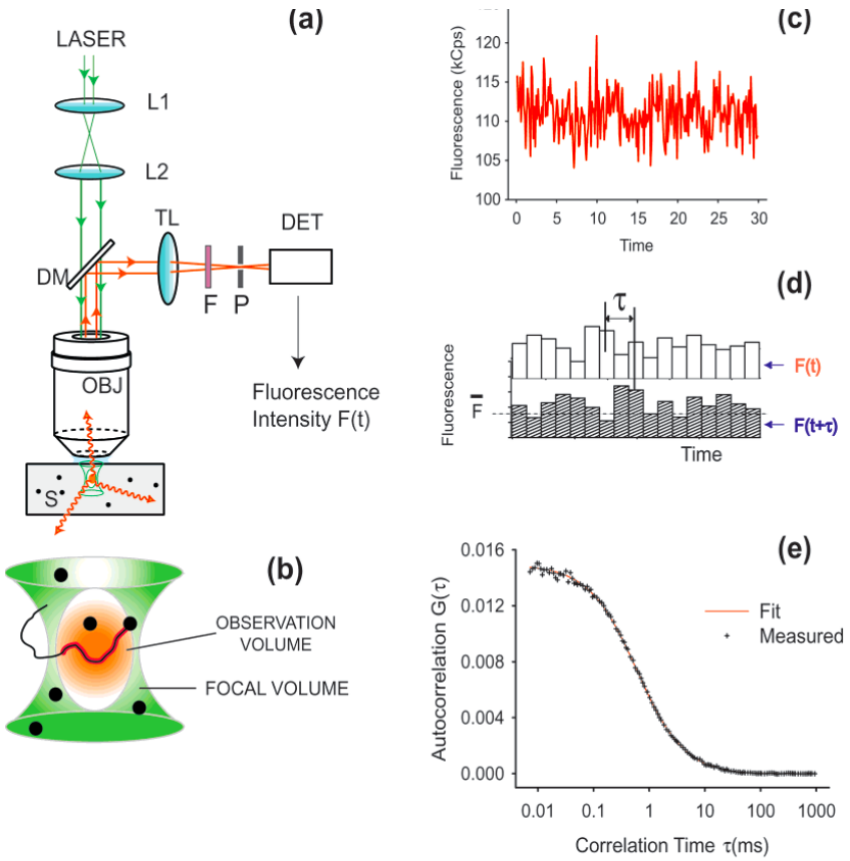

Figure 4.1: **Fluorescence Correlation Spectroscopy**. (Left) Experimental setup for FCS. (a) A laser beam is first expanded by a telescope (L1 and L2), and then focused by a high-NA objective lens (OBJ) on a fluorescent sample (S). The epifluorescence is collected by the same objective, reflected by a dichroic mirror (DM), focused by a tube lens (TL), filtered (F), and passed through a confocal aperture (P) onto the detector (DET). (b) Magnified focal volume (green) where the sample particles (black circles) are illuminated. (Right) (c) A typical fluorescence signal, as a function of time. (d) Portion of the same signal in panel c, binned, with an expanded time axis and average fluorescence $\langle F(t) \rangle$. The signal is correlated with itself at a later time ($t+\tau$) to produce the autocorrelation $G(\tau)$. (e) Measured $G(\tau)$ describing the fluorescence fluctuation of molecules due to diffusion as observed by FCS. Adapted from (165)

A natural evolution of the FCS concept is represented by Image Correlation Spectroscopy (ICS) (166). In ICS, a spatiotemporal autocorrelation function is calculated from *images* of fluorophores collected through either a confocal scanning microscope (where detectors are photomultipliers or avalanche diodes) or a TIRF microscope (where detectors are highly-sensitive CCD cameras). The introduction of the spatial dimension in the calculus of the autocorrelation helps to identify spatial structures and characteristics of diffusion that otherwise would not be noticed. Notably, ICS reveals only dynamic processes occurring in a time window comparable or slower than the frame rate. Modern confocal and TIRF microscopes allow fast acquisition rates of about 1-30 milliseconds. ICS-based techniques are largely applied to follow diffusion processes occurring in this time-scale, particularly on the membrane (167).

It is worth noting that meaningful interpretation of autocorrelation data is based on a strong assumption that is seldom stated in the descriptions of fluorescence correlation spectroscopies: the observed system should be space and time-invariant (168). At first sight, this condition could appear inapplicable to living systems, owing to their constant modification. Nevertheless, FCS/ICS measurements on biological samples are usually restricted to small spatial regions and they last for times not exceeding a few seconds (169). In most cases, the latter conditions ensure nearly “stationary state” for all visible processes occurring in the same regions and over the same collection time.

4.1.1 Temporal Image Correlation Spectroscopy

Temporal Image Correlation Spectroscopy (tICS) is an image correlation method where only the temporal autocorrelation of an image stack series is calculated, thus averaging the recorded dynamics over a given spatial area of the sample. This strategy can be assimilated to the parallel collection of several single-point FCS traces in different spatial locations, in order to maximize the signal-to-noise ratio of the measurement. tICS was used successfully to characterize the dynamics of several membrane proteins including integrins (160,161), wild-type cystic fibrosis transmembrane conductance regulator (CFTR) channel (162), and sodium-hydrogen exchange regulatory factor 1 (NHERF-1). In many cases, tICS results were confirmed by other diffusion measurements by alternative techniques such as FRAP or single particle tracking.

Starting from the generalized spatiotemporal correlation (Appendix A, Eq A.1), tICS is associated with an autocorrelation function of the form:

$$G(0,0,\tau) = \frac{\langle F_a(x,y,t) \cdot F_b(x,y,t+\tau) \rangle}{\langle F_a(x,y,t) \rangle_t \cdot \langle F_b(x,y,t+\tau) \rangle_{t+\tau}} - 1, \qquad [4.1]$$

where *x,y* are the spatial coordinates on the image plane (Eq. A.1).

Experimentally, a temporal stack of images is collected and then the autocorrelation is calculated following Eq. 4.1 for each pixel of the stack. Meaningful tICS measurements require the frame rate to be appropriately matched to the time scale of the diffusion process under investigation.

The analytical forms of $G(0,0,\tau)$ are rapidly calculated from general solutions of Eq. 4.1. For 3D free diffusion imaged by a Gaussian PSF, Eq. 4.1 reduces to (167) :

$$G_{3D}(0,0,\tau) = G(0,0,0) \cdot \left(1 + \frac{\tau}{\tau_D}\right)^{-1} \cdot \left(1 + \frac{\tau}{S^2 \tau_D}\right)^{-1/2}, \qquad [4.2]$$

where $S = \sigma_z/\sigma_{xy}$ is the ratio between the axial and the radial waists of the PSF and τ_D is related to the diffusion coefficient *D*, by:

$$D = \frac{\sigma_{xy}^2}{4\tau_D}. \qquad [4.3]$$

Protein diffusion on membranes, however, is amenable to a 2D diffusion description, namely:

$$G_{2D}(0,0,\tau) = G(0,0,0) \cdot \left(1 + \frac{\tau}{\tau_D}\right)^{-1}. \qquad [4.4]$$

Given our interest in processes occurring within the plasma membrane, further elaborations will concern only the 2D case.

When more than one molecular species are diffusing into the imaged area, the overall autocorrelation can be written as a sum of components expressed by Eq. 4.4, each one associated with a specific characteristic diffusion time $\tau_{D,i}$:

$$G_{2D}(0,0,\tau) = \sum_i G_i(0,0,0) \cdot \left(1 + \frac{\tau}{\tau_{D,i}}\right)^{-1} . \qquad [4.5]$$

In eq. 4.5 $G_i(0,0,0)$ represents the amplitude of autocorrelation function due to the component *i*. $G_i(0,0,0)$ values are usually recovered as empirical parameters from actual autocorrelation measurements, because they are connected in a complex way to both the concentration and the intrinsic molecular brightness of the *i*-component.

A very interesting condition occurs when the diffusing particle has very long (ideally infinite) characteristic diffusion time (immobile fraction). An "immobile" fraction may originate from an extended aggregation of the diffusing molecule triggered by some specific biochemical stimuli. For the simplest case of one diffusing moiety in presence of immobile fraction, Eq. 4.4 become:

$$G_{2D}(0,0,\tau) = G(0,0,0) \cdot \left(1 + \frac{\tau}{\tau_D}\right)^{-1} + g_\infty , \qquad [4.6]$$

where the time offset g_∞ stems from the presence of the immobile component with $\tau_D \to \infty$.

Assuming constant molecular brightness, the fraction of immobile population X_{imm} can be calculated with (167):

$$X_{imm} = \frac{g_\infty}{G(0,0,0) + g_\infty} . \qquad [4.7]$$

Eq.4.6 will be used throughout the chapter to analyze experimental data.

.

4.2 Average membrane diffusion properties of TRPV1

In this section we shall describe the use of tICS to measure the average membrane diffusion of TRPV1 in the basal and activated states.

4.2.1 Calibration of tICS technique

Initially, the reliability of the tICS analysis protocol was put to the test. Fluorescent nanospheres of 40 nm were imaged in a water/glycerol solution of known viscosity (109 centipoises at 20°C) by using a CLSM. For each sample, 300 images were sequentially acquired with a frame rate corresponding to $\Delta\tau$ = 65 ms between two consecutive images. $G(0,0,\tau)$ was calculated according to Eq. 4.1 and the diffusion coefficient D of the nanospheres was obtained by fitting $G(0,0,\tau)$ *vs.* τ to Eq. 4.2 (Fig. 4.2). The fitting yielded D=(4.4±0.1)*10^{-2} (# 10 experiments). Note that the radial resolution σ_{xy} of the confocal microscope had been previously determined by analyzing the diffraction-limited image of fixed nanoparticles with 100 nm diameter (§ 2.1.1). In excellent agreement with the recovered data, the Stokes-Einstein law yielded D=4.9*10^{-2} $\mu m^2/s$ for the adopted solution viscosity and temperature (Fig. 4.2), thus validating our tICS protocol.

4.2.2 tICS on TRPV1 at basal state and under stimulation

At first, only the receptor at basal state was investigated. tICS was applied to CHO cells transiently expressing TRPV1-YFP; YFP selection was motivated by its being the brightest variant among the available TRPV1-chimeras, thus ensuring the maximum S/N ratio. By exciting at 488 nm in a CLSM, we collected at maximum frame rate ($\Delta\tau$=26 ms between two consecutive images, "fast acquisition" mode) 300 sequential images of 10 μm x 10 μm membrane areas. The collection range was set to 500-600 nm. The excitation power was minimized to a level ensuring that little (<5%) if none photobleaching occurred over time (note that the presence of photobleaching is known to yield overestimated diffusion coefficients (167)).

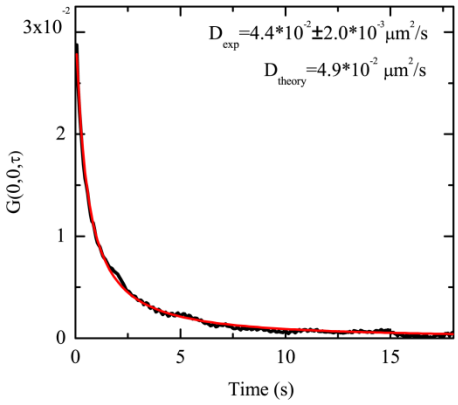

Figure 4.2. tICS calibration. tICS curve obtained by imaging a dispersion of fluorescent microspheres (diameter=0.04 μm) in a mixture of water/glycerol (85% w/w). The measurement was performed using the same acquisition parameters used for living cells, namely λ_{exc}=488 nm, emission collected between 500-600 nm, and 65 ms frame rate (300 frames).

Fitting of tICS curves to Eq. 4.6 (Fig 4.3) showed rather fast loss of temporal correlation (τ=3.1±2.2 s), with an average diffusion coefficient D_{fast}= (7±2)*10^{-3} μm^2 (Tab. 4.1) (Fig. 4.3). This D_{fast} value is in agreement with the typical D values of transmembrane receptors (10^{-2}-10^{-3} μm^2/s) and about four orders of magnitude smaller than the D of cytosolic proteins (170).

Although in "fast acquisition" mode no more than 300 images could be recorded, $G(0,0,\tau)$ was dissipated at the end of collection (7.8 s) by about 20% (Fig. 4.3). In order to reveal any additional slower diffusion component, we acquired for 600 s by using a longer time lag between frames ($\Delta\tau$=2s, "slow acquisition" mode). In these conditions, $G(0,0,\tau)$ could be fitted to a sum of two exponential decays (Eq. 4.8) where the first component corresponded to the fast population ($\tau_{D\,fast} \approx 3$ s) previously detected.

$$G(0,0,\tau) = G_{fast}(0,0,0)\left(1+\frac{\tau}{\tau_{D\,fast}}\right)^{-1} + G_{slow}(0,0,0)\left(1+\frac{\tau}{\tau_{D_{slow}}}\right)^{-1} + g_{\infty}. \qquad [4.8]$$

Importantly, the fit yielded $g_{\infty} \approx 0$, indicating that almost no immobile fraction of TRPV1-YFP exists at very long times.

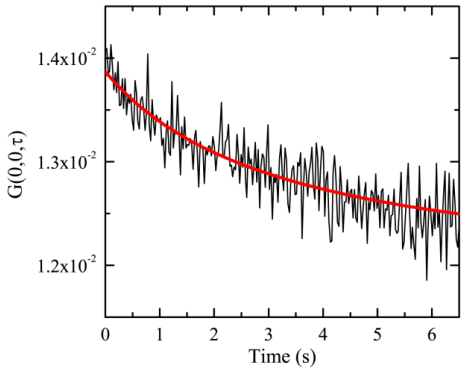

Figure 4.3. Representative autocorrelation function of membrane TRPV1-YFP acquired at Δt=26 ms ("fast" acquisition mode). Autocorrelation function is reported together with the relevant fit to a 2-dimension diffusion model.

The slower TRPV1 population was associated with $\tau_{D_{slow}}$ =370±189 s, yielding an average diffusion coefficient D_{slow} = (6±4)*10^{-5} μm^2/s (Table 4.1). Thus, the two diffusive components were separated by about 2 orders of magnitude, although they displayed similar average autocorrelation amplitudes (Table 4.1). We should stress again that the amplitude values do not necessarily reflect the relative abundance of the two populations (§ 4.1.1). Only variations of their relative proportions would be indicative of concentration changes.

The relevance of these results prompted us to verify whether the TRPV1 diffusion properties at basal state were independent from the protein expression levels. To do this, we subdivided the analyzed cells into three groups with different YFP emission intensities and calculated for each the average *D* value (Fig. 4.5). Our analysis highlighted that no statistical differences among diffusion coefficients were found at different expression levels.

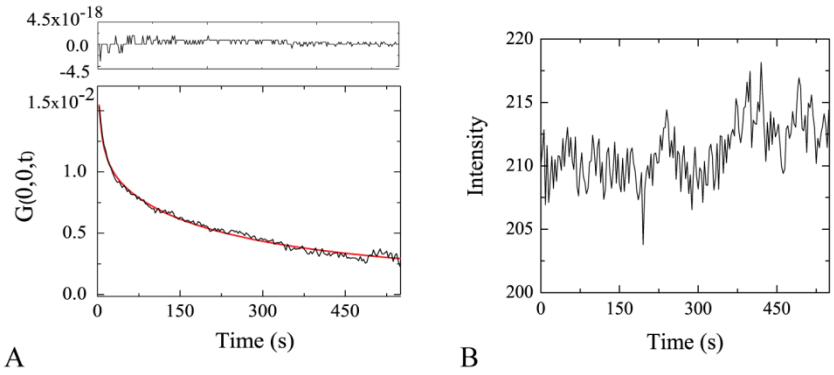

Figure 4.4. Representative autocorrelation function of membrane TRPV1-YFP acquired at Δt=2 s ("slow" acquisition mode).. (A) A representative autocorrelation function of membrane TRPV1-YFP is reported together with the relevant fit to a 2-dimension diffusion model. (B) Temporal trace of fluorescence intensity fluctuations showing negligible photobleaching.

Starting from these findings on basal state of the receptor, we set out to investigate whether stimulation by RTX agonist (§ 3.2.1) could modulate the diffusion properties of TRPV1. Remarkably, agonist activation modified neither the presence of the two diffusing components, nor their respective diffusion coefficients. The relative correlation amplitudes, however, changed significantly as $G_{slow}(0,0,0)$ became predominant (Tab. 4.1). The constancy of the diffusion coefficients suggested that the agonist induced little modification of the structural and/or oligomerization property of both TRPV1 components. Additionally, the fluorescence lifetime of TRPV1-YFP in the absence and in the presence of RTX remained unchanged (Tab. 4.1), indicating that the intrinsic brightness of the protein reporter did not affect the observed changes in autocorrelation amplitudes. These results indicated that the changes of autocorrelation amplitudes were produced by a concentration increase of slow-moving TRPV1. In this perspective, the slow TRPV1 component identifies in part or totally with the functional receptor, i.e. the TRPV1 that can undergo stimulation by RTX agonist.

Table 4.1. Diffusion parameters derived from tICS measurements on membrane TRPV1-YFP and fluorescence lifetime of TRPV1-YFP. % AC: per cent of autocorrelation amplitude. D: diffusion coefficient. IF: Immobile fraction percentage. The %AC, D, and IF values are expressed as mean ± standard deviation.

	tICS				Fluorescence lifetime
	% AC	D ($\mu m^2/s$)	IF (%)	# cells	τ
Basal	40±12	$(7\pm2)*10^{-3}$	0	32	3.08±0.04
	60±10	$(6\pm4)*10^{-5}$			
Nocodazole	25±15[a]	$(9\pm8)*10^{-2}$	35±15	30	2.99±0.08
	40±20[a]	$(3\pm2)*10^{-4}$			
Cytochalasin D	60±20	$(2\pm1)*10^{-3}$	0	10	-
	40±20	$(2\pm1)*10^{-5}$			
RTX	10±10	$(3\pm2)*10^{-3}$	0	20	2.99±0.09
	90±10	$(5\pm3)*10^{-5}$			

[a] Note that the ratio between the autocorrelation amplitude (AC) of fast and slow populations in nocodazole treatment cells (25%/40%) is the same of that calculate in basal condition (60%/40%)

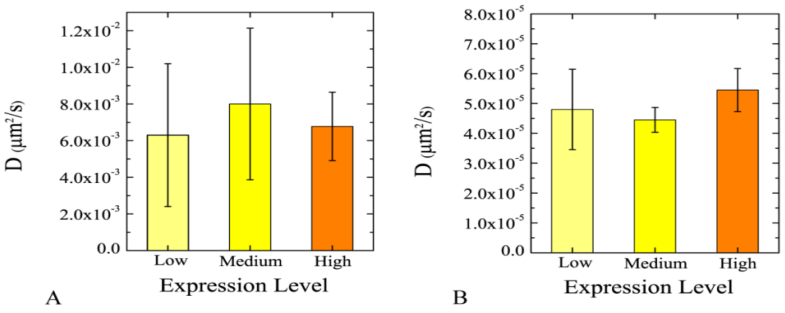

Figure 4.5. Diffusion coefficients *vs.* cellular expression levels. The histograms show the dependence of fast (A) and slow (B) diffusion coefficients upon protein expression level in living cells at basal condition. The results are divided in three sets of expression levels depending on fluorescence intensity values (a.u.): low expression level (from 50 to 150 a.u.), medium expression level (from 151 to 350 a.u.), and high expression level (from 351 to 550). Each column represents the statistical analysis of 4 cells (mean ± standard deviation).

4.3 Temporal dynamics of TRPV1-microtubule complex

In section 4.2 we demonstrated that membrane TRPV1-YFP is characterized by at least two diffusing components with fairly different diffusion coefficients. The clear demonstration of TRPV1-microtubule interactions in living cells by FRET in Chapter 3 prompted us to clarify whether: 1) microtubule integrity affects the dynamic properties of the receptor at membrane level, 2) one or both components interact with microtubules. These issues are discussed in the following sections.

4.3.1 Effect of microtubule disassembly on TRPV1 dynamics

In order to verify the effect of microtubule integrity on TRPV1 dynamics, we carried out tICS experiments under cell treatment with nocodazole. Measurements were performed on CHO cells expressing TRPV1-YFP. Nocodazole treatment led to a 10-fold increase of diffusion coefficient values of both fast and slow subpools ($p < 0.0025$, # = 30 cells). The ratio between the correlation amplitudes of the two populations was, however, virtually unaffected (Tab. 4.1). On the other hand, the mobility increase of TRPV1 was not correlated to non-specific cytoskeletal disruption effects. In fact, the addition of actin-disrupting cytochalasin *D* affected neither the diffusion coefficients nor the relative correlation amplitudes (Tab. 4.1). At odds with what observed in the presence of intact microtubules, autocorrelation curves showed large asymptotic offsets (~35%) upon nocodazole treatment. This effect was attributed to a significant level of immobile fraction, on account of the negligible photobleaching of YFP in our measurement conditions. Additionally, nocodazole was found to be non-influent on the intrinsic brightness of the YFP reporter, as witnessed by the constancy of the average fluorescence lifetime of TRPV1-YFP (Tab. 4.1). These findings suggest that integer microtubules are essential to maintain the physiological dynamic states of the receptor.

4.3.2 Analysis of the dynamics of TRPV1-μT complex at basal state

In order to identify whether one or both TRPV1 components interact with microtubules, tICS measurements were combined with FRET. tICS experiments were performed on cells in basal state expressing both TRPV1-E^0GFP (donor) and TagRFP-αT (acceptor). Images in the donor (480-560 nm) and FRET (615-715 nm)

channels were acquired over time by selectively exciting the donor alone at 405 nm. We then calculated separate autocorrelation functions from the donor and FRET channels (Fig. 4.7). Analogously to previous experiments (§ 4.2), image temporal stacks were recorded in "fast" and "slow" acquisition modes, in order to recover fast and slow receptor dynamics.

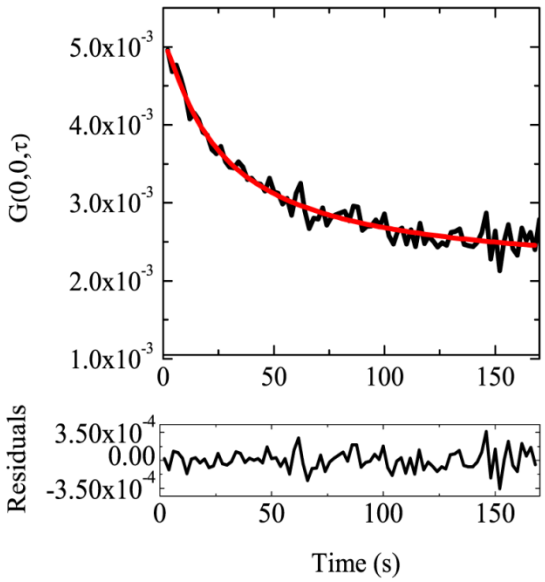

Figure 4.6 Representative autocorrelation function of membrane TRPV1-YFP upon nocodazole administration. The image sequence was acquired at Δt=2 s. Autocorrelation function is reported together with the relevant fit to a biexponential 2D diffusion model. The offset calculated by fitting is 36%.

The autocorrelation analysis of the donor channel was in complete agreement with those collected for TRPV1-YFP at basal state (D_{fast} = 5±1*10^{-3} μm^2/s, D_{slow} = 9±5*10^{-5} μm^2/s). This confirmed that YFP replacement by E^{0}GFP had no effect on the mobility of the fusion construct, as expected by the close structural similarity of these fluorescent proteins.

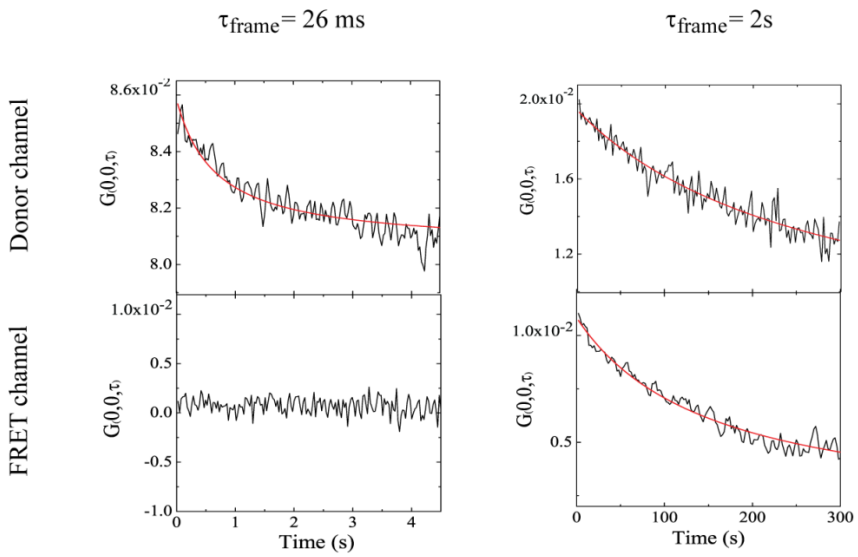

Figure 4.7. tICS-FRET analysis. Autocorrelation function of intensity fluctuations collected in the donor channel (TRPV1-E^{0}GFP, emission in the 480-560 nm range) and in the acceptor/FRET channel (TagRFP-αT, emission in the 615-715 nm range). Excitation was set to 405 nm. Left panels refer to "fast" acquisition mode, whereas right panels refer to "slow" acquisition mode.

The autocorrelation curve of the FRET channel was nearly equivalent to TRPV1-E^{0}GFP in "slow acquisition" mode (D_{slow} = 4±9*10^{-5} μm^2/s). On the other hand, when the fast acquisition mode was adopted, we observed no temporal dependence of autocorrelation in the FRET channel (Fig. 4.7). Control experiments on cells expressing TRPV1-E^{0}GFP or TagRFP-αT alone (Fig. 4.8) confirmed that the observed pattern was associated only with the interaction between the receptor and microtubules. In cell expressing only the acceptor, the excitation at 405 nm led to null correlation when recording at >615 nm, in agreement with null absorption of TagRFP in the violet region of spectrum (§ 3.1.3, Fig. 3.3). The selection of the E^{0}GFP/ TagRFP pair was indeed motivated by this photophysical feature, since it prevents mixing of acceptor dynamics with that of the complex. In cells expressing only the donor, a small amount of cross-talk intensity was visible in the FRET channel by exciting at 405 nm. Yet this signal was poorly autocorrelated, likely owing to the interference of detector noise (Fig. 4.8A). Accordingly, the signal

autocorrelation was present only for the fluorescence acquired in the donor channel (Fig. 4.8B).

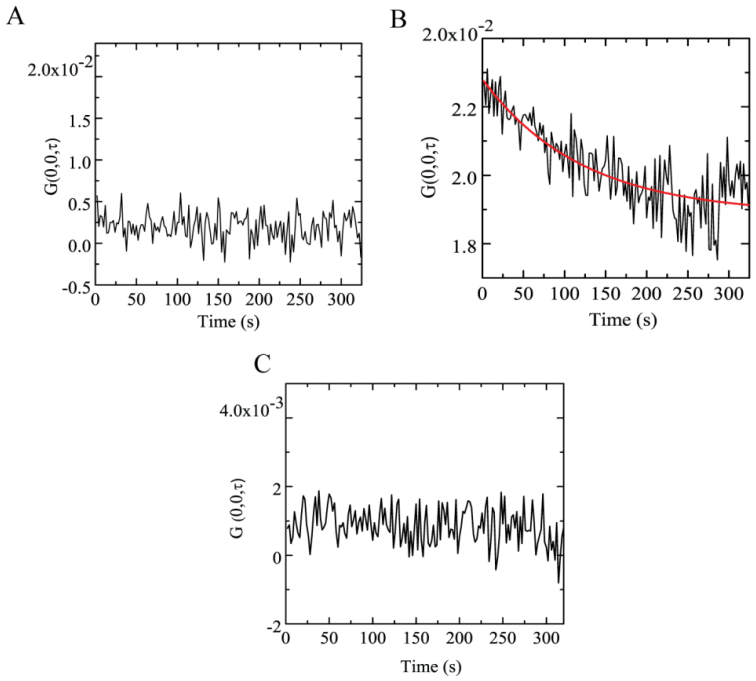

Figure 4.8. **Control experiments on cell expressing TagRFP-αT or TRPV1-E^{0}GFP.** Upon excitation at 405 nm of cells expressing only TRPV1-E^{0}GFP, we show the autocorrelation of the "cross-talk" signal collected in the emission interval λ_{em}=615-715 nm (A), and of the "donor" signal collected in the emission interval λ_{em}=480-560 nm (B). (C) Upon excitation at 405 nm of cells expressing only TagRFP-αT, we show the autocorrelation of the "bleed-through" signal collected in the emission interval λ_{em} =615-715 nm. Note that a positive correlation is present only in the donor emission channel, while cross-talk and bleed-through signals are not correlated. Fit of the donor autocorrelation (red line in panel B) to a 2D diffusion model yielded τ_D=140 s.

4.3.3 Analysis of the dynamics of TRPV1-microtubules complex upon agonist stimulation

In section 4.2.2 we demonstrated that only the slow TRPV1 subpool is functional, i.e. sensitive to agonist stimulation. Later, (§ 4.3.2) we identified the slow TRPV1 subpool with the microtubule-interacting component, and we stressed the relevance of microtubule integrity to maintain the physiological dynamic states of the receptor. These findings prompted us to investigate how receptor stimulation by RTX modulates the microtubule-TRPV1 dynamic interaction by using tICS-FRET. Much alike the basal state, only the slow diffusing component was found to interact with microtubules. Yet, tICS-FRET afforded D_{slow} =(3±3)*10^{-5} μm^2/s. This value was statistically smaller (p=0.020) if compared to the diffusion coefficient of the donor or of the complex in absence of the agonist. This result indicated that agonist stimulation slowed the membrane diffusion of TRPV1-microtubule complex.

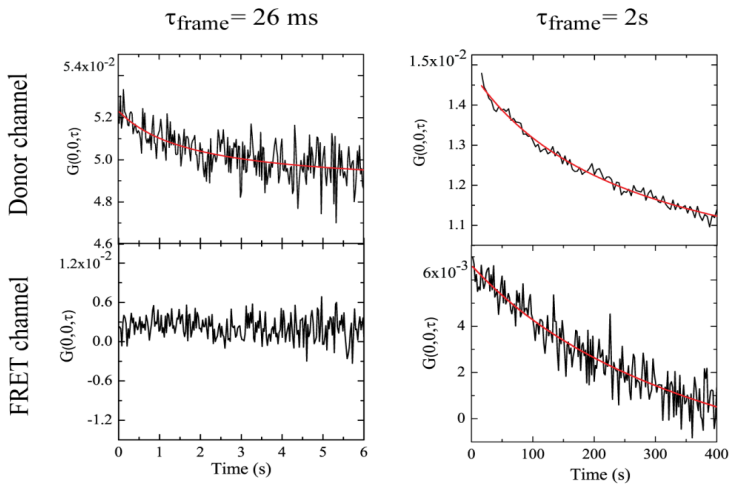

Figure 4.9. tICS-FRET analysis on RTX-stimulated TRPV1-E^{0}GFP. Autocorrelation function of intensity fluctuations collected in the donor channel (TRPV1-E^{0}GFP, emission in the 480-560 nm range) and in the acceptor/FRET channel (TagRFP-αT, emission in the 615 - 715 nm range). Excitation was set to 405 nm. Left panels refer to "fast" acquisition mode, whereas right panels refer to "slow" acquisition mode.

4.4 Concluding remarks

In conclusion, tICS and tICS-FRET measurements revealed that TRPV1 membrane dynamics is characterized by at least two diffusing components ("fast" and "slow") with fairly different mobilities. The "slow" component corresponds in part or on the whole to the functional form of the receptor and interacts in part or globally with integer microtubules. This pattern is not qualitatively modified by receptor activation by agonist RTX, although stimulation slows the membrane diffusion of TRPV1-microtubule complex. On the other hand, microtubule integrity is essential to maintain the physiological dynamic states of the receptor. These findings confirm that microtubule integrity preserves the functionality of the receptor, as also suggested in section 3.2.2.

It is tempting to ascribe the lowered mobility of the slow TRPV1 component to its interaction with microtubules. Here, two non-exclusive situations can be envisaged: i) TRPV1 diffusion is slowed by reversible binding to microtubules, ii) TRPV1 is transiently confined in membrane regions and/or motion-guided by microtubules interaction. In chapter 6, we shall demonstrate that hypothesis ii) holds.

Intriguingly, the "fast" TRPV1 subpool does not interact with microtubules and it is depleted upon agonist stimulation. On account of these evidences, we hypothesize that the "fast" component could include an immature form of the receptor. We shall demonstrate the validity of this hypothesis in the next chapter.

4.5 Experimental Procedures

4.5.1 Cell culture and transfections.

In order to monitor the mebranne diffusion of TRPV1, CHO-K1 cells cultured onto 35-mm glass bottom were transfected with TRPV1-YFP plasmid, a kind gift from Wei Cheng (159) . The transfections were performed as described in §3.4.2

4.5.2 Temporal Image Correlation Spectroscopy (tICS) and tICS-FRET.

tICS and tICS-FRET measurements were carried out with an Olympus FluoView 1000-ASW-2.0 (Japan) confocal laser scanning microscope using a 63x (NA 1.4) planApo oil-immersion objective while setting the confocal pinhole at 1 Airy unit. For each measurement, a small section of the plasma membrane (about 13x13 μm^2) was imaged (26 ms/frame or 2 s/frame) by acquiring 300 images. In conventional tICS on TRPV1- YFP, we excited at 488 nm and collected the emitted fluorescence in the 500-600 nm range. In tICS-FRET, we excited at 405 nm, we collected donor and emissions in the 480-560 and 615-715 nm range, respectively. Image autocorrelation was obtained by the ICS Temporal plugin of ImageJ; fitting of autocorrelation curves was performed by a custom-made software running on IgorPro 6 or Origin.

4.5.3 Calibration of tICS technique

For tICS calibration we used a dispersion of fluorescent microspheres (diameter=0.04 μm) in a mixture of water/glycerol (85% w/w). Measurements were performed with a confocal microscopy Olympus FluoView 1000-ASW-2.0 using the same acquisition parameters set for living cells, namely excitation at 488 nm, collection of fluorescence emission in the 500-600 nm range, and 65 ms frame rate (300 frames). Image autocorrelation was generated by the ICS Temporal plugin of ImageJ; fitting of autocorrelation curves was performed by a custom-made software running under Origin.

5

Study of TRPV1 oligomerization in living cells: Homo-FRET imaging and Number and Brightness analysis

In chapter 4 we demonstrated that membrane TRPV1 is subdivided in at least two components with fairly different diffusion properties. The slowest component corresponds to the functional form of the receptor, whereas the faster component could represent an immature form of TRPV1. The functional form, either in whole or in part, binds and is stabilized by integer microtubules. In fact, microtubule disassembly leads to strong changes in the dynamic properties of the receptor, including the formation of a significant immobile fraction, and consequently to the impairing of ion channel activity. These findings suggest the presence of structural variants of the receptor on the membrane, likely associated to different oligomerization degrees. In literature, however, oligomerization of the receptor was estimated only in vitro (79,171,172). In order to clarify this issue, this chapter reports our studies on the aggregation state of the receptor in living cells. In section 5.1, by fluorescence anisotropy imaging (FAIM) associated to homo-FRET, we shall demonstrate that TRPV1 is already aggregated in basal condition and its oligomerization degree increases significantly upon microtubule disassembly. In section 5.2, by Number and Brightness (N&B) analysis, we shall investigate further

the oligomerization degree of the receptor at basal state and under agonist stimulation.

5.1 Fluorescence Anisotropy Imaging Microscopy (FAIM) on TRPV1

5.1.1 Homo-FRET theory and FAIM

At odds with more popular hetero-FRET (chapter 3), homo-FRET involves non-radiative energy transfer between fluorophores of the same kind characterized by small Stokes' shifts, to ensure adequate overlapping between absorption and emission spectra (173). Intensity ratios or lifetime measurements, however, can not be used for quantification of homo-FRET, because donor and acceptor are spectroscopically indistinguishable. The measurement of fluorescence depolarization upon non-radiative transfer, albeit just one of many ways to quantify hetero-FRET, is the most established method of detecting homo-FRET (174).

From a photophysical point of view, excitation of any fluorescent moiety with polarized light results in photoselection of fluorophores sharing a component of their absorption transition dipole moment with the polarization direction of the excitation light. Fluorescence emission, however, is partially depolarized with respect to excitation, owing to probe rotation occurring during the life of the excited state. The degree of depolarization is measured by resolving $I_{\parallel}$ and $I_{\perp}$ relative to the polarization of the excitation light. The concept of fluorescence anisotropy imaging microscopy (FAIM) is to measure the polarization orientation of the fluorescence relative to that of the excitation light in every image pixel. The fluorescence anisotropy *r* is conventionally defined as:

$$r = \frac{I_{\parallel} - GI_{\perp}}{I_{\parallel} + 2GI_{\perp}}, \qquad [5.1]$$

where $I_{\parallel}$ and $I_{\perp}$ are the fluorescence intensities with parallel and perpendicular polarizations with respect to excitation, and *G* is the calibration factor that accounts

for polarization effects of the collection optics. Fig. 5.1 illustrates the essential features of FAIM.

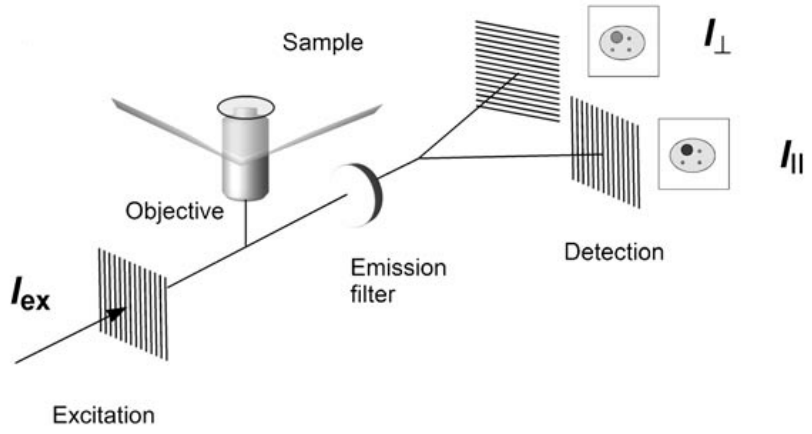

Figure 5.1. Fluorescence anisotropy imaging microscopy. Fluorescence-labeled molecules in a sample are excited with linearly polarized light (I_{ex}). The amount of depolarization that has occurred during the lifetime of the fluorophore is measured by resolving the fluorescence intensity parallel and perpendicular to the excitation polarization ($I_\parallel$ and $I_\perp$). Images of $I_\parallel$ and $I_\perp$ yield pixel-by-pixel anisotropy measurements, resolving molecular features related to polarization such as molecular rotation. (Adapted from (175))

Fluorescence depolarization is mainly due to rotational diffusion and FRET between molecules of different orientation (175). When molecular rotation is hindered, FRET is the main channel of depolarization. Fig. 5.2 depicts a classical context for homo-FRET measurements: a receptor membrane dimer is linked to two FPs whose transition dipoles are randomly oriented. Homo-FRET leads to depolarized emission, since the energy transfer does not maintain the polarization of the excitation light. Additionally, because the same fluorophore acts both as donor and acceptor, the transfer of energy is reversible, increasing the extent of depolarization (175). This "bouncing" excitation leads to a significant difference between the anisotropy of the reporter with a monomeric (r_{mono}) or a multimeric (r_{et}) receptor (175).

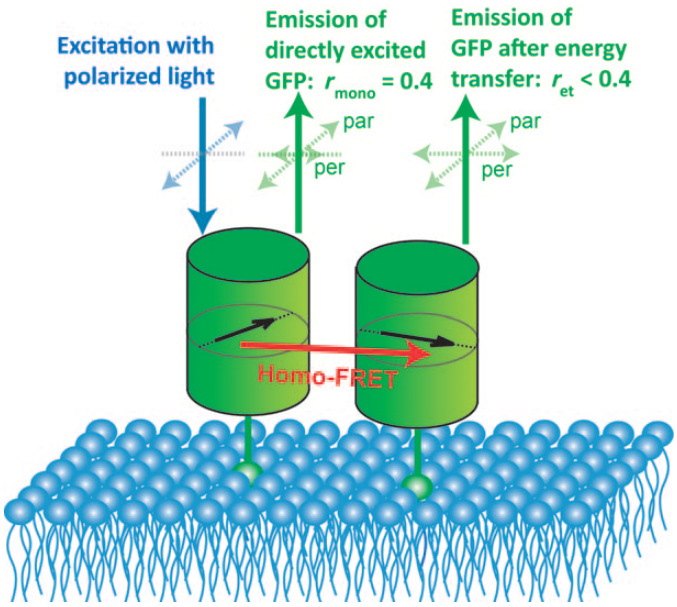

Figure 5.2. Schematic representation of homo-FRET in a dimer of GFP anchored to a membrane. Adapted from (176)

The loss of polarization upon homo-FRET affords an opportunity for cluster-size quantification. Indeed, the maximum amount of homo-FRET depolarization for a defined cluster occurs when the energy transfer has reached equilibrium, that is, a point where all molecules in the cluster have an equal probability of emitting a photon. Runnels and Scarlata (173) derived a set of equations to predict the amount of depolarization based on cluster size and inter-fluorophore distance within the cluster. The emission anisotropy arising from a cluster of N molecules is expressed by:

$$r_N = r_1 \cdot \frac{(1 + F \cdot \tau)}{(1 + N \cdot F \cdot \tau)} + r_{et} \cdot \frac{(N-1) \cdot (F \cdot \tau)}{(1 + N \cdot F \cdot \tau)}, \qquad [5.2]$$

where r_N the emission anisotropy for a single cluster, r_1 is the emission anisotropy for the initially excited molecule (or a monomer), r_{et} is the average anisotropy of fluorophores that are indirectly excited after homo-FRET (limiting

anisotropy), τ represent the average lifetime of the fluorophore, N is the number of fluorophores in the cluster, and F is Förster's transfer rate (§3.1.1, Eq. 3.1). For randomly oriented fluorophores, the limiting anisotropy approaches zero since $r_{et} = 0.016$ (173).

In homo-FRET studies the depolarization due to intrinsic rotational motion of fluorophore must be negligible (175). Apart from viscous intracellular regions such as the membrane, this condition can be simply accommodated for by using a fluorescent probe for which the characteristic rotation time Θ of the molecule is much larger than its lifetime. FPs share this property, as they display lifetimes in the 1-3 ns range and Θ >20 ns at the very low viscosity of aqueous environment. (177).

5.1.2 FAIM measurements on basal and stimulated TRPV1

As benchmark, we carried out homo-FRET / FAIM on proteins with a known state of oligomerization: monomeric YFP and EGFP, and a EGFP tetrameric chimera. All these proteins were excited at the same wavelength (488 nm) and imaged as freely-diffusing molecules in the cytoplasm of CHO cells. We found out $<r>$=0.30±0.03 and $<r>$=0.27±0.02 for monomeric EGFP and YFP, respectively, in good agreement with literature data (178). Conversely, tetrameric EGFP showed $<r>$=0.19±0.04, clearly indicating the presence of active homo-FRET.

Next, we carried out FAIM measurements on basal and RTX-activated TRPV1-YFP expressed on the plasma membrane of CHO cells (Fig. 5.4). YFP reporter was chosen on account of its small Stokes' shift that increases the Forster radius (R_0=5.11 nm (179)) and therefore the efficiency of homo-FRET.

Interestingly, we found out that basal TRPV1-YFP is associated with a significantly smaller $<r>$ with respect to monomeric YFP (Tab. 5.1), at odds with its hampered mobility due to membrane localization. The decrease of <r> can not be attributed to changes in the photophysics of emission, since YFP retains the same lifetime as free protein or conjugated to TRPV1 (Tab. 5.1). These data unequivocally demonstrate that the observed reduction in anisotropy due to homo-FRET among YFP reporters, thus indicating the aggregated form of the receptor at basal state. Agonist stimulation by RTX changed significantly neither the $<r>$ value, nor the YFP lifetime (Tab. 5.1).

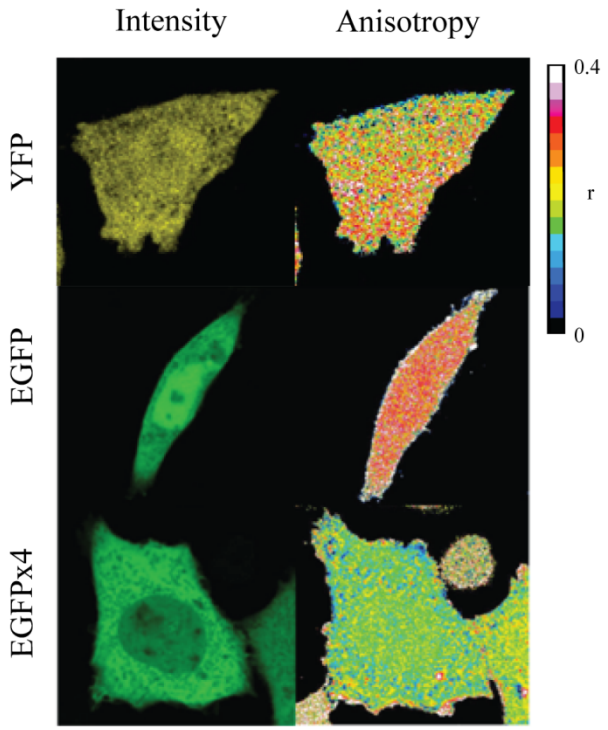

Figure 5.3. Anisotropy measurements on cells transfected with YFP, EGFP and EGFPx4. The intensity and anisotropy intracellular maps of YFP (upper panels), EGFP monomer (middle panels), and EGFP tetramer (lower panels) are shown.

Table 5.1. Average anisotropy and lifetime value of YFP and TRPV1-YFP at basal condition and upon administration of different drugs.

	<r>	<τ>	# cells
YFP	0.27±0.02	3.00±0.05	20
TRPV1-YFP	0.18±0.03	3.08±0.04	15
TRPV1-YFP + RTX	0.18±0.04	2.99±0.09	15
TRPV1 + Nocodazole	0.12±0.03	2.99±0.08	40
TRPV1 + Cytochalasin D	0.17±0.02	-	20

A semi-quantitative estimate of the aggregation state at basal and under agonist stimulation can be obtained by applying Eq. 5.2. The Förster's homo-transfer rate *F*

of YFP was calculated by Eq. 3.1 (§ 3.1.1) assuming inter-reporter distances from 4 to 10 nm. Then, the F values were used to determine r_N by setting r_1=0.27 (monomer YFP), $r_{et}=0$ (random orientation of homo-FRET acceptors), and τ=3 (YFP) ns in Eq. 5.2. Results are reported in Tab. 5.2. Experimental <r> values were consistent for dimers and/or tetramers under the assumption of YFP-YFP distances of 5-7 nm between dipoles. Larger distances would imply further clusterization of the receptor in physiological state. It should be reminded that TRPV1 was shown to adopt a tetrameric configuration in vitro with inter-subunit distance around 10 nm (§ 1.2) (79). Such a value is in keeping with a YFP-YFP distance of 5-7 nm if the size of 2 YFPs are taken into account.

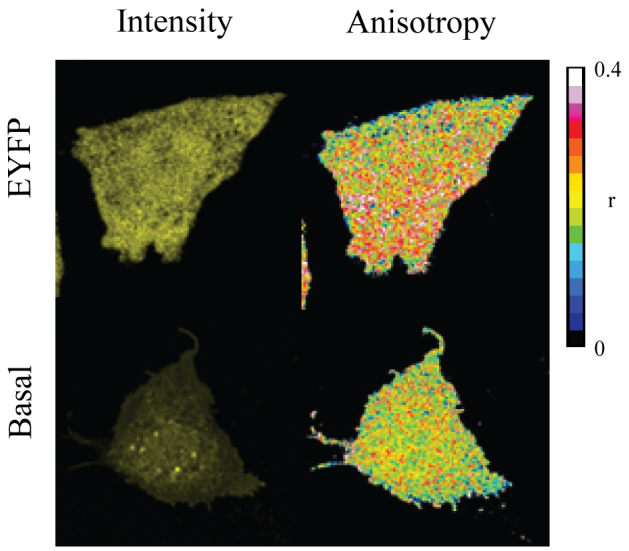

Figure 5.4. Fluorescence intensity and anisotropy images of cells expressing TRPV1-YFP at basal condition and upon RTX stimulation.

5.1.3 FAIM measurements on TRPV1 under microtubule disassembly

In chapter 4 we highlighted by tICS that microtubule disassembly produces a significant level of immobile receptor fraction (35% of the global autocorrelation amplitude). In order to investigate possible changes in TRPV1 oligomerization, we carried out FAIM experiments in cells treated with nocodazole.

Remarkably, microtubule disassembly led to $<r>=0.13\pm0.03$ without altering the YFP lifetime (Table 5.1). This strong reduction in anisotropy with respect to the basal state suggested an increase in homo-FRET triggered by a larger oligomerization degree of the receptor. Assuming that only a fraction of TRPV1 extensively aggregates, as advocated by the immobile pool in tICS measurements, Tab. 5.2 shows that large complexes of tens of TRPV1 units may make up for the observed reduction in average anisotropy.

On the other hand, the administration of actin-depolymerizing cytochalasin-D instead of nocodazole did not lead to an immobile TRPV1 fraction in tICS measurements (§ 4.3.1) and, coherently, had no effect on $<r>$ in FAIM experiments (Fig. 5.5, Tab. 5.1). These findings indicate that microtubule disassembly and the loss of microtubule-TRPV1 interaction leads to extensive receptor aggregation. It is tempting to attribute the observed loss of TRPV1 functionality upon microtubule disassembly to the non-physiological oligomerization state of the receptor.

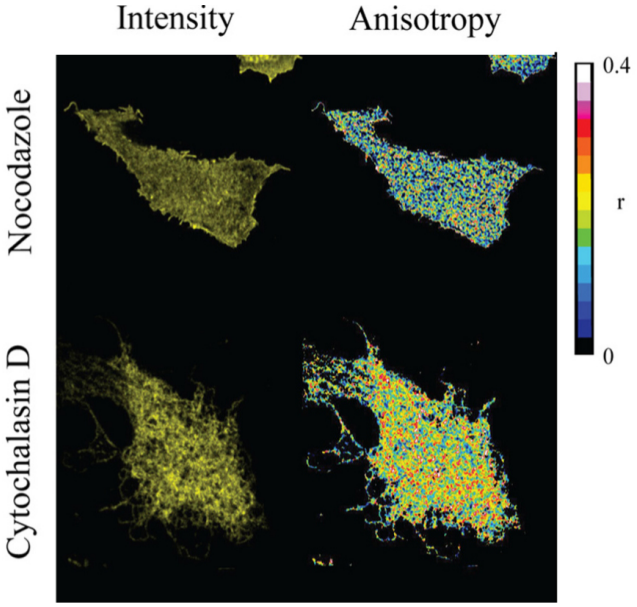

Figure 5.5. Fluorescence intensity and anisotropy images of cells expressing TRPV1-YFP upon nocodazole or cytochalasin D tretment.

Table 5.2 Expected anisotropy value depending on fluorophore distances and number of fluorophores for each cluster. The anisotropy values are calculated following the equation 5.2.

	Fluorophores distance (nm)						
Number of fluorophores for cluster	***4***	***5***	***6***	***7***	***8***	***9***	***10***
1	0.27	0.27	0.27	0.27	0.27	0.27	0.27
2	0.15	0.18	0.21	0.24	0.25	0.26	0.27
4	0.08	0.10	0.15	0.19	0.23	0.25	0.26
10	0.03	0.05	0.08	0.12	0.17	0.21	0.23
20	0.02	0.02	0.04	0.08	0.12	0.17	0.20

5.2 The Number and Brightness analysis

5.2.1. Photophysical background of N&B analysis

Number and Brightness (N&B) is an imaging method based on moment analysis of fluorescence fluctuations. N&B is particularly suitable for the detection and quantification of protein aggregation states (180-182) .

In N&B analysis, the average intensity $\langle k \rangle$ and variance σ^2 of a given pixel are defined according to the following formulas:

$$\langle k \rangle = \frac{\sum_i k_i}{K}, \qquad [5.3]$$

$$\sigma^2 = \frac{\sum_i (k_i - \langle k \rangle^2)}{K}, \qquad [5.4]$$

where k_i is the pixel intensity collected for the image i ($0 \leq i \leq K$). Now, let ε be the molecular brightness of the fluorescent particle under observation. ε is defined as the number of photons emitted per second per particle when the particle is at the

center of the illumination volume (183). Thus, ε reflects the aggregation state of emitting particles.

If n is the average number of particles in the illumination volume, the average intensity is given by:

$$\langle k \rangle = S\varepsilon n + k_0, \quad [5.5]$$

where k_0 is the intensity offset and S is the conversion factor between one photon detected and the number of digital levels (DLs) produced by the detector electronics. For a photon-counting detector, S=1 and k_0=0

The variance σ^2 is composed by two contributions (183), according to:

$$\sigma^2 = \sigma_n^2 + \sigma_d^2. \quad [5.6]$$

Here, σ_n^2 is the variance of fluctuations due to changes in the number of molecules (and/or brightness flickering). The dependence of σ_n^2 from molecular number and brightness is easily understood by considering two pixels characterized by the same average intensity $\langle k \rangle$ but different values of n and ε: the variance will be higher at the pixel were few bright particles are moving compared to the other pixel at which many dim particles are diffusing (Fig. 5.6). Fluctuation theory based on Poissonian statistics (183) predicts that σ_n^2 is given by:

$$\sigma_n^2 = S^2 \varepsilon^2 n. \quad [5.7]$$

σ_d^2 is the variance attributable to the count statistics or shot noise of the detector, which is expressed by (183):

$$\sigma_d^2 = S^2 \varepsilon n + \sigma_0^2. \quad [5.8]$$

Here, σ_0^2 is the read-out noise of the detector (i.e. the intensity variance measured when zero fluorescence is collected). For a photon-counting detector, $\sigma_0^2 = 0$.

Next, the *N* and *B* parameters are defined following the treatment of *Digman et al.* (183). *B* is the apparent brightness of the fluorescent species and it is obtained for each pixel as the reciprocal of the ratio between the average fluorescence intensity and its associated variance, that is:

$$B = \frac{\sigma^2 - \sigma_0^2}{\langle k \rangle - k_0}. \qquad [5.9]$$

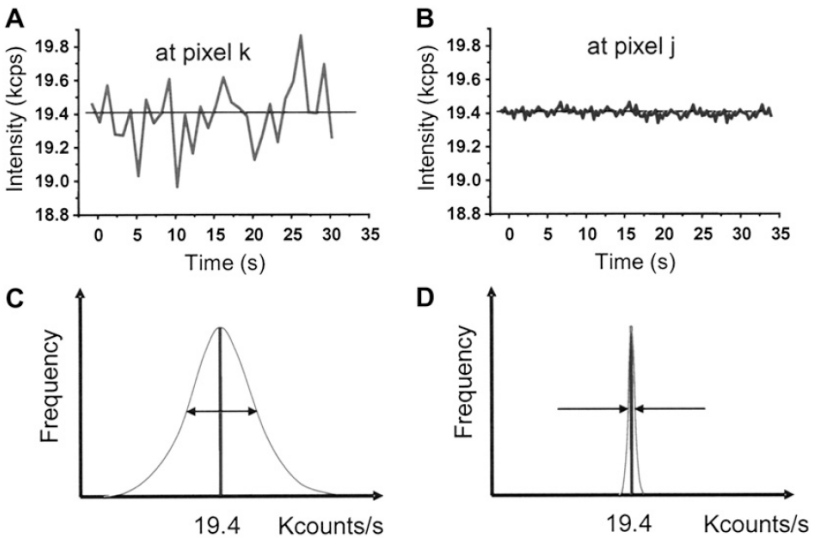

Figure 5.6. Schematic description of intensity and variance of a fluorescence signal over time. At pixels k (A) and j (B) the average intensity is the same but the standard deviation is much larger at pixel k than at pixel j. This is due to few bright particles fluctuating at pixel k while at pixel j there are a large number of dim particles. Panels C and D show schematically the histogram of counts corresponding to the situation in panels A and B, respectively. (Adapted from (183))

By using Eq. 5.5-5.9, *B* can be expressed as function of the molecular brightness:

$$B = S(\varepsilon + 1). \qquad [5.10]$$

B is particularly useful to identify the parts of the image that contain immobile fluorescent species. Indeed, for each pixel that contains only immobile particles, $\sigma^2 - \sigma_0^2 = \sigma_d^2 = \langle k \rangle - k_0$ and *B*=1. Conversely, pixels that contain mobile particles show *B>1*. The oligomerization degree *M* of a mobile multimeric fluorescent species can be easily calculated from the *B* value and that of the monomeric species (B_{mon}) by using eq. 5.10 and recalling the definition of average brightness (184):

$$M = \frac{B-1}{B_{mon}-1}. \qquad [5.11]$$

For a multimeric protein labeled with a FP reporter, B_{mon} is usually determined by looking at a reference monomeric FP chimera in the same experimental conditions (laser power and integration time in each pixel) adopted to image the target protein. For pixels containing a mixture of mobile and immobile components the value of *B* will be intermediate between 1 and that of the mobile fraction:

$$B = f_{mob} B_{mob} + (1 + f_{mob}), \qquad [5.12]$$

where B_{mob} is the apparent brightness of the mobile fraction and f_{mob} is its fluorescence intensity ratio, i.e.:

$$\frac{F_{mob}}{F_{mob} + F_{immob}}, \qquad [5.13]$$

N is defined as the ratio between the average intensity and *B*, and it represents the apparent number of emitting particles. It is easy to demonstrate that *N* depends only on ε and *n* according to:

$$N = \frac{\left(\langle k \rangle - k_0\right)^2}{\sigma^2 - \sigma_0^2} = \frac{\varepsilon}{\varepsilon + 1} n. \qquad [5.14]$$

N&B analysis involves mapping each pixel of the image stack in a plot of *B vs. N* from which the presence of immobile fraction and the oligomerization degree of the species under observation can be determined after a suitable calibration. In a meaningful N&B measurement, the pixel dwell time should always be small enough to ensure the recording of fluorescence fluctuations (183). On the other hand, the

frame time must be larger than the characteristic diffusion time to ensure that pixel occupation is governed by Poissonian statistics and Eq. 5.7 holds (183).

Since the error in the determination of the average and the variance decreases as the square-root of the number of independent measurements, the accuracy of N&B analysis increases as more frames are collected. Typically 10-20 frames are necessary to determine the brightness and number of particles and to be capable of showing the location of molecular aggregates. Spurious phenomena such as photobleaching or cell motion, which would increase the recorded variance, can be removed by suitable algorithms based on high-pass filters (183). Nonetheless, this procedure works only if the intensity changes due to cell movement or photobleaching are slower than particle fluctuations.

5.2.2 N&B analysis for quantitative investigation of oligomerization status of TRPV1 before and after activation

In section 5.1 we demonstrated that TRPV1 oligomerizes in both basal and agonist-activated states. Accordingly, N&B was applied to characterize further the oligomerization degree of TRPV1 on the cell membrane. N&B experiments were carried out in the confocal apparatus by collecting 100 sequential images. Pixel dwell time and frame time were set to 20 μs and 1.6 s, respectively. We should note that only the fast-moving TRPV1 subpools could be fully observed as mobile fraction under the adopted frame-time. The slow-moving TRPV1 fraction largely behaved as "immobile fraction" in the experimental conditions of the N&B experiments (characteristic diffusion time τ=370±189 s *vs.* frame time of 1.6 s), yielding B=1. A frame time matching the mobility of the slow-moving subpool was not accessible on account of by significant cell movement and extensive photobleaching during the measurements.

In order to relate the molecular brightness to the oligomerization degree, we first observed a monomeric FP benchmark that diffuses within the membrane. The choice fell on the fusion construct farnesyl-EGFP (EGFP-F), on account of its membrane arrangement similar to TRPV1-FP (185). In fact, EGFP-F intrudes the farnesyl lipid tail into the membrane bilayer and exposes the FP reporter on the cytoplasmic side. As expected, N&B revealed a homogeneous distribution of monomeric farnesyl-EGFP on the membrane (Fig. 5.7*A-B*). Upon excitation at 488 nm, the analysis afforded B = 1.13 ± 0.03 counts/molecule (number of cells = 8), corresponding to an average ε = 0.13 ± 0.03 counts/molecule (Fig. 5.7*C*). Under the

same excitation/emission conditions we found out that monomeric EGFP and YFP were characterized by the same brightness (Fig. 5.8). This can be easily explained by considering that YFP is brighter than EGFP when both proteins are excited at their absorption maxima (YFP: 525 nm, EGFP: 488 nm, see Fig. 3.3, § 3.1.3), but this difference becomes negligible when 488 nm excitation is adopted, because of the lower absorption of YFP at this wavelength. Thus, farnesyl-EGFP represented a useful benchmark of TRPV1-YFP, too.

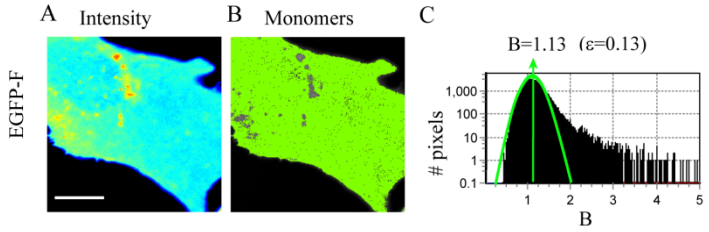

Fig. 5.7. N&B analysis of farnesyl-EGFP. (A) Confocal fluorescence image of a CHO cell transiently transfected with farnesyl-EGFP (EGFP-F) (scale bar: 10μm). Dwell time is set to 20 μs/pixel. (B) For the same cell shown in (A), selection of the pixels with apparent brightness corresponding to monomers (*B*=1.13 cpm) (ε=0.13 cpm=molecular brightness): monomers are distributed uniformly throughout the cell. (*C*) Brightness histogram: a Gaussian distribution centered at *B*=1.13 cpm identifies the monomer; only a few pixels are outside the distribution of the monomeric brightness.

N&B measurements on TRPV1-YFP yielded $B = 1.26 \pm 0.10$ [# 10cells] (Fig. 5.9A-C), although a significant number of pixels localized near $B = 1$. $B = 1.26$ corresponds to $\varepsilon = 0.26 \pm 0.02$ counts/molecule, a value which is twice as that observed for the monomeric benchmark.

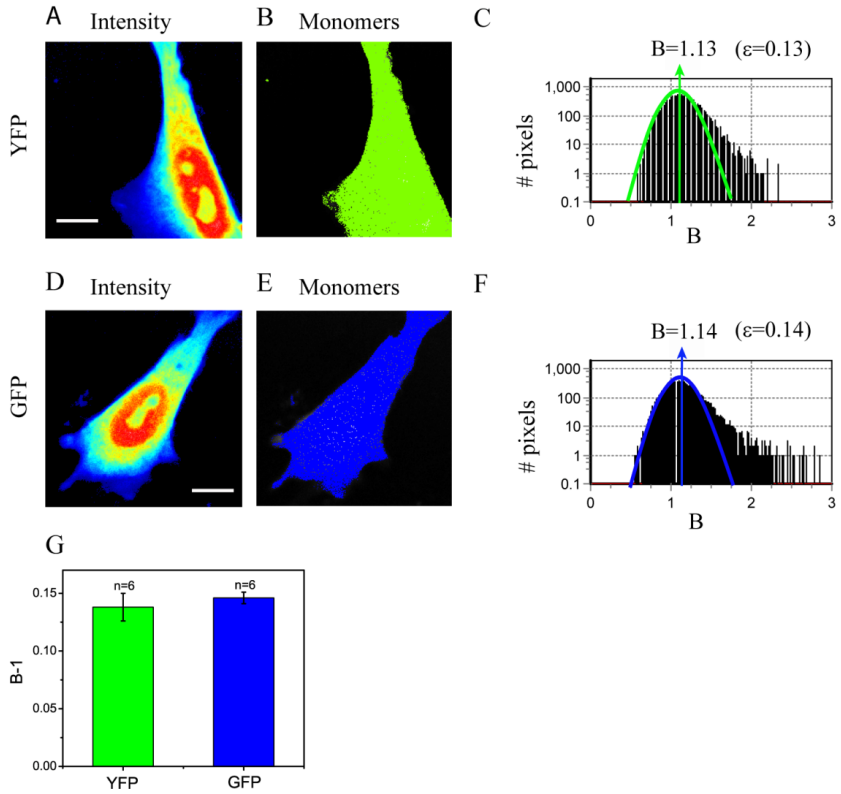

Fig. 5.8. Determination of the molecular brightness of YFP and GFP by N&B analysis. (A) Confocal fluorescence image of a CHO-K1 cell transiently transfected with YFP (scale bar: 10μm). Dwell time is set to 12.5 μs/pixel;. (B) For the same cell shown in (A), selection of pixels whose brightness corresponds to a YFP monomer, *B*=1.13 cpm. Notably, monomers are distributed uniformly throughout the cell. (C) Brightness histogram. A Gaussian distribution centered at *B*=1.13 cpm identifies the monomeric protein. Only a few pixels are outside the distribution of the monomeric brightness. (D-F) N&B analysis is performed on a cell transiently transfected with GFP (scale bar: 10μm) and imaged with the same experimental settings described above. The analysis reveals a homogeneous distribution of the monomeric form of GFP throughout the cell, with an average brightness of 1.14 cpm. (G) Cumulative results. In our N&B setup the ratio of molecular brightness (ε=*B*-1) between YFP and GFP is approximately 1. Thus EGFP-F and TRPV1-YFP can be directly compared in terms of oligomerization state as obtained from N&B analysis.

N&B analysis was also performed upon agonist (RTX) stimulation. With respect to basal state, both the "immobile" fraction with *B*=1 (blue) and the region with *B*

=1.52 (red), corresponding to tetrameric receptor arrangement, became more populated in the *B*/intensity map (Fig. 5.9D-F).

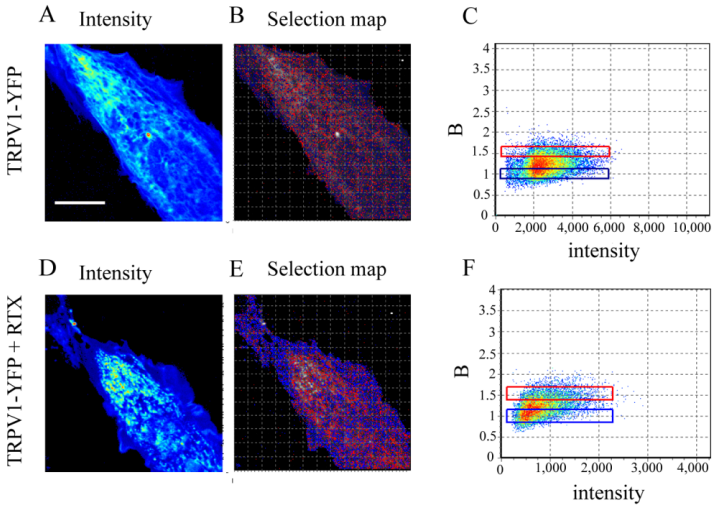

Fig 5.9. N&B analysis of TRPV1 oligomerization state. (A) Confocal fluorescence image of a CHO-K1 cell transiently transfected with TRPV1-YFP at basal state (scale bar: 10μm). (B) Pixels of corresponding to *B*=1 ("slow" diffusing component that behaves as immobile fraction in the frame time adopted for N&B analysis, see text) and *B*=1.52 (tetramers) were colored in blue and red, respectively. (C) B *vs.* intensity plot reveals that most pixels have average apparent brightness of 1.26 cpm (ε=0.26 cpm), corresponding to dimers. The blue and red rectangles enclose pixels corresponding to *B*=1 and *B*=1.52, respectively. (D) Confocal fluorescence image of the same cell of (A) after stimulation with RTX. (E) Similarly to (B), pixels of corresponding to *B*=1 and *B*=1.52 (tetramers) were colored in blue and red, respectively. (F) Brightness-*vs.* intensity plot shows a significant increase of *B*=1 pixels (blue rectangle) relevant to the slow TRPV1 component.

These findings were fully accounted for by the population increase of slow-moving, functional receptor upon agonist stimulation that was already observed by tICS (§ 4.2.2). Although the slow-moving TRPV1 subpool was observed prevalently as immobile fraction (*B*=1), some molecules diffused in times matching the acquisition frame time, and were visualized as tetramers with *B* = 1.52 consistently with the tetrameric arrangement reported in literature for functional TRPV1.

Concerning the fast-moving TRPV1 subpool, two possible oligomerization states could be envisaged by N&B data. We might assign *B*=1.26 to dimers only, under the

assumption that pixels characterized by this *B* value contains only the fast-moving TRPV1. On the other hand, if pixels contain both populations, we might consider *B*=1.26 as the intensity-weighted average between *B*=1 (blue rectangle in Fig. 5.9C) and *B*=1.52 (red rectangle in Fig. 5.9C). As discussed before, *B*=1 should be assigned to the slow component since its diffusion can not be visualized as fluctuation in our frame time. The value *B*=1.52 would imply a tetrameric oligomerization for the fast diffusing component. We can not exclude the presence of intermediate cases (i.e. mixtures of dimers and tetramers), under the reasonable assumption of receptor aggregation/disaggregation processes at equilibrium.

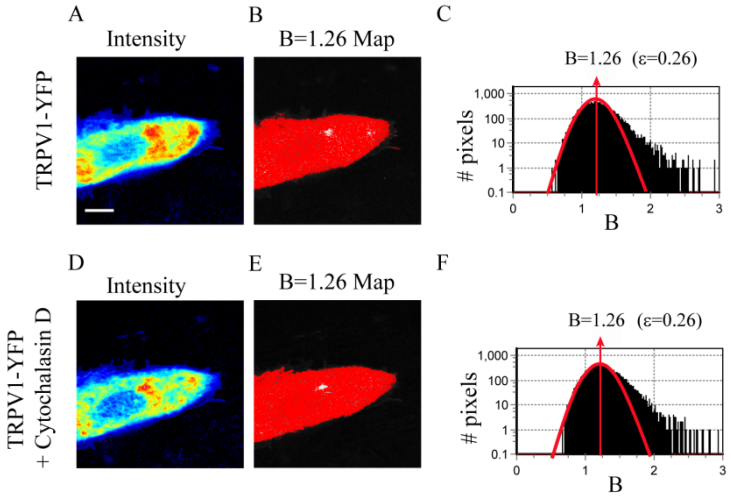

Fig. 5.10. N&B analyses of TRPV1-YFP oligomerization state after cytochalasin D. (A) Confocal fluorescence image of a CHO cell transiently expressing TRPV1-YFP at basal state (scale bar: 10µm). (B) N&B analysis reveals a homogeneous distribution of *B*=1.26 pixels throughout the cell of panel (A). (C) Brightness histogram where a Gaussian distribution centered at 1.26 cpm is denoted by a red line. Notably, only a few pixels are outside the distribution. (D) Confocal fluorescence image of the same CHO cell of (A) after stimulation with Cytochalasin D. (F) Same as in panel (C).

Finally, we measured N&B in presence of nocodazole and cytochalasin to test the effect of cytoskeletal disruption on TRPV1 oligomerization. Cytochalasin administration led to *B*=1.26 identical to resting cells (Fig 5.10), in full consistency with the absence of interactions between TRPV1 and the actin cytoskeleton. Unfortunately, nocodazole treatment led to extensive bleaching of the fluorescence, thus preventing N&B analysis. This finding is in agreement with FAIM and tICS

data indicating that microtubule disassembly leads to the formation of large and immobile TRPV1 oligomers prone to photobleaching (Fig. 5.11).

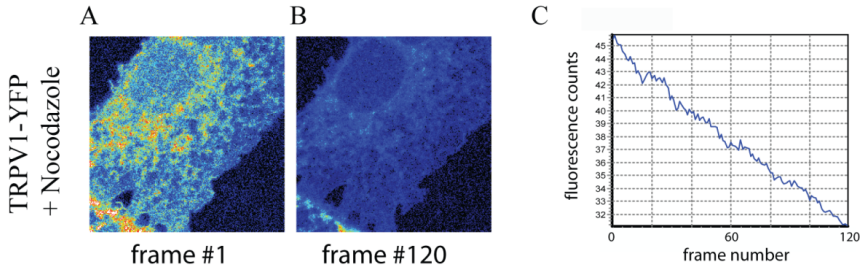

Fig.5.11 Fluorescence intensity analysis of cells expressing TRPV1-YFP after nocodazole treatment. First (A) and last (B) intensity image of a time stack relevant to TRPV1-YFP after after nocodazole treatment. (C) The intensity *vs.* time plot shows a strong photobleaching occurring during the measurement.

5.3 Concluding remarks

In conclusion, by fluorescence anisotropy imaging (FAIM) associated to homo-FRET we demonstrated that TRPV1 is aggregated in basal condition and its oligomerization degree increases significantly upon microtubule disassembly. The extensive aggregation might explain the loss of TRPV1 functionality upon microtubule disassembly observed at Chapter 3. On the other hand, actin depolymerization did not produce changes in the aggregation state of TRPV1, highlighting the specific role of microtubule in stabilizing the receptor in its functional state. The tetrameric structure of the functional receptor was compatible with our Number and Brightness (N&B) results. N&B also witnessed the concentration increase of the functional, slow-moving TRPV1 subpool upon agonist stimulation. Two limiting oligomerization states are compatible with N&B data for the fast-moving TRPV1 subpool: 1) dimeric, under the assumption of spatial segregation with respect to the slow-moving subpool, or 2) tetrameric, otherwise. Intermediate cases, i.e. dimers and tetramers interconverting at equilibrium, are nonetheless possible.

5.4 Experimental procedures

5.4.1 Plasmids, cell culture and trasfections

For this set of experiments we used the plasmid TRPV1-YFP (described in §3.4.1). EGFP and EYFP plasmids (from Clontech) were used to calibrate the anisotropy value of monomer in FAIM and the brightness ratio in N&B analysis. The plasmid encoding for farnesyl-EGFP is a kind gift of Dr. Tarik F. Haydar, Laboratory of Neural Development and Intellectual Disorders, Boston University. CHO-K1 cells from ATCC (CCL-61 ATCC) were cultured and transfected as described in §3.4.2

5.4.2 FAIM: Anisotropy imaging.

Measurements were carried out by a Leica TCS SP2 inverted confocal microscope (Leica Microsystems AG, Wetzlar, Germany). 40x (NA 1.25) planApo oil immersion objectives were used while setting the confocal pinhole at 1 Airy unit. For anisotropy imaging on TRPV1-YFP, samples were excited at 488 nm and fluorescence was collected in the 520-600 nm range at parallel and perpendicular polarization with respect to the exciting beam by using the internal polarizer of the microscope. Anisotropy maps were obtained by a custom-made plugin running under ImageJ. Images were smoothed with a Gaussian filter with a standard deviation of 1 pixel. When processing data acquired from cells, the images were corrected by subtracting the average background intensity measured from a small region in the image where no cells were visible.

5.4.3 Number and Brightness (N&B) analysis.

We set the Olympus FluoView 1000 to the pseudo-photon-counting data acquisition mode. In this mode, the parameters needed for N&B analysis are the detector offset, the factor S that converts photon counts to digital levels, and the readout variance σ_0^2. For the present analysis these parameters were estimated according to (184). We obtained S=3.5, σ_0^2=0, and offset=0. 256x256 images at 8 bits were collected with a pixel dwell time of 20μs. A time series of 100 frames with no programmed delay between images was used to reduce statistical error. Low laser power was used to avoid photobleaching. The N&B analysis was performed using the SimFCS software (**www.lfd.uci.edu**). In order to calibrate laser power and scanning conditions required for the measurement of a monomeric protein diffusing

within membranes, we measured the brightness of CHO-K1 cells transiently expressing the nonaggregating farnesyl-EGFP adduct (EGFP-F). These conditions were then used for the TRPV1-YFP experiments. We separately measured the difference in apparent brightness (B) between EGFP and YFP by using CHO-K1 cells transiently expressing the two untagged variants (Fig. S2): we found a YFP/EGFP brightness ratio very close to 1.

Chapter

6

Spatio-Temporal Image Correlation Spectroscopy: revealing connections between TRPV1 function and receptor organization on membrane

In Chapter 3 we showed by FRET that TRPV1 interacts with caveolin-1 and tubulin dimers belonging to integer microtubules as a way to de-sensitize and stabilize the activated receptor, respectively. In Chapter 4 we demonstrated by temporal Image Correlation Spectroscopy (tICS) that membrane TRPV1 entails at least two components. The slowest component corresponds to the functional receptor and, in part or totally, was found to interact with intact microtubules. We can not exclude, however, that one or both components could be subdivided in further subpools characterized by different types of diffusion processes. The comprehensive picture of TRPV1 diffusion/binding processes and its spatial organization on the membrane can be clarified only by image correlation protocols that consider both the spatial and temporal coordinates. Accordingly, we availed ourselves of a new fluorescence fluctuation approach named *i*MSD analysis. *i*MSD is based on Spatio-Temporal Correlation Spectroscopy (STICS) and its

photophysical background will be presented in section 6.1. In Section 6.2 we shall demonstrate that *i*MSD can be proficiently combined with FRET to highlight the relationship between diffusion and spatial organization of the interacting/non-interacting receptor subpools. In particular, we shall demonstrate that TRPV1 complexes with caveolin-1 and tubulin are spatially-decoupled and follow distinct diffusion processes. A further non-interacting TRPV1 subpool will be assigned to an immature form of the receptor that plays the role of membrane reservoir.

6.1 *i*MSD approach to spatio-temporal image correlation spectroscopy

Spatio-Temporal Correlation Spectroscopy (STICS) is a fluorescence fluctuation technique that identifies the kind of spatial movements of fluorescently labeled adhesion macromolecules within the plasma membrane of living cells (168) (161). In contrast with tICS, STICS relies on a complete calculation of both the temporal and all-spatial correlation lags for intensity fluctuations from an image stack. Recently a group in our lab has proposed a modified STICS approach that is suitable for determining diffusion laws of biomolecules in live cells with high temporal and spatial resolution and no need for the preliminary assumption of a specific interpretative model. The novel STICS approach was named *i*MSD analysis (186). Recent data demonstrated that *i*MSD is particularly suitable to study protein membrane dynamics on wide spatial and temporal scales, thus fully complementing high-speed single-molecule techniques in the investigation of membrane dynamics at the nanoscale (187).

6.1.1 Photophysical background of *i*MSD

In Appendix A we showed that the image spatiotemporal autocorrelation function $G(\xi,\chi,\tau)$ is calculated from a temporal stack of images according to:

$$G(\xi,\chi,\tau) = \frac{\langle I(x,y,t)\cdot I(x+\xi,y+\chi,t+\tau)\rangle}{\langle I(x,y,t)\rangle\langle I(x,y,t+\tau)\rangle} - 1, \qquad [6.1]$$

where *I(x,y,t)* stands for the fluorescence intensity of the pixel located in the (*x,y*) position of the image at time *t*, and ξ, χ, τ represent variable spatial and temporal increments. Given the usual z-axial symmetry of the Gaussian illumination beam, it is useful to recast the ξ and χ spatial-lags into a single parameter (Appendix A):

$$\rho^2 = \xi^2 + \chi^2. \qquad [6.2]$$

The spatiotemporal correlation function in a 2D space (membrane bilayer) is reported as Eq. A.11 of Appendix A. This equation can be rewritten in an equivalent (but more informative) form:

$$G_{2D}(\rho,\tau) = G(0,0)\cdot g_C(\rho,\tau)\cdot g_\Phi(\tau), \qquad [6.3]$$

where g_C and g_* are the autocorrelation components due to molecular motion and brightness flickering, respectively. The g_C component is expressed by:

$$g_C(\rho,\tau) = \frac{1}{\sigma_r^2(\tau)}\cdot \exp\left(-\frac{\rho^2}{\sigma_r^2(\tau)}\right), \qquad [6.4]$$

with

$$\sigma_r^2(\tau) = 4D\tau^\alpha + \sigma_0^2. \qquad [6.5]$$

D is the diffusion coefficient, α takes into account the nature of the diffusive process (α =1: isotropic diffusion, α <1 confined diffusion, α >1 guided diffusion), and σ_0 is a parameter related to the size of the diffusing moiety (186). Indeed, it can be demonstrated that the diameter d of a diffusing particle can be approximated by:

$$d = \sqrt{\sigma_0^2 - \sigma_{xy}^2}, \qquad [6.6]$$

where σ_{xy} is the spatial resolution of the microscope on the focal plane (§ 2.1.1). σ_r^2 is denoted as *i*MSD, since it is conceptually and mathematically analogous to the mean square displacement (MSD) of single particle tracking analysis (186).
The g_* component is expressed by:

$$g_{\Phi}(\rho,\tau) = \exp\left(-\frac{\tau}{\tau_{\Phi}}\right), \qquad [6.7]$$

where τ_{Φ} is the characteristic time of brightness flickering. Several photophysical and photochemical processes result in brightness flickering. The most relevant ones are quenching and FRET upon biomolecular binding. When binding is involved, τ_{Φ} corresponds the characteristic time of reversible association/dissociation of the complex, τ_a.

Two limit cases are of particular relevance for *i*MSD analysis: 1) constant brightness and 2) diffusion time much slower than the characteristic time of brightness flickering. In case (1), only molecular diffusion contributes to the recorded autocorrelation function, that is:

$$G_{2D}(\rho,\tau) = G(0,0)\cdot g_C(\rho,\tau). \qquad [6.8]$$

Experimental data can be fitted to Eqs. 6.4-6.5 and 6.8 to recover diffusion parameters. An alternative way to analyze molecular diffusion is provided by inspecting the time derivative of $G_{2D}(\rho,\tau)$:

$$\frac{\partial G_{2D}(\rho,\tau)}{\partial \tau} = G(0,0)\frac{\exp\left(-\frac{\rho^2}{\sigma_r^2(\tau)}\right)}{\sigma_r^4(\tau)}\cdot\left(\frac{\rho^2}{\sigma_r^2(\tau)}-1\right)\cdot\frac{\partial\sigma_r^2(\tau)}{\partial\tau}. \qquad [6.9]$$

At time $\tau_{\max}^{\alpha}$ when:

$$\left(\frac{\rho^2}{\sigma_r^2\left(\tau_{\max}^{\alpha}\right)}-1\right) = 0, \qquad [6.10]$$

the time-derivative in Eq. 6.11 goes to zero. It is easy to demonstrate that $\tau_{\max}^{\alpha}$ corresponds to a maximum of $G_{2D}(\rho,\tau)$ *vs.* τ at constant ρ.

By inserting (6.5) into (6.10), for a given $\rho^2 > \sigma_0^2$, we have:

$$\rho^2 = 4D\tau_{\max}^{\alpha} + \sigma_0^2. \qquad [6.11]$$

We can recover the relevant diffusion parameters directly from the plot of ρ^2 *vs.* $\tau_{\max}^{\alpha}$ by using Eq. 6.11. For isotropic diffusion ($\alpha = 1$), we have a linear dependence of ρ^2 from $\tau_{\max}^{\alpha}$, whereas super- and sub-diffusion processes ($\alpha \neq 1$) are characterized by non-linear plots.

In case (2), i.e. when the particle diffusion time is much slower with respect to its brightness flickering, we can assume $D \approx 0$. Thus, Eq. 6.3 becomes:

$$G_{2D}(\rho,\tau) = G(0,0) \cdot \frac{1}{\sigma_0^2} \cdot \exp\left(-\frac{\rho^2}{\sigma_0^2}\right) \exp\left(-\frac{\tau}{\tau_\Phi}\right). \qquad [6.12]$$

In this condition, Eq. 6.12 indicates that, $G_{2D}(\rho,\tau)$ is expressed by a Gaussian function of constant width and time-decreasing amplitude.

6.1.2 *i*MSD to study mixed binding and diffusion

An analytical form of $G_{2D}(\rho,\tau)$ is not available for a heterogeneous biological context containing different types of diffusing particles. An empirical approach considers a total autocorrelation function given by a sum of individual components, such as:

$$G_{2D}(\rho,\tau) = \sum_i A_i \cdot g_i(\rho,\tau), \qquad [6.13]$$

where A_i is the correlation amplitude of the ith component at zero space and time, and $g_i(\rho,\tau)$ represents its relevant autocorrelation function. The presence of a known binding equilibrium entailing a single component, however, helps to simplify the analysis. Indeed, in such a case we can use a "FRET filter", as already demonstrated for tICS (§ 4.3). The FRET filter is obtained by labeling the target molecule and its binding partner by a suitable FRET couple. Notably, the sensitized FRET signal associated with a molecular complex, or the concomitant donor quenching, depend directly on the reversible formation/dissociation of the complex itself. This leads to brightness flickering, which is in turn reflected into the general autocorrelation function by means of the characteristic binding time τ_B. Accordingly, it is useful to define a "FRET" correlation function that accounts for both diffusion and binding time of the complex as:

$$G_{FRET}(\rho,\tau) = G(0,0)\frac{1}{\sigma_r^2(\tau)}\cdot\exp\left(-\frac{\rho^2}{\sigma_r^2(\tau)}\right)\exp\left(-\frac{\tau}{\tau_B}\right). \quad [6.14]$$

*i*MSD-FRET approach is based on Eq. 6.14. In Section 6.2 we shall apply *i*MSD-FRET to recover the intrinsic diffusion properties of the TRPV1-caveolin-1 (TRPV1-C) and TRPV1-tubulin (TRPV1-T) complexes.

6.2 Spatio-temporal investigation of TRPV1 membrane mobility by *i*MSD

6.2.1 Spatiotemporal organization of TRPV1-caveolin (TRPV1-C) complex

The diffusion characteristics of the TRPV1-caveolin-1 complex (TRPV1-C) were analyzed by FRET-*i*MSD in TIRF modality. Experimentally, CHO cells were imaged every 10 ms up to 60s. A time-dependent spatial correlation function $G_{FRET}(\rho,\tau)$ was calculated from each image collected in the FRET acceptor channel of RFP emission. $G_{FRET}(\rho,\tau)$ was fitted to Eq. 6.5-6.14 to take into account both diffusion and FRET flickering for TRPV1-C. Notably, the profile of *i*MSD (Eq. 6.5) due to TRPV1-C was nearly time-independent after a fast transient of small amplitude (Fig. 6.1A). This finding demonstrates that TRPV1 and caveolin-1 do not co-diffuse significantly as a complex. Nonetheless, the autocorrelation amplitude was shown to decrease over time, indicating the presence of brightness flickering due to FRET (Table 6.1). This flickering was assigned to the reversible binding of TRPV1-C. In order to recover the characteristic binding time of the complex, we assumed $D \approx 0$ and we fitted the correlation data at $\rho = 0$ to Eq. 6.12. We found out τ_b=16.4±4.0 s (Fig. 6.4B).

Finally, the analysis of *i*MSD intercept with Y-axis highlighted that TRPV1-C has an apparent diameter of 360±40 nm, consistent with the size of caveolar regions (188) (Table 6.1).

Table 6.1. Parameters derived from *i*MSD analysis.
The rows indicate the different dynamic populations of TRPV1. For each population we report three conditions: basal, nocodazole-treated (+NDZ), and sphingomyelinase-treated (+SMase). Dynamic parameters are reported in columns: *D*=diffusion coefficient, α = *anomalous diffusion* exponent, δ = diameter of diffusing species, τ_B = characteristic binding time, and A = fractional correlation amplitude. The values are expressed as Mean±Standard Error.

TRPV1 pool	*D* ($\mu m^2/s$)	α	d (nm)	τ_b (s)	A (%)	
TRPV1-C	~ 0	-	360±40	16.4±4.0	68±21	**Basal**
	*	*	*	*	69±14	**+NDZ**
	*	*	*	2.9±2.1	88±08	**+SMase**
TRPV1-T	$(9.0\pm2.6)\cdot10^{-3}$	1.5±0.3	860±300	«10 ms or »60 s	19±16	**Basal**
	-	-	-	-	0	**+NDZ**
	-	-	-	-	0	**+SMase**
TRPV1-I	0.22±0.02	1	-	-	13±09	**Basal**
	0.99±0.18	*	-	-	31	**+NDZ**
	0.10±0.04	*	-	-	12±07	**+SMase**

* Values keeping equal at basal condition (obtained by STICS-FRET analysis) during the fitting
- Not Determined

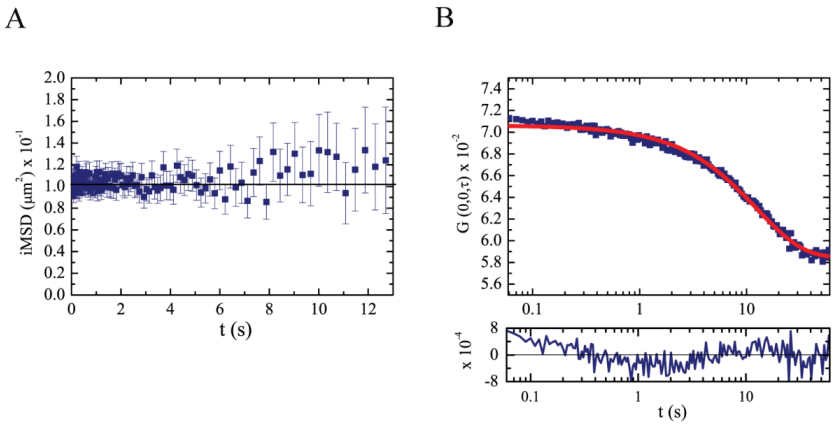

Figure 6.1. *i*MSD-FRET analysis of TRPV1-caveolin-1 complex (TRPV1-C). (A) *i*MSD vs. time plot of FRET signal for the caveolin-1-EGFP/TRPV1-TagRFP pair in physiological condition. The constant *i*MSD clearly demonstrates that the complex is not diffusing in space, i.e. it is trapped within caveolin-enriched structures on cellular membrane. (B), Temporal evolution of the binding component: plot of G(0,0,τ) vs. time shows the decrease of correlation function in time.

6.2.2 Spatiotemporal organization of TRPV1-microtubule (TRPV1-T) complex

The diffusion characteristics of the TRPV1-α–tubulin complex (TRPV1-T) were analyzed by FRET-*i*MSD in TIRF modality by using TRPV1-EGFP and TagRFP-αT. Fitting of $G_{FRET}(\rho,\tau)$ to Eq. 6.5 and 6.14 indicated the absence of FRET flickering and the presence of the sole diffusing component, thus suggesting that the complex binding time is much longer than the overall acquisition time (60 s). Remarkably, *i*MSD of TRPV1-T was found to be associated with a time dipendent hyperbolic growth (Fig. 6.2). This "super-diffusive" dynamic behavior is attributable to guided/active mobility (189). In this process we found out $D=(9.0\pm2.6)\cdot10^{-3}$ $\mu m^2/s$ and $\alpha=1.5\pm0.3$ (Table 6.1). Interestingly, the analysis gave $\sigma_0 >> \sigma_{xy}$: Eq. 6.6 yielded ~800 nm as the dimension of super-diffusive TRPV1-T. This suggests that the interaction between TRPV1 and tubulin occurs over large sub-micron domains of the cell membrane. Consistently, a highly patterned signal, composed by several spots with 500-1000 nm size, was visible also in the static FRET image (§ 3.2.2 Fig 3.9).

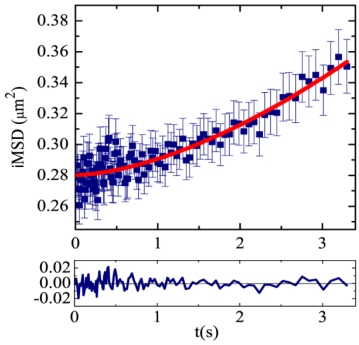

Figure 6.2. *i*MSD-FRET analysis of TRPV1-microtubules interaction (TRPV1-T). *i*MSD *vs*. time plot for FRET signal between TRPV1-EGFP and TagRFP-αT in physiological conditions. The fitting shows that TRPV1-T undergoes a super-diffusion process within the cellular membrane.

In Section 3.2.2 we demonstrated by FRET that a fraction of TRPV1 is bound to (at least) one microtubule chain. Literature data showed that the cytoplasmic tail of a single TRPV1 chain contains a binding stretch to the plus end of microtubules

(147). tICS results indicated that only the functional receptor interacts with, and it is stabilized by, microtubules. FRET-*i*MSD provided further biological insights on the TRPV1-microtubule interaction: TRPV1-T complexes are arranged supramolecularly over large membrane regions (500-1000 nm), and the diffusion of these rather large membrane islets is guided by microtubules.

6.2.3 Fast- and brownian-diffusing TRPV1 pool

The FRET and *i*MSD-FRET experiments highlighted the presence of the TRPV1 complexes with caveolin-1 (TRPV1-C) and microtubules (TRPV1-T). To check whether these two subpools constitute the only dynamic populations of the receptor, we carried out *i*MSD measurements on the sole receptor (Fig 6.3A).

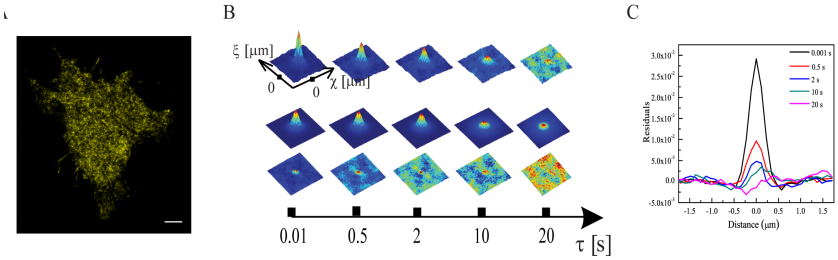

Figure 6.3. *i*MSD analysis of TRPV1-YFP diffusion assuming only two species that contribute to the observed decay of autocorrelation function. (A) TIRF microscopy image of a CHO cell expressing TRPV1-YFP. (B*)* The spatiotemporal autocorrelation function at different times is shown (upper section) together with with the corresponding Gaussian fit (middle section) and residues (lower section). Two dynamic components that account for binding and superdiffusion regimes are considered. Note the rather high residuals at short timescale <2 s. (C) Horizontal ($\xi = 0$) section of the residual plot of panel (B): the high residuals at short times are clearly visible.

The autocorrelation function of TRPV1-YFP was initially fitted to a sum of two fixed components (Fig. 6.3B), one accounting for a sub-diffusive/binding regime (TRPV1-C) and the other for a super-diffusive regime with very long binding time (TRPV1-T). Inspection of the residuals highlighted that TRPV1-C and TRPV1-T are not enough to account for the experimental autocorrelation at times <2s (Fig.6.3C). Additionally the presence of a fast diffusing component was investigated by the "derivative" approach expressed by Eq. 6.9-6.10. $G_{2D}(\rho,\tau)$ *vs.* τ was plotted for 500 nm < ρ < 1 μm (Fig. 6.4A), thus filtering out the "immobile" binding component TRPV1-C, visible only for $\rho \leq \sigma_{xy}$ (§ 6.13). Then, the time at which the

autocorrelation showed a maximum (τ_{max}) was computed for each ρ value. For short times (<2 s), the plot of ρ^2 *vs.* τ_{max} displayed a nearly linear behavior (Fig. 6.4B).

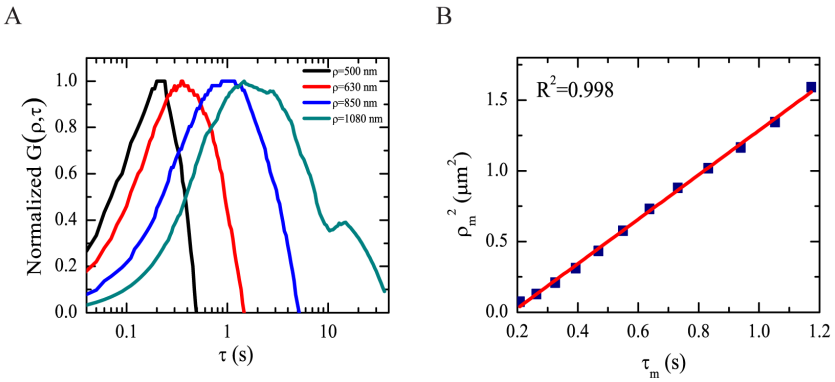

Figure 6.4. Disclosing of an isotropic TRPV1 component by *i*MSD analysis. (A) Representative average correlation functions of TRPV1 for distances between 500 nm e 1 um. The position of the maximum of the curves (ρ_m^2) shifts at longer times (τ_m) increasing the spatial lag.. (B) When ρ_m^2 is plotted *vs.* τ_m (<1.2 s), a linear trend (R^2=0.998) is clearly visible, indicating the presence of a Brownian-diffusing TRPV1 component.

We should note that in this temporal range the guided diffusion by microtubules was spatially negligible (*i*MSD < 0.03 mm^2/s) and TRPV1-T did not contribute to the observed *i*MSD. These date indicated the presence of a TRPV1 subpool diffusing isotropically with $D=(2.2\pm0.2)\cdot10^{-1}$ $\mu m^2/s$. We denoted this subpool as TRPV1-I.

Remarkably fitting the experimental $G_{2D}(\rho,\tau)$ to a sum of three components (Fig 6.5A), TRPV1-T, C and I always yielded very low residuals at any time, thus confirming the presence of the three subpools (Fig.6.5B). Table 6.1 reports the correlation amplitudes as fraction of the total correlation at $\rho = 0$ and $\tau = 0$. Correlation theory shows that the inverse of correlation amplitudes is related to a number of factors including the mole fraction of the relevant diffusing component. Accordingly we investigated the dependence of the inverse of A_T, A_C and A_I upon the total expression of the receptor, the latter being expressed by the overall fluorescence on the cell membrane. This analysis afforded a semi-quantitative

picture on how the three TRPV1 pools were populated at different total receptor concentration. Remarkably, A_C, A_T were almost independent from fluorescence intensity of TRPV1-YFP (i.e. from the expression level of the receptor) (Fig 6.6A and B), whereas A_I appeared linearly correlated with the TRPV1 concentration (Fig 6.6C).

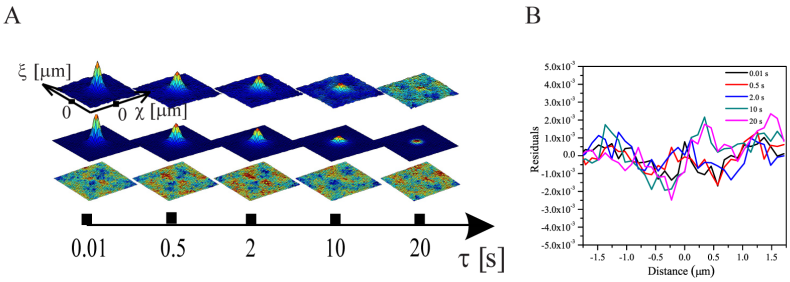

Figure 6.5 *i*MSD analysis of TRPV1-YFP diffusion assuming three species that contribute to the observed decay of autocorrelation function. (A) The spatiotemporal autocorrelation function at different times is shown (upper section) together with the corresponding Gaussian fit (middle section) and residues (lower section). For fitting, three dynamic components that account for binding, superdiffusion, and isotropic diffusion regimes are considered.. (B), Horizontal ($\xi = 0$) section of the residual plot as shown in panel (A): the low residuals at any time are clearly visible...

This finding strongly suggests that the membrane concentrations of TRPV1-C and TRPV1-T are strictly regulated and do not follow changes in the expression level of the receptor. This feature is in keeping with the strict control over the diffusion behavior of these TRPV1 complexes, confirming that they play a relevant biological role. On the other hand, the progressive growth of TRPV1-I concentration with increasing expression level, together with its free isotropic diffusion, advocates a reservoir role for this subpool, which likely represents an immature form of the receptor.

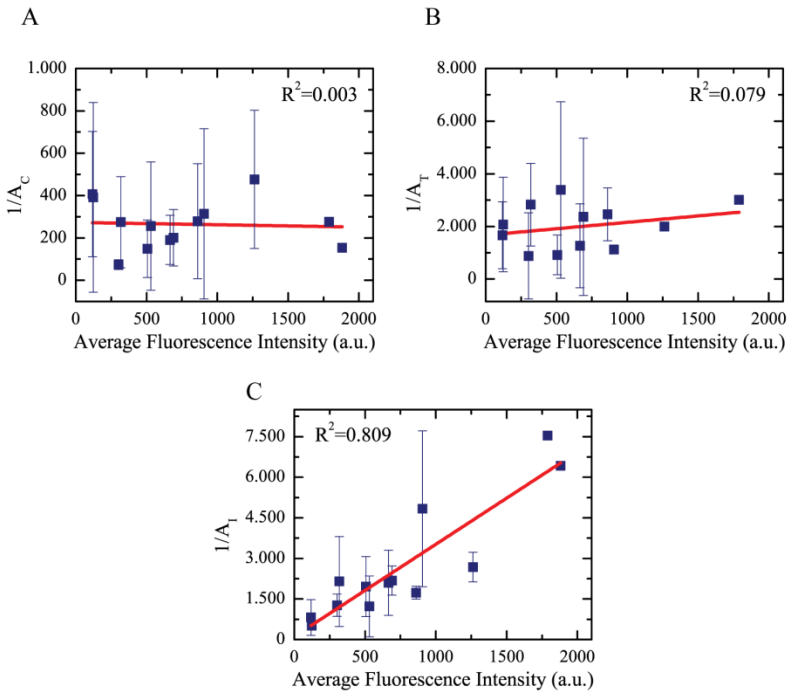

Figure 6.6. Dependence of the amounts of TRPV1 subpools upon cellular expression level of the whole receptor. TRPV1-C (A) and TRPV1-T (B) membrane populations are not affected by the receptor expression level, as witnessed by the low linear correlation coefficients. (C) Unlike the other two components TRPV1-I population is almost linearly related to receptor expression level.

6.2.4 Effect of microtubule disassembly or lipid-raft depletion on TRPV1 diffusion

In order to test the effect of microtubule disassembly or lipid-raft depletion on TRPV1 diffusion, we submitted cells to nocodazole and sphingomyelinase, respectively.

Nocodazole treatment had two effects: 1) TRPV1-T pools disappeared, and 2) $G_{2D}(\rho,\tau)$ could be fitted to a two components model entailing TRPV1-C and TRPV1-I (Fig 6.7A). Furthermore, in the absence of microtubules A_C did not change, whereas an increase in A_I was observed (Table 6.1). These findings support

the hypothesis of TRPV1-I as receptor reservoir. Notably, TRPV1-I was characterized by a larger diffusion coefficient as compared to the basal condition (Table 6.1).

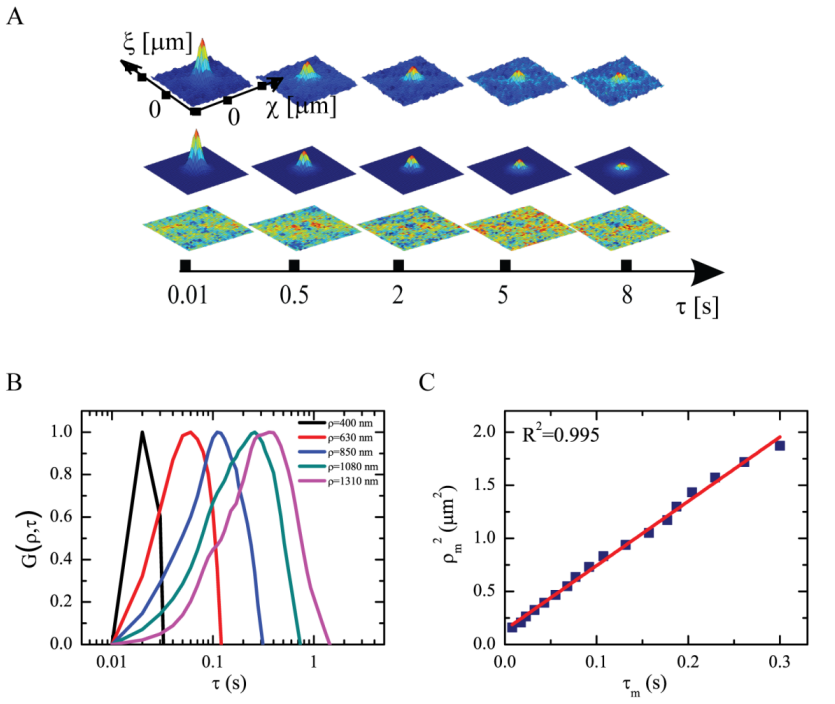

Figure 6.7. *i*MSD analysis of TRPV1-YFP diffusion in the presence of nocodazole. (A) The spatiotemporal autocorrelation function at different times is shown (upper section) together with the corresponding Gaussian fit (middle section) and residues (lower section). Two dynamic components that account for binding, and isotropic diffusion regimes are considered. The superdiffusive TRPV1-T was not considered for the absence of intact microtubules. The low residuals support our assumption. (B) Representative average correlation functions of TRPV1 for distances between 410 and 1310 nm e 1 um. The position of the maximum of the curves (ρ_m^2) shifts at longer times (τ_m) increasing the spatial lag. (C) When ρ_m^2 is plotted *vs.* τ_m (<0.4 s), a linear trend (R^2=0.995) is clearly visible, highlighting the isotropic diffusion of TRPV1-I (*D*=(0.99±0.18) $\mu m^2/s$).

Sphingomyelinase treatment hampered the formation of TRPV1-C, as witnessed by the significant 5-fold decrease of τ_b (Tab. 6.1). This result is consistent on the sphingomyelin-enriched raft nature of caveolae (190). Surprisingly, however,

sphingomyelinase treatment triggered the complete disappearance of TRPV1-T component. This result in turn dictates that the large membrane islets containing TRPV1-T must be stabilized by raft patches containing sphingomyelin. Inspection of fractional correlation amplitudes showed that the loss of TRPV1-T increased of TRPV1-C, with no concomitantly alteration of the TRPV1-I concentration (Table 6.1). The diffusion coefficient of TRPV1-I, however, was radically decreased. This result might be explained by considering a general systemic influence on membrane fluidity by sphingomyelin.

6.3 Concluding remarks

In conclusion, in this chapter we targeted the full comprehension of TRPV1 diffusion/interaction processes as well as its spatial organization on the membrane. This goal was pursued by the use of a novel image correlation approach, *i*MSD. *i*MSD includes both the spatial and temporal dimensions and it is suitable for determining diffusion laws of biomolecules in live cells. We demonstrated that *i*MSD can be proficiently combined with FRET to highlight the relationship between diffusion and spatial organization of the interacting/non-interacting receptor subpools. In particular, we showed that TRPV1 complexes with caveolin-1 (TRPV1-C) and tubulin (TRPV1-T) are spatially-decoupled and follow distinct diffusion processes. TRPV1-C is almost immobile on the membrane, being located in membrane regions with size comparable or smaller than the resolution of the imaging system (250-300 nm). Also TRPV1-C is characterized by a reversible association/dissociation process over a few seconds. TRPV1-T, instead, assemble over large membrane patches (up to 900-1000 nm). The membrane diffusion of the these patches is guided by microtubules. The TRPV1-T complex is stable for times longer than 60 s but microtubule depolymerization leads to the disassembly. On the other hand, depletion of sphingomyelin to hamper lipid-raft formation leads to a faster association/dissociation equilibrium of TRPV1-C and the disassembly of TRPV1-T. The latter result suggests that the large islets where TRPV1-T assembles are critically dependent on the stability of membrane rafts. TRPV1 comprises a third “immature” subpool, TRPV1-I, which moves isotropically within the membrane and plays the role of receptor reservoir. Differently from TRPV1-C and

TRPV1-T, whose membrane contents are strickly regulated to fulfill their biological roles, TRPV1-I concentration increases with receptor expression.

The presence of three receptor subpools is apparently in contrast with previous tICS results, which indicate the presence of two main autocorrelation components. We should note, however, that the reversible equilibrium of "immobile" TRPV1-C is detected by tICS as temporal dissipation of correlation. Thus, the "fast" component detected by tICS averages the fast isotropic diffusion of TRPV1-I and the reversible binding of TRPV1-C. Consistently, no interaction of the "fast" component with microtubules was highlighted by tICS-FRET ($ 4.3.2). Instead, the "slow" component detected by tICS and tICS-FRET fully identifies with TRPV1-T.

6.4 Experimental procedures

6.4.1 Cell Cultures, Constructs and Transfection.

CHO K1 cells were provided by American Type Culture Collection (CCL-61 ATCC) and grown in Dulbecco's modified Eagle medium F-12 nutrient mix (D-MEM/F-12, Invitrogen, Carlsbad, CA) supplemented with 10% fetal bovine serum, 100 U/ml penicillin, and 100 mg/ml streptomycin (Invitrogen). For live imaging, 12 $\times 10^4$ cells were plated 24 hours before transfection onto a 35-mm glass-bottom dish (WillCo-dish GWSt-3522). Transfections of all constructs were carried out using Lipofectamine reagent (Invitrogen) according to the manufacturer's instructions. In all experiments, cell were maintained at 37°C in a 5% CO_2 atmosphere. For experiments of depolimerazation of microtubules cells were incubated in fresh medium with 3mg/ml of nocodazole (Sigma Aldrich) for 10 minutes. Sphingomyelin on plasma cellular membrane was depleted by 1 U/ml Sphingomyelinase from *Bacillus cereus* (Sigma Aldrich) for 30 minutes. All the details about TRPV1-YFP construct are described in (145). The TRPV1-EGFP construct was generated by site direct mutagenesis of p-TRPV1-E^0GFP as described in §3.4.1. The TRPV1-TagRFP construct was obtained by sub-cloning TRPV1 sequence from TRPV1-YFP construct in pTagRFP-N (§ 3.4.1) TRPV1-YFP is a kindly gift from Wei Cheng (159). TagRFP-αT construct was purchased by

Evrogen (FP145). The caveolin-1-EGFP plasmid was a kindly gift from L.Pelkmans (191)

6.4.2 *i*MSD and *i*MSD-FRET.

Measurements were carried out with a Leica AF6000 fluorescence microscope in Total Internal Reflection mode (TIRF), with a penetration depth of the evanescent wave less than 100 nm. Fluorescence was collected by using a 100x (NA 1.47) oil-immersion objective and was recorder cooled EM-CCD (Hamamatsu C1900-13). for STICS-FRET measurements on cell co-expressing TRPV1-EGFP and TagRFP-αT, and cell co-transfected with TRPV1-TagRFP and caveolin-1-EGFP excitation at 488 nm was used and emission was collected using a 502 dichroic mirror (Leica Microsystem) and filtered by a Semrock FF01-641/75-25 filter.

In detail, where not differently stated, TIRF time series were acquired at 10 ms time resolution by using the overlapping mode of CCD camera. Typical time series lasted at least 6000 frames (~60 seconds). *i*MSD analysis was performed by an custom-made MatLab library as previously shown (186). The contribution to the STICS function of an immobile fraction of particles was removed by proper filtering (161). Additional possible artifacts due to average image intensity temporal drift, were removed by subtracting the spatial-averaged image, as described in Ref (192).

Chapter

7

TRPV1 organization on plasma membrane: general model and conclusions

In chapter 3-6 we described several experimental results that shed light on the previously unknown diffusion/binding interplay of membrane TRPV1. In this final chapter we recast the acquired knowledge into a working model of TRPV1 behavior.

7.1 Molecular association of membrane TRPV1 with itself and other proteins

In vitro biochemical assays (73) and colocalization analysis on fixed cells (25) highlighted that TRPV1 and microtubules interact together in some way. Other experiments identified the cytoplasmic C-terminus of TRPV1 as hot-spot for binding to β-tubulin (74). The possible interaction between TRPV1 and

microtubules is particularly intriguing, since it would provide a connection between nociception and cytoskeletal remodeling. This was our starting point.

In this thesis we demonstrated for the first time in living cells the effective binding between basal or agonist-stimulated TRPV1 and microtubules. This result was accomplished by observing FRET between TRPV1 and α-tubulin labeled with optically-complementary fluorescent proteins. High-resolution FRET maps showed that the binding interactions occur within large membrane islets of size up to 900-1000 nm. Notably, microtubule disassembly (induced by nocodazole) led to the complete disappearance of the FRET signal. These findings demonstrated that: 1) TRPV1-tubulin binding takes place only when the latter protein is polymerized in functional microtubules, 2) the interaction between TRPV1 and microtubule is independent from the channel-activation status, and 3) the binding regions consist of supramolecular arrangement of several TRPV1 receptors. The TRPV1-microtubule complex was named TRPV1-T.

Earlier reports highlighted the positive role of TRPV1 activation in promoting microtubule disassembly and remodeling. Our results raise the question whether microtubules could be an essential factor to stabilize TRPV1, through binding, in its functional form. Remarkably, we found out that microtubule depolymerization yields a large fraction of membrane-immobile receptor, as well as a considerable loss of TRPV1 activity in terms of Ca^{2+} influx upon stimulation. By Fluorescence Anisotropy Analysis (FAIM) we revealed that the immobile fraction is composed by large receptor aggregates made up of several (likely ≥10) TRPV1 units. We applied FAIM and moment analysis of fluorescence fluctuations (N&B analysis) also to study TRPV1 oligomerization in the presence of integer microtubules, highlighting that TRPV1 at basal state can aggregate only up to tetramers. According to literature, functional TRPV1 has a well-defined tetrameric structure on the membrane(79).

The activation of the TRPV1 due to noxious stimulation is followed by the attenuation of the excitability of nociceptive sensory neurons, making nociceptors partially or totally refractory to subsequent stimuli (86). Depending on the refractory period, which can range from minutes and hours up to days, this phenomenon is known as acute desensitization, down-regulation, or defunctionalization (152). While Ca^{2+}-dependent mechanism of acute desensitization is known (92), long-term TRPV1 desensitization is poorly understood. It was hypothesized that long-term desensitization might involve TRPV1 withdrawal from the cell surface.

Interestingly, *Sanz-Salvador et al*. visualized the effective internalization of the receptor upon agonist stimulation and showed its independence from clathrin endocytotic pathway, although they were unable to reveal the actual mechanism (152). In this work, we demonstrated that caveolar endocytosis is an effective long-term desensitization mechanism of TRPV1. For the first time caveolin-1 (one of the most important protein in caveolar endocytosis) was identified by FRET as a molecular interactor of TRPV1 at membrane level and, most likely, as a powerful modulator of receptor long-term desensitization. In fact, we demonstrated that TRPV1 stimulation leads to cell internalization and positive co-localization of intracellular TRPV1 with caveosoma structures. The TRPV1-caveolin-1 complex was named TRPV1-C.

7.2 Membrane dynamics of TRPV1

By combining FRET with temporal image correlation analysis we were able to identify the dynamic features of TRPV1-T with respect to the whole membrane receptor pool. At first, we looked only at the temporal behavior of fluorescence fluctuations due to protein diffusion (tICS analysis). Albeit tICS did not provide the subtle details of TRPV1-T membrane dynamics, it clearly indicated that TRPV1-T should be identified with the functional (i.e. capable of agonist stimulation) form of the receptor at basal state, which is characterized by a very slow mobility within the bilayer (D~10^{-5} $\mu m^2/s$).

Next, we aimed at understanding the whole dynamic network of TRPV1 interactions within the membrane. For this goal, we applied a novel correlation analysis (*i*MSD) based on spatio-temporal image correlation spectroscopy (STICS). *i*MSD was also combined with FRET to follow specifically the dynamic features of TRPV1-T and TRPV1-C. *i*MSD-FRET highlighted intriguing dynamic and spatial features of TRPV1-T. Each TRPV1-T system does not move as single complex, but it participates to a concerted movement of large membrane islets (up to 900-1000 nm). These islets diffuse slowly within the cell membrane and are actively driven by integer microtubule chains. Notably, sphingomyelin is a necessary constituent of these islets, as demonstrated by the disappearance of the TRPV1-T pools upon sphingomyelin digestion by sphingomyelinase. The presence of sphingomyelin

suggests that lipid rafts are essential constituents of these large islets, in agreement with a previous study that pointed out the correlation between cholesterol and TRPV1 functionality (70). Although more experimental data are necessary to clarify the structural features of TRPV1-T, we can sketch a first model in which many TRPV1 molecules move, in a coordinated way, either along microtubule chains that reside underneath the membrane, or tethered to microtubule chain-ends. The functional role of TRPV1-T is witnessed also by the strict control over its membrane concentration by the cell.

Conversely, FRET-*i*MSD results showed that TRPV1-C is confined into small sphingomyelin-enriched membrane patches likely identifiable with caveolar structures. These structures were found to be almost immobile for times up to 1 min. The binding of TRPV1 to caveolin-1, however, displayed a reversible dynamics with a characteristic time of about 16 s. Analysis of autocorrelation amplitude highlighted that TRPV1-C concentration on the membrane is independent of the expression level of the receptor. This indicates a strict biochemical control by the cell over the amount of membrane TRPV1-C, in order to fulfill its biological role. Significantly, upon agonist (RTX) administration, TRPV1 and caveolin-1 were mostly removed from the cell membrane and translocated to the cell interior in caveolar structures. These findings suggest that TRPV1-C is the first step towards caveolar endocytosis of the receptor and, likely, its desensitization.

One may question whether the regions containing TRPV1-C are subsets of the large TRPV1-T islets, on account of the recognized interplay between caveolae and microtubules (55,193). Our findings suggest that TRPV1-C and TRPV1-T are *spatially decoupled*: in fact, the *i*MSD trace at time zero of TRPV1-C did not display large patch-like arrangements as in the case of TRPV1-T, a feature that would be expected if the two TRPV1 pools were accommodated in the same membrane location. Additionally, microtubule disassembly did not affect the amplitude of TRPV1-C correlation.

Finally, a third, isotropically- and fast-moving TRPV1 subpool was identified by *i*MSD analysis and named TRPV1-I. Notably, TRPV1-I concentration on the membrane was found to depend on the expression level of the receptor. This finding strongly suggests that TRPV1-I is not directly involved in the receptor functional role, but represents a TRPV1 “reservoir”. TRPV1-I could be a precursor of the TRPV1-T functional receptor: in fact, microtubule disassembly by nocodazole leads to the conversion of TRPV1-T into the freely-moving TRPV1-I subpool.

7.3 Functional model of TRPV1

Recently, a working model of membrane TRPV1 was presented. This model accommodates most of the results we presented in Chapters 3-6 and it integrates additional biochemical data published by other authors on the phosphorylation of the receptor (51). According to this model, TRPV1 assembles firstly as a dimer, then tetramerizes, and eventually is sensitized towards agonist activation by phosphorylation carried out by kinases on the cytoplasmic C-terminus of the receptor. In this model, microtubules promote tetramerization but are detached from TRPV1 upon phosphorylation. This model is a convenient starting point to interpret our intriguing *i*MSD data. In fact, the identification of the sensitized receptor with TRPV1-C would explain the spatial decoupling of TRPV1-C and TRPV1-T. Enabling sensitization upon phosphorylation and de-sensitization upon internalization would account for the fine regulation of receptor activity that is required to fulfill its biological role. Further activation of TRPV1 generates also Ca^{2+} influx that causes rapid disassembly of microtubules and shifts the equilibrium towards the tubulin dimer as a feedback mechanism (Fig. 7.1). Vice-versa, independent microtubule disassembly leads to TRPV1 aggregation and the impairment of receptor function. On overall, this subtle molecular interplay oversees the correct functioning of the receptor and prevents the over-activation of the cell response following noxious stimuli.

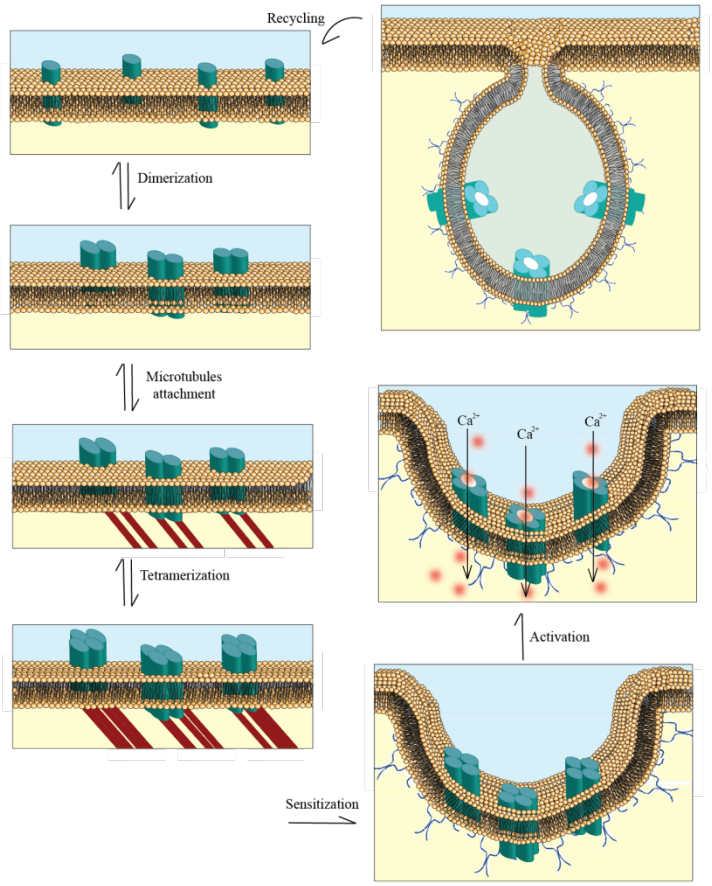

Figure 7.1 A general model depicting TRPV1 activity and functionality. The life-cycle of TRPV1 is described starting from the upper left panel and moving counter-clockwise. TRPV1 is initially monomer after expression and proteic maturation. Then, the receptor forms stable dimers that represent an immature form of the receptor. At physiological condition microtubules filaments attach to dimers and stabilize TRPV1 in tetrameric form. Translocation of the TRPV1 tetramer on caveolar regions, dissociation of microtubules and phosphorylation is required to sensitize the receptor towards external signals. Agonist stimulation of TRPV1 results in Ca^{2+} influx and a cascade of signaling events. Yet, after prolonged activation the desensitization mechanisms of TRPV1 take place and involve withdrawal of the receptor from the cell surface via caveolar endocytosis.

Appendix

A

Image Correlation spectroscopy: mathematical foundations

The starting point of ICS analysis is the generalized spatiotemporal correlation function (161):

$$G(\mathbf{s},\tau)=\frac{\langle F_a(\mathbf{r},t)\cdot F_b(\mathbf{r}+\mathbf{s},t+\tau)\rangle}{\langle F_a(\mathbf{r},t)\rangle_t\cdot\langle F_b(\mathbf{r},t+\tau)\rangle_{t+\tau}}-1\,, \qquad [A.1]$$

where $F(\mathbf{r},t)$ is the intensity at position **r** in the image recorded at time *t*, and $\langle F(\mathbf{r},t)\rangle_t$ is the average intensity of that image at time *t* (i.e. average is taken only on spatial dimensions). **s** and τ represent the spatial and temporal lags of correlation, respectively. To avoid confusion, the spatial components of the vectors **r** and **s** will be distinguished and denoted as (x,y,z) and (ξ,χ,ζ), respectively. For generality, we introduce the subscripts *a* and *b* in Eq. 2.7 to refer to two *distinct* wavelength detection channels. If *a*=*b*, Eq.A.1 expresses the *auto*correlation function of the system; conversely, *a*≠*b* refers to a *cross*correlation function. In the following, only the autocorrelation function will be considered and the subscripts *a* and *b* are dropped.

Starting from the definition of spatiotemporal autocorrelation (Eq. A.1) it can be demonstrated that $G(\mathbf{s},\tau)$ is expressed by a sequential convolution ($\otimes$) of two functions, $p(\mathbf{s},\tau)$ and $W(\mathbf{s})$ (186), according to:

$$G(\mathbf{s},\tau) = \frac{\gamma}{\langle N \rangle} p(\mathbf{s},\tau) \otimes \left[W(\mathbf{s}) \otimes W(\mathbf{s}) \right]. \qquad [A.2]$$

The terms constituting Eq. A.2 deserve particular attention:

- $p(\mathbf{s},\tau)$ is a probability function describing the dispersive dynamics of diffusing molecules. Actually, $p(\mathbf{s},\tau)$ corresponds to the Green's function that is adopted for solving the Fick's equation once boundary conditions are stated. Here, an important case is represented by *isotropic free diffusion*. This condition holds whenever diffusing molecules have size negligible as compared to the focal volume, and the latter is in turn spatially negligible as compared to whole diffusion volume. In such a case, the Green's function of Fick's equation in a space of dimensionality *k* (*k*=1,2,3) is (194):

$$p(\mathbf{s},\tau) = \frac{1}{(4\pi D\tau)^{k/2}} \cdot \exp\left(-\frac{\mathbf{s}^2}{4D\tau} \right) \qquad [A.3]$$

- $W(\mathbf{s})$ is the fluorescence intensity distribution corresponding to the imaged focal volume in CLSM or TIRFM systems, and corresponds to the Point Spread Function (PSF). In most systems, $W(\mathbf{s})$ is well approximated by a Gaussian distribution (see Eq. 2.2, §2.1.1)
- γ is a scalar related to the actual shape of the PSF.

Before trying to solve Eq. A.2, an important point has to be mentioned. In all ICS techniques the autocorrelation is calculated on a temporal stack of images collected in a given specimen area *without modifying the focal z position of the objective*. So, we have always ζ=0, and the autocorrelation function actually becomes function of two spatial coordinates only, i.e. $G(\mathbf{s},\tau) \rightarrow G(\xi,\chi,\tau)$. These two coordinates

represent the spatial lags of correlation within the optical *xy* plane containing the image.

Integration of Eq. A.2 is possible only for those special cases for which analytical forms of $p(\mathbf{s},\tau)$ and $W(\mathbf{s})$ are available. A very important example is represented by the combination of *isotropic free diffusion* (Eq. A.3) and Gaussian PSF. In such a case, for 3D diffusion (k=3 in Eq. A.3), we have:

$$G_{D\text{-}3}(\xi,\chi,\tau) = G(0,0,0)\cdot\left(1+\frac{\tau}{\tau_D}\right)^{-1}\cdot\left(1+\frac{\tau}{S^2\tau_D}\right)^{-1/2}\cdot\exp\left[\left(-\frac{\xi^2+\chi^2}{\sigma_{xy}^2}\right)\cdot\left(1+\frac{\tau}{\tau_D}\right)^{-1}\right], \quad [A.4]$$

where $G(0,0,0)$ is the zero-lag amplitude, S is the ratio between the axial and the radial resolution of the optical setup ($S=\sigma_z/\sigma_{xy}$ in our notation), and τ_D is the characteristic diffusion time of the molecules under observation.

Many interesting cellular processes take place in membrane compartments, i.e. within extended *planar* cellular structures. Here, diffusion must be considered as occurring in a 2D plane only, which is conventionally considered as coinciding with the *xy* plane of the images. In such a case, A.4 is recast as:

$$G_{D\text{-}2}(\xi,\chi,\tau) = G(0,0,0)\cdot\left(1+\frac{\tau}{\tau_D}\right)^{-1}\cdot\exp\left[\left(-\frac{\xi^2+\chi^2}{\sigma_{xy}^2}\right)\cdot\left(1+\frac{\tau}{\tau_D}\right)^{-1}\right]. \quad [A.5]$$

Regardless of the dimensionality of the diffusion space, τ_D is related to the molecular diffusion coefficient D through (167):

$$D = \frac{\sigma_{xy}^2}{4\tau_D} \quad [A.6]$$

Often, in biological contexts, the ideal case of isotropic diffusion does not apply, because the movement of the molecules is restricted or the mobility shows strong local changes. These deviations may be due to the confinement of the molecules

within cellular compartments or lipid domains of membranes, but also to nonspecific interactions with other molecules or cellular structures. In such cases, Eq. A.4 and A4.5 generalize to Eq. A.7 and A.8, respectively:

$$G_{D-3}(\xi,\chi,\tau) = G(0,0,0)\cdot\left(1+\left[\frac{\tau}{\tau_D}\right]^{\alpha}\right)^{-1}\cdot\left(1+\frac{1}{S^2}\left[\frac{\tau}{\tau_D}\right]^{\alpha}\right)^{-1/2}\cdot\exp\left[\left(-\frac{\xi^2+\chi^2}{\sigma_{xy}^2}\right)\cdot\left(1+\left[\frac{\tau}{\tau_D}\right]^{\alpha}\right)^{-1}\right], \quad [A.7]$$

$$G_{D-2}(\xi,\chi,\tau) = G(0,0,0)\cdot\left(1+\left[\frac{\tau}{\tau_D}\right]^{\alpha}\right)^{-1}\cdot\exp\left[\left(-\frac{\xi^2+\chi^2}{\sigma_{xy}^2}\right)\cdot\left(1+\left[\frac{\tau}{\tau_D}\right]^{\alpha}\right)^{-1}\right]. \quad [A.8]$$

In Eq. A.7 and A.8 the anomalous diffusion behavior is cast into the α coefficient. Isotropic diffusion holds for $\alpha = 1$; the case $\alpha > 1$ is typical of "guided diffusion", i.e. diffusion partially driven by energy-dependent processes, whereas the case $\alpha < 1$ is attributable to restricted (confined) diffusion (195). Eq. A.6 is now rewritten as:

$$D = \frac{\sigma_{xy}^2}{4(\tau_D)^{\alpha}}. \quad [A.9]$$

Notably, for $\alpha \neq 1$, D stands for an empirical transport coefficient of fractional time dimension (in some cases denoted as apparent diffusion coefficient or D_{app}).

So far, fluorescence fluctuations were attributed to diffusion motion only. However, diffusion-independent molecular mechanisms that change the fluorescence brightness also contribute to fluctuations, and they are inevitably recorded into the autocorrelation function. This phenomenon is called brightness flickering. In the simplest case brightness flickering is accounted for by adding an exponential term to the diffusive autocorrelation function, i.e.:

$$G_{3D}(\xi,\chi,\tau) = G_{D-3}(\xi,\chi,\tau)\cdot\exp\left(-\frac{\tau}{\tau_{\Phi}}\right), \qquad [A.10]$$

$$G_{2D}(\xi,\chi,\tau) = G_{D-2}(\xi,\chi,\tau)\cdot\exp\left(-\frac{\tau}{\tau_{\Phi}}\right), \qquad [A.11]$$

where τ_* is the characteristic time of brightness flickering and G_{D-3} and G_{D-2} are given by Eq. A.8 and A.9, respectively. Despite its simplicity, the exponential term describes properly a number of photophysical phenomena, including quenching or FRET upon complex formation and triplet states.

Appendix

B

Photoswitching of E222Q GFP mutant linked to TRPV1 for advanced imaging applications

The discovery of phototransformable FPs (PTFPs) from *Anthozoa* species triggered a revolution in the field, notably by enabling single-molecule localization-based super-resolution microscopy (196,197). Three types of phototransformations can be distinguished: photoactivation and photoconversion are nonreversible processes that result from covalent modifications of the FP matrix, whereas photoswitching refers to the reversible transition between a fluorescent on-state and a non-fluorescent off-state.

Reversible photoswitching (photochromism) in FPs has first been observed for yellow derivatives of *Aequorea victoria* GFP (YFP) at single-molecule level by alternating cyan (488 nm) and violet (405 nm) excitation (198). Bulk photoswitching at room temperature was discovered also for other GFP derivatives, notably CFP (199) and several yellow variants such as, Citrine (199), E^2GFP (200), and YFP-10C (201). In all cases, the photoswitching contrast was not high, on account of the coexistence of non-photoswitchable populations of molecules. Reversible light-induced *cis-trans* isomerization of the chromophore and/or chromophore protonation was hypothesized as the most likely reasons for the observed photochromism.

The discovery of FPs from *Anthozoa* species such as corals or anemones triggered a considerable boost in FP research. The first photochromic optical highlighter for biological experiments was obtained upon engineering a *Pectiniidae* coral FP, yielding the well-known photochromic Dronpa (202). The creation of Dronpa was followed by the introduction of other photochromic proteins exhibiting improved properties such as better fluorescence brightness, enhanced switching contrast, tunable switching quantum yields, increased fatigue-resistance, or red-shifted emission color (203). Mechanistic investigations of some of these photochromic proteins, generally based on a combination of crystallographic, spectroscopic, and molecular dynamics approaches (204-209), suggested photoswitching mechanisms based on coupled *cis-trans* isomerization and protonation changes of the chromophore.

In this context, we recently found that the E222Q amino acid replacement confers efficient photochromicity in otherwise poorly switchable green fluorescent protein variants of different optical properties (210). The generality of E222Q substitution was tested on both green and yellow FP mutants.

Here we shall present the photochromic EYQ1, a yellow-emitting E222Q mutant which was fused to TRPV1 in order to investigate the receptor distribution on cell membrane by means of novel imaging approaches that take advantage of the intrinsic photochromicity of the fluorescent label (158).

B.1 EYQ1

B.1.1 Optical properties of EYQ1 mutant in the native state

With respect to wtGFP, EYQ1 is characterized by three aminoacid replacements (F64L/T203Y/E222Q). The T203Y mutation confers the yellow-emitting properties to the protein (126), whereas the E222Q is at basis of its photochromicity; F64L is known to reduce the chromophore maturation time (103).

Three ground states characterized by different protonation patterns of the chromophore and nearby Glu222 contribute to the 400–530 nm region of the absorption spectrum of GFPs (125). .Nonetheless, the removal of Glu222 leads to only two protonation states affecting the protein optical properties: (i) neutral chromophore (protonated phenol group), hereafter denoted as A state, and (ii)

anionic chromophore (deprotonated phenol group), hereafter denoted as B state. State A absorbs at 400–410 nm (Fig B.1 full red line) and, in EYQ1 protein, is practically non-fluorescent (quantum yields about 10^{-3}). State B absorbs at 480–500 and it emits yellow fluorescence in EYQ1 (λ_{em} = 525 nm). The quantum yields of B state is 0.72 (210).

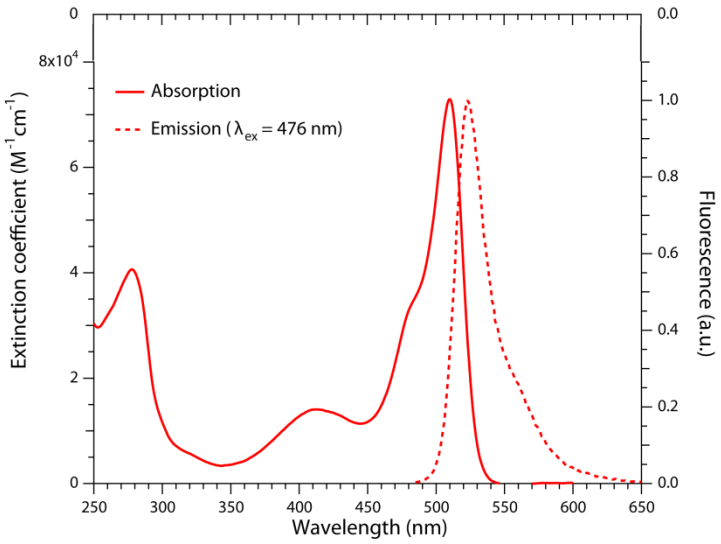

Figure B.1. Optical properties of EYQ1. Absorption (full lines) and emission spectra (dotted lines).

States A and B can be reversibly interconverted by changing the pH of the solution surrounding the protein. Removal of E222 or its stabilization in the neutral form has been repeatedly shown to favor the B state from a thermodynamic point of view (125,211). Indeed, EYQ1 has p*K* = 6.87 (210). Thus, at physiological pH (7.2–7.4) state B is predominant.

B.1.2 Photoswitching of EYQ1 mutant

At physiological pH and above, illumination near the maximum wavelength of the B state of EYQ1 leads to a progressive decrease of fluorescence both *in vitro* and *in cells*. Analysis of the *in vitro* absorption of EYQ1 showed that the fluorescence

decrease was associated with a parallel decrease of the B absorption band and an increase of a nonfluorescent state (hereafter denoted as A_t) located at 400–415 nm (Fig. B.2). Upon irradiation of A_t, the B state was partially restored, as well as the protein fluorescence.

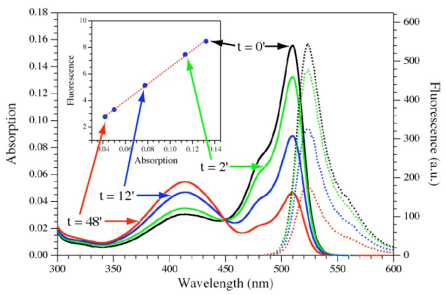

Figure B.2. *On→off* photoswitching of EYQ1. Photoswitching of EYQ1 *in vitro* at pH 7.4 upon illumination at 514 nm (0.5 W cm^{-2}) followed by absorption (full lines) and emission (λ_{ex} = 476 nm, dotted lines) spectra taken at different times. Photoswitching leads to population decrease of *cis* anionic B state (λ = 510 nm) and to population increase of *trans* neutral At state (λ = 413 nm). The latter state is non-emissive, and global EYQ1 fluorescence decreases proportionally to the deployment of emissive B state (inset plot).

Actually, a photostationary condition, for which the on- and off-switching rates compensate each other, was eventually reached at any illumination wavelength within the absorption range of the B band. As the switching rate is linearly proportional to the number of absorbed photons, the fraction of photoswitched protein depends on the overlap of B and A_t absorption bands (212).

O*n*↔*off* photoswitching experiments on the protein entrapped in a polyacrylamide gel showed that a minor fraction (≤3%) of the protein was irreversibly photobleached at each cycle (this figure is called *fatigue resistance*) (Fig. B.3). 3% of signal loss at each cycle means that more than 70 cycles are required for the fluorescence to drop below 10% of the initial value (213). Note that the observed fatigue resistance is comparable to that of photochromic FPs widely applied to super-resolution and pulse-chase labeling studies (214).

Interestingly, the photoconverted A_t state of EYQ1 relaxed thermally back to the initial *cis* state (B) after the illumination had stopped. The thermal decay followed a first-order kinetics with relaxation time constant related to the pH of the solution

(210). Similarly to what proposed for mutants from *Clavularia* (206) and Dronpa (205), this behavior was accounted for by the ionization of the chromophore in the *trans* state. In such a case, different energy barriers between *trans* and *cis* configurations exist for the protonated and anionic chromophore states, leading to thermal relaxation with pH-dependent rates. This hypothesis was experimentally demonstrated by coupled photoconversion/pH-jump experiments, and the pH-dependent ionization site was assigned to the phenolic function of the EYQ1 chromophore. Significantly, the *trans* form of the chromophore displayed a much higher pK as compared to the *cis* form (+2-3 pH unit), presumably owing to the lack of surrounding proton acceptor residues.

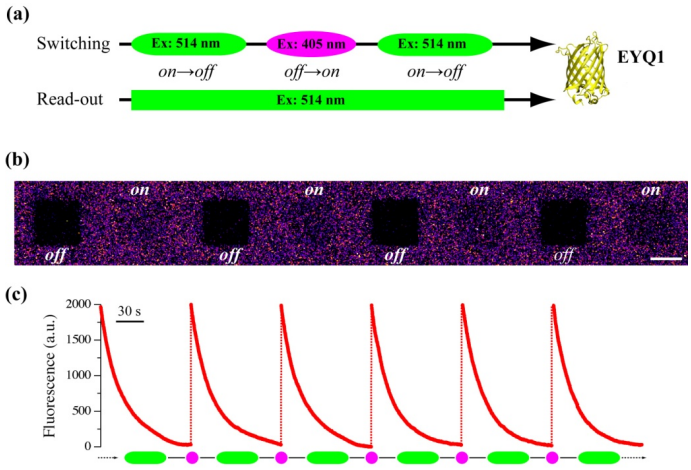

Figure B.3. Photochromic behavior of EYQ1 (A) Photoswitching scheme of the yellow photochromic mutant EYQ1. Switching was carried out by alternating 514 and 405 nm excitation; fluorescence read-out was provided by continuous 514 nm excitation. Note that illumination at 514 nm was tuned to obtain concomitant switching off and fluorescence read-out. (B) Photoswitching of EYQ1 immobilized in a polyacrylamide gel at pH 7.8 imaged by confocal microscopy A 13.1 µm × 13.1 µm was photoswitched according to the scheme of panel (A). Light intensities at focal plane were 0.8 kW/cm^2 for 514 nm and 0.06 kW/cm^2 for 405 nm. Scale bar = 5 µm. (C) EYQ1was photoswitched according to the scheme of panel (A). At the bottom of the panel, the alternating sequence of 514/476 and 403 nm illumination is pictorially represented by green/cyan and violet ellipses. Light intensities at focal plane were 20−50 kW/cm^2 for 514 nm and 2 kW/cm^2 for 403 nm (Adapted from (210)).

These findings led to a photophysical model that successfully rationalized all experimental results on EYQ1 and other E222Q proteins (Figure B.4) (215).

Natively, the chromophore has a *cis* stereochemistry and is characterized by a pH-dependent equilibrium between a neutral phenol (protonated) state A and a phenolate (anionic) state B shifted towards B at physiological pH (pK_{cis} EYQ1 = 6.87 (210)). Only B is fluorescent (yellow), probably because the lack of E222 forbids the ESPT mechanism from the neutral state A (216). Illumination at B maximum wavelength (510 nm) yields *cis*→*trans* photoisomerization of the chromophore. On account of its significantly lower acidity (pK_{trans} ≥ pK_{cis} + 3), only the *trans* neutral chromophore (state A_t) becomes populated at pH < 9.

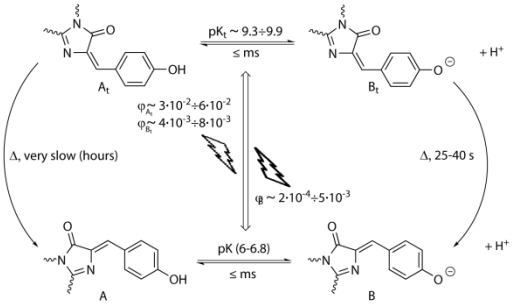

Scheme B.4. Photoisomerization of E222Q GFP mutants. Natively, the protein has a *cis* chromophore charachterized by two fundamental states differing for the protonation state: neutral (**A**) and anionic (**B**). Interconversion between **A** and **B** at ground state is characterized by pK_a values in the 6-7 range. Illumination of B state leads to *cis*→*trans* photoisomerization to dark $\mathbf{A_t}$ state for pH < 9. Illumination of $\mathbf{A_t}$ leads to *trans*→*cis* photoisomerization to emissive **B** state. These two photoprocesses are at basis of the *on*↔*off* photoswitching. The *trans* chromophore has a much higher pK_a (denoted as pK_t) than the *cis* form. Thermal relaxation back from *trans* to *cis* has a rather low activation energy barrier for the anionic $\mathbf{B_t}$ state (relaxation times of a few tens of second), whereas it is strongly unfavored for $\mathbf{A_t}$ (relaxation times of hours).

Similarly to A, A_t absorbs at 400–410 nm and is *non-fluorescent*; hence, the photoisomerization results in the protein switching from an *on* state to an *off* state. The optical similarity between different stereochemical configurations (*cis*/*trans*) of the neutral state was reported also for Dronpa (217). Analogously, the *trans* anionic state of the chromophore (B_t) has optical properties very similar to B. Once in the *trans* form, the chromophore can return to the *cis* configuration in two ways: (1) by photoisomerization upon illumination at maximum wavelength of the predominantly

populated *trans* state or (2) by thermal relaxation (all calculations point out that the *trans* states have a larger free-energy than the *cis* states (212)). The first pathway is at basis of the observed efficient photochromic properties and, at pH where the B and A_t states are stabilized (between 7 and 9), allowed for *on↔off* cycling of fluorescence. The complete kinetic analysis of photoisomerization showed that B conversion is associated with switching yields of 2×10^{-4}, whereas back-photoisomerization of A_t and B_t states displayed switching yields between 4×10^{-3} (210).

The second pathway is pH-dependent, as the energy barrier for thermal isomerization between the B_t and B states is much less than between the A_t and A states. Thus, the thermal relaxation rate is practically proportional to the population of B_t, which is in turn modulated by pH. Note that the knowledge of the spontaneous thermal relaxation rate from photoconverted states is essential to plan the application of any photochromic mutant to imaging studies, because it defines (together with irreversible photobleaching) the time-window of stable non-emission (or emission for inverse photochromic mutants such as Padron (208)) from single molecules as well as from large molecular ensembles (*e.g.* subcellular regions). In particular we found out that *trans* dark states of EYQ1 are stable for several minutes at physiological pH.

For further applications in the cellular context, where pH uniformity is not granted in all locations, we set out to investigate whether A_t or B_t, are the *primary* product of photoisomerization of EYQ1 (and other switching variants). By flash-photolysis it was found that photoisomerization of B yields A_t, thus implying that the *cis-trans* isomerization is concomitant with the change in chromophore protonation state. Although the experimental set-up did not permit the visualization of the state populations in the first 2 μs after photoswitching, these results strongly support a coordinated isomerization/protonation mechanism from B excited state (B*) (158). Significantly, some authors have suggested that, in the *cis-trans* photoswitching of other photochromic fluorescent proteins (*e.g.* Dronpa), the protonation and isomerization are two closely related events that take place in a very short time delay (218,219). This observation suggests an impressive degree of structural and photophysical resemblance among fluorescent proteins whose primary sequences display often a low degree of similarity.

B.2 TRPV1-EYQ1 for Superresolution Optical Fluctuation Imaging (SOFI)

B.2.1 SOFI

Super-resolution fluorescence microscopy overcomes the diffraction resolution barrier and allows investigation of mesoscale/nanoscale features with enhanced spatial detail. In general, all of these approaches generate "diffraction-unlimited images" by using the physical properties of fluorescent probes to distinguish emissions from two nearby molecules within a diffraction-limited region. These super-resolution approaches can be divided into two primary classes (220). The first category is constituted by patterned illumination. In such a way, not all molecules emit simultaneously, thereby achieving sub-diffraction limit resolution. This category includes stimulated emission depletion (STED) microscopy (221,222) and the related RESOLFT technology (223) as well as saturated structured illumination microscopy (SSIM) (224,225). The second category takes advantages of single-molecule imaging, using photoswitching or other mechanisms to stochastically activate individual molecules within the diffraction-limited region at different times. Images with subdiffraction resolution are then reconstructed from the measured positions of individual fluorophores. This second class includes stochastic optical reconstruction microscopy (STORM) (226), photoactivated localization microscopy (PALM) (196), and fluorescence photoactivation localization microscopy (FPALM) (197). Although these two families use different approaches to accomplish subdiffraction resolution, they share important characteristics. Indeed, in both cases, a physical or chemical property of the fluorophore is used to image it in different states (i.e., "on" and "off"), enabling them to be resolved from each other (227).

A recent addition to this field is *Superresolution Optical Fluctuation Imaging* (SOFI), based on the statistical analysis of temporal fluorescence fluctuations. SOFI does not require specialized equipment and can produce subdiffraction images over a broad range of imaging conditions, including low signal-to-noise and high background (228,229). In SOFI, a dataset of tens or hundreds of images is acquired at high speed, using photochromic fluorophores that can switch between a fluorescent and nonfluorescent state in a stochastic way (230). In intensity images, the signal in each pixel is given by the superposition of the fluorescence originating from different, nearby emitters. In a SOFI image each pixel is associated with a value that is obtained from the *n*th-order cumulant of the original pixel time series.

The *n*th-order cumulant (a quantity related to the *n*th-order correlation function) filters the photoswitching intensity signal in such a way that only highly correlated fluctuations emerge. The fluorescence signal contribution of emitters in neighboring pixels will yield poor correlation values, thus leading to an increased resolution (231). The exact resolution improvement depends on the order of the cumulant analysis (228). In addition to robust spatial resolution improvements, SOFI allows improved contrast, background rejection, and favorable temporal resolution (229). Whereas SOFI can be performed on any sufficiently sensitive imaging system, including confocal systems, in practice it is most conveniently applied to wide-field imaging systems, owing to the increased efficiency afforded by the parallel read-out of multiple pixels.

The underlying theory can be described (231) starting from a sample of *N* single, independently fluctuating emitters, located at position r_k (Fig. B.5) and having a time-dependent molecular brightness $\varepsilon_k \cdot s_k(t)$. In this case, the resulting fluorescence source distribution is given by:

$$\sum_{k=1}^{N} \partial(r - r_k) \cdot \varepsilon_k \cdot s_k(t) \qquad [B.1]$$

where ε_k is the constant molecular brightness and $s_k(t)$ is a time-dependent fluctuation.

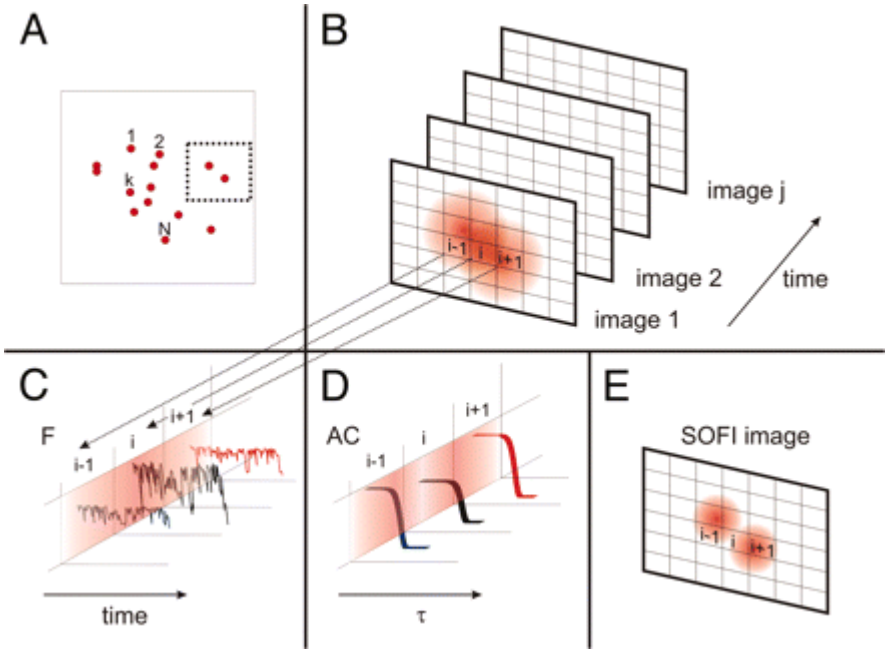

Figure B.5. Principle of SOFI. (A) Emitter distribution in the object plane. Each emitter exhibits fluorescence intermittency, which is uncorrelated with the others. (B) Magnified detail of the dotted box in panel A. The signal from the emitter fluorescence distribution is convolved with the systems PSF and recorded on a subdiffraction grid (e.g., pixels of the CCD-camera). Two neighboring emitters, for example, cannot be resolved because of the optical diffraction limit. The fluctuations are recorded in a movie. (C) Each pixel contains a time trace, which is composed of the sum of individual emitter signals. (D) The second-order correlation function is calculated from the fluctuations for each pixel. (E) The SOFI intensity value assigned for each pixel is given by the integral over the second-order correlation function. The second-order correlation function is proportional to the squared PSF, thus increasing the resolution of the imaging system by a factor of $\sqrt{2}$. Taken from (231).

We shall assume that the positions of emitters do not change during the image acquisition; temporal changes are caused only by emission blinking.

The fluorescence signal $F(r,t)$ at position r and time t is given by the convolution of the system's PSF $U(r)$ and the fluorescence source distribution (Eq. B.1 and Fig B.4B and C)

$$F(r,t) = \sum_{k=1}^{N} U(r - r_k) \cdot \varepsilon_k \cdot s_k(t) \qquad \text{[B.2]}$$

Assuming that the sample is in stationary equilibrium during acquisition, the fluctuations can be expressed as zero-mean fluctuations:

$$\begin{aligned} \delta F(r,t) &= F(r,t) - \langle F(r,t) \rangle_t \\ &= \sum_k U(r - r_k) \cdot \varepsilon_k \cdot \left[s_k(t) - \langle s_k(t) \rangle_t \right] \\ &= \sum_k U(r - r_k) \cdot \varepsilon_k \cdot s_k(t) \end{aligned} \qquad \text{[B.3]}$$

where $\langle ... \rangle_t$ denotes time averaging. The second-order autocorrelation function $G_2(r,t)$ is then given by (Fig. B.4D):

$$\begin{aligned} G_2(r,t) &= \langle \delta F(r, t+\tau) \cdot \delta F(r,t) \rangle_t \\ &= \sum_{j,k} U(r - r_j) U(r - r_k) \cdot \varepsilon_j \cdot \varepsilon_k \cdot \langle \delta s_j(t+\tau) \delta s_k(t) \rangle \\ &= \sum_k U^2(r - r_k) \cdot \varepsilon_k^2 \cdot \langle \delta s_k(t+\tau) s_k(t) \rangle \end{aligned} \qquad \text{[B.4]}$$

In eq. B.4 we assumed that the emission of different emitters is not correlated in time so that all cross-correlation terms $\langle \delta s_j(t+\tau) s_k(t) \rangle$ with $j \neq k$ vanish. The second-order autocorrelation function thus appears as a simple sum of the squared PSF, weighted by each emitter's squared brightness and molecular correlation function $\langle \delta s_k(t+\tau) s_k(t) \rangle$.

The value of $G_2(r,t)$ for a time lag τ defines a SOFI image, the only difference between each image being the weighting of the squared PSF with the molecular correlation function.

If the original PSF of the optical system can be approximated by a 3D Gaussian distribution, it follows from Eq. B.4 that the width of the "new" PSF is reduced by a factor of $\sqrt{2}$ along all three dimensions, thus increasing the optical resolution of the second-order SOFI image. Because the second-order correlation function involves the square of the PSF, it is natural to look into higher-order correlation functions, generate higher powers of the PSF, and therefore further increase the resolution. The *n*th-order correlation function is given by:

$$G_n(r,\tau_1,...,\tau_{n-1}) = \left\langle \delta F(r,t)\delta F(r,t+\tau_1)\cdots\delta F(r,t+\tau_{n-1})\right\rangle_t \qquad [B.5]$$

G_n can be easily computed in a straightforward manner, because the above formula states that the acquired signal fluctuations have to be multiplied for $n-1$ time lags to obtain G_n. To generate SOFI images of higher orders, it is, however, necessary to transform the *n*th-order correlation functions into *n*th-order cumulant functions $C_n(\mathbf{r},\tau_1,\ldots\tau n_{-1})$. The reason is that all cross-terms caused by lower-order correlation contributions are eliminated in cumulants, so that the *n*th-order cumulant consists only of terms containing the *n*th power of the PSF.

Beside cumulant analysis, SOFI can take advantage of cross-cumulant calculation by determining the cross correlation between pixels that surround the pixel of interest. The mathematical description of this approach (228) is beyond the scope of this short overview, but it is worth mentioning that the additional information of cross-cumulants can be used to reduce the noise in SOFI images even though no additional resolution is gained. This is especially useful when short acquisition times are used.

B.2.2 TRPV1-EYQ1 for SOFI

So far, most of the reported optical switches for SOFI applications are fusion constructs of the reversibly photoswitchable Dronpa protein (232). Dronpa is a green emitter with optical properties similar to the popular genetically encodable marker EGFP. Yet, SOFI is in principle applicable to any optical switcher. On account of the peculiar optical properties of EYQ1, namely its rather high photoswitching yields (similar to Dronpa), and its yellow emission that affords an

intermediate detection channel between those of green and red fluorescent proteins, we set out to test this mutant for SOFI application. More specifically, we engineered a TRPV1-EYQ1 fusion construct to image the morphological pattern of the receptor on the cell membrane at spatial scales below the diffraction limit (<250-300 nm).

TRPV1-EYQ1 was obtained by site direct mutagenesis of TRPV1-EYFP construct. The photochromic capability of this construct were assessed in CHO K1 cells by TIRF microscopy (233). Excitation was set to 488 nm, the emission was collected between 520 and 550 nm, and a dichroic filter at 502 nm separated out excitation from emission.

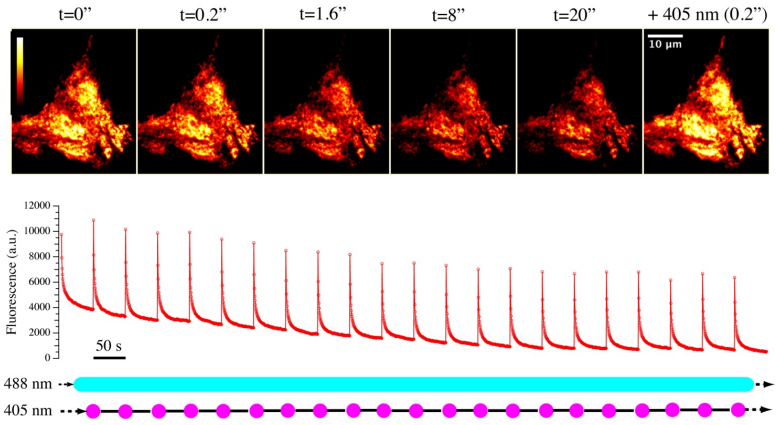

Figure B.6. *On⇔off* photoswitching cycles of EYQ1 linked to TRPV1 receptor and expressed on the membrane of CHO cell. Microscopy images were taken in TIRF mode. Upper panel: TRPV1-EYQ1 on a cell membrane was concomitantly imaged and switched off by excitation at 488 nm; the first 5 panel show the progressive decay of TRPV1-EYQ1 fluorescence with time; the last panel shows the effect of adding a brief 405 nm pulse: the original fluorescence was almost completely restored. Lower panel: mean fluorescence of the same cell undergoing 22 *on⇔off* photoswitching cycles; below is reported, as a colored scheme, the illumination sequence of 488 and 405 nm lasers.

Results showed that TRPV1-EYQ1 retains the same photoswiching behavior of EYQ1 alone (Fig. B.6), with a similar irreversible loss per switching cycle (3-4%). Fluorescence flickering of TRPV1-EYQ1 at membrane level was very evident when the acquisition time was shortened to 10-20 ms. 488 nm is a convenient wavelength to promote the reversible photoswitching of EYQ1, since at this wavelength the dark neutral state retains a non negligible absorption (Fig. B.2), eventually affording a

photostationary state between *off* and *on* states. Thus, we set out to collect time-lapses to generate SOFI images. Experimentally, we acquired 1000-5000 sequential images (10 or 20 ms per frame) and the time-lapse was analyzed by using a second-order cross-cumulant analysis followed by a Richardson-Lucy deconvolution, as implemented in the Localizer software (234). Fig B.7 displays the average intensity, as calculated on the time stack, relevant to the membrane of a single cell; this image corresponds to a conventional TIRF acquisition. Fig B.6B, instead, shows the image after SOFI processing. Although 2nd order SOFI increases the spatial resolution by only a √2 factor (squeezing the initial PSF from 270 nm to 190 nm), the SOFI image enhances greatly the understanding of the spatial morphology of receptor (Fig. B.7). In particular, TRPV1 forms a complex meshwork that extends all over the cell membrane and up to filipodia-like protrusions. The latter structures can be used to infer the spatial resolution enhancement, and the comparison of otherwise hidden substructures in the ≈200 nm scale (Fig B.7C). From the resolution viewpoint, these results are comparable to other examples reported in recent literature (230,235).

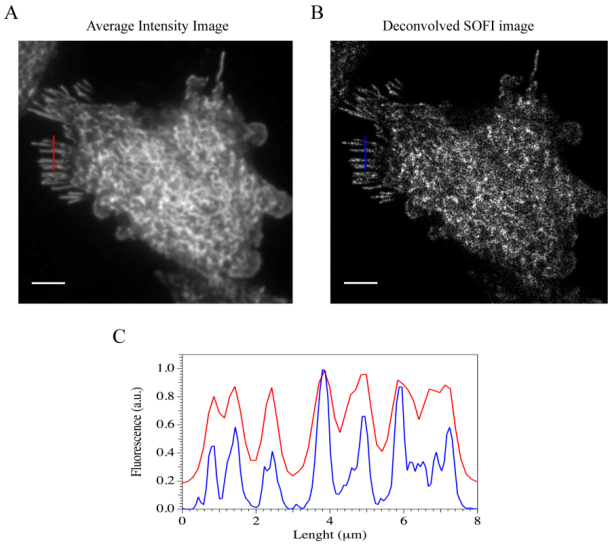

Figure B.7. Superresolution imaging with SOFI. TIRF intensity image (A) and deconvolved SOFI image (B) acquired on CHO cells transfected with TRPV1-EYQ1 (Scale bars 5 µm). (C) Intensity *vs,* distance along the red (panel A) and blue (panel B) lines.

In chapter 6 it was shown that the complexes of TRPV1 with microtubules (TRPV1-T) and caveolin-1 (TRPV1-C) do not overlap in space and reside in

membrane patches of significantly different sizes, 360±40 nm for TRPV1-C and 860±300 nm for TRPV1-T respectively. Accordingly, we set out to investigate whether SOFI was able to identify small structures, presumably attributable to TRPV1-C, in the meshwork of TRPV1 membrane distribution. For this, we collected time lapses (40 ms, 1250 images) over small regions of the membrane (7.2 x 7.2 mm), with the minimum pixel size allowed by our setup (110 nm); the time-lapse was processed according to the SOFI-deconvolution algorithm (Fig. B.8). We were able to identify a few substructures with size ranging between 200 and 300 nm that could be assigned to interaction patches between TRPV1 and caveolin-1 (Fig. B.8). It is worth noting that SOFI greatly enhanced the understanding of the spatial pattern of the receptor in these small membrane areas as compared to conventional TIRF.

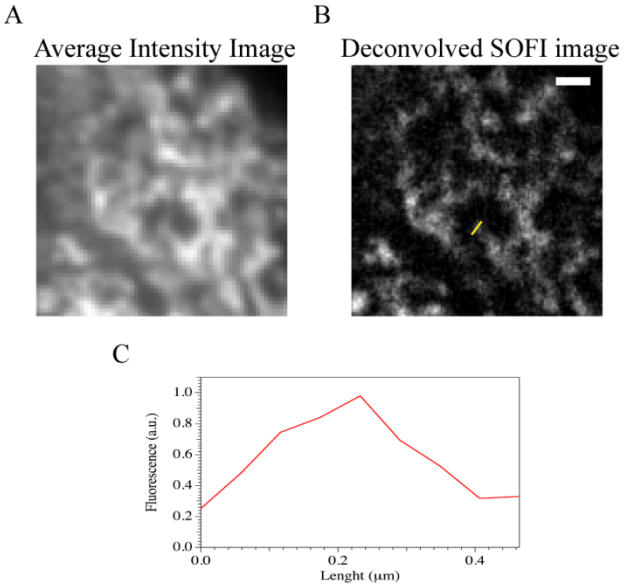

Fig. B.7. SOFI imaging of a small cell region. (A) TIRF and (B) second-order SOFI image of a selected region of cell (Scale bars, 1 µm.) (C) Plot profile along the yellow line in the B panel.

Bibliography

1. Singer, S. J., and Nicolson, G. L. (1972) *Science* **175**, 720-731
2. Feder, T. J., Brust-Mascher, I., Slattery, J. P., Baird, B., and Webb, W. W. (1996) *Biophys J* **70**, 2767-2773
3. Kusumi, A., Suzuki, K. G., Kasai, R. S., Ritchie, K., and Fujiwara, T. K. (2011) *Trends Biochem Sci* **36**, 604-615
4. Suzuki, K., Ritchie, K., Kajikawa, E., Fujiwara, T., and Kusumi, A. (2005) *Biophys J* **88**, 3659-3680
5. Bussell, S. J., Koch, D. L., and Hammer, D. A. (1995) *Biophys J* **68**, 1828-1835
6. Bussell, S. J., Koch, D. L., and Hammer, D. A. (1995) *Biophys J* **68**, 1836-1849
7. Nicolau, D. V., Jr., Hancock, J. F., and Burrage, K. (2007) *Biophys J* **92**, 1975-1987
8. Murase, K., Fujiwara, T., Umemura, Y., Suzuki, K., Iino, R., Yamashita, H., Saito, M., Murakoshi, H., Ritchie, K., and Kusumi, A. (2004) *Biophys J* **86**, 4075-4093
9. Kusumi, A., Koyama-Honda, I., and Suzuki, K. (2004) *Traffic* **5**, 213-230
10. Subczynski, W. K., Antholine, W. E., Hyde, J. S., and Kusumi, A. (1990) *Biochemistry* **29**, 7936-7945
11. Subczynski, W. K., Hyde, J. S., and Kusumi, A. (1991) *Biochemistry* **30**, 8578-8590
12. Pasenkiewicz-Gierula, M., Subczynski, W. K., and Kusumi, A. (1991) *Biochimie* **73**, 1311-1316
13. Kusumi, A., Fujiwara, T. K., Morone, N., Yoshida, K. J., Chadda, R., Xie, M., Kasai, R. S., and Suzuki, K. G. (2012) *Seminars in cell & developmental biology* **23**, 126-144
14. Subczynski, W. K., Pasenkiewicz-Gierula, M., McElhaney, R. N., Hyde, J. S., and Kusumi, A. (2003) *Biochemistry* **42**, 3939-3948

15. Lingwood, D., Ries, J., Schwille, P., and Simons, K. (2008) *Proc Natl Acad Sci U S A* **105**, 10005-10010

16. Kaiser, H. J., Lingwood, D., Levental, I., Sampaio, J. L., Kalvodova, L., Rajendran, L., and Simons, K. (2009) *Proc Natl Acad Sci U S A* **106**, 16645-16650

17. Simons, K., and Gerl, M. J. (2010) *Nat Rev Mol Cell Biol* **11**, 688-699

18. Levental, I., Lingwood, D., Grzybek, M., Coskun, U., and Simons, K. (2010) *Proc Natl Acad Sci U S A* **107**, 22050-22054

19. Chen, Y., Veracini, L., Benistant, C., and Jacobson, K. (2009) *J Cell Sci* **122**, 3966-3972

20. Martin, R. B., and Yeagle, P. L. (1978) *Lipids* **13**, 594-597

21. Schlessinger, J. (2000) *Cell* **103**, 211-225

22. Blume-Jensen, P., and Hunter, T. (2001) *Nature* **411**, 355-365

23. Lemmon, M. A., and Schlessinger, J. (2010) *Cell* **141**, 1117-1134

24. Brazer, S. C., Singh, B. B., Liu, X., Swaim, W., and Ambudkar, I. S. (2003) *J Biol Chem* **278**, 27208-27215

25. Goswami, C., Dreger, M., Otto, H., Schwappach, B., and Hucho, F. (2006) *J Neurochem* **96**, 254-266

26. Lisanti, M. P., Tang, Z., Scherer, P. E., Kubler, E., Koleske, A. J., and Sargiacomo, M. (1995) *Molecular membrane biology* **12**, 121-124

27. Williams, T. M., and Lisanti, M. P. (2005) *Am J Physiol Cell Physiol* **288**, C494-506

28. Rothberg, K. G., Heuser, J. E., Donzell, W. C., Ying, Y. S., Glenney, J. R., and Anderson, R. G. (1992) *Cell* **68**, 673-682

29. Scherer, P. E., Okamoto, T., Chun, M., Nishimoto, I., Lodish, H. F., and Lisanti, M. P. (1996) *Proc Natl Acad Sci U S A* **93**, 131-135

30. Walser, P. J., Ariotti, N., Howes, M., Ferguson, C., Webb, R., Schwudke, D., Leneva, N., Cho, K. J., Cooper, L., Rae, J., Floetenmeyer, M., Oorschot, V. M., Skoglund, U., Simons, K., Hancock, J. F., and Parton, R. G. (2012) *Cell* **150**, 752-763

31. Ortegren, U., Karlsson, M., Blazic, N., Blomqvist, M., Nystrom, F. H., Gustavsson, J., Fredman, P., and Stralfors, P. (2004) *Eur J Biochem* **271**, 2028-2036

32. Lockwich, T. P., Liu, X., Singh, B. B., Jadlowiec, J., Weiland, S., and Ambudkar, I. S. (2000) *J Biol Chem* **275**, 11934-11942

33. Swaney, J. S., Patel, H. H., Yokoyama, U., Head, B. P., Roth, D. M., and Insel, P. A. (2006) *J Biol Chem* **281**, 17173-17179

34. Remillard, C. V., and Yuan, J. X. (2006) *Mol Pharmacol* **70**, 1151-1154

35. Carver, L. A., and Schnitzer, J. E. (2003) *Nature reviews. Cancer* **3**, 571-581

36. Cohen, A. W., Razani, B., Schubert, W., Williams, T. M., Wang, X. B., Iyengar, P., Brasaemle, D. L., Scherer, P. E., and Lisanti, M. P. (2004) *Diabetes* **53**, 1261-1270

37. Muro, S., Wiewrodt, R., Thomas, A., Koniaris, L., Albelda, S. M., Muzykantov, V. R., and Koval, M. (2003) *Journal of Cell Science* **116**, 1599-1609

38. Parton, R. G., and Simons, K. (2007) *Nat Rev Mol Cell Biol* **8**, 185-194

39. Parton, R. G., and Richards, A. A. (2003) *Traffic* **4**, 724-738

40. Richter, T., Floetenmeyer, M., Ferguson, C., Galea, J., Goh, J., Lindsay, M. R., Morgan, G. P., Marsh, B. J., and Parton, R. G. (2008) *Traffic* **9**, 893-909

41. Wickstrom, S. A., Lange, A., Hess, M. W., Polleux, J., Spatz, J. P., Kruger, M., Pfaller, K., Lambacher, A., Bloch, W., Mann, M., Huber, L. A., and Fassler, R. (2010) *Dev Cell* **19**, 574-588

42. Nogales, E., Wolf, S. G., and Downing, K. H. (1998) *Nature* **391**, 199-203

43. Conde, C., and Caceres, A. (2009) *Nat Rev Neurosci* **10**, 319-332

44. Desai, A., and Mitchison, T. J. (1997) *Annu Rev Cell Dev Biol* **13**, 83-117

45. Burbank, K. S., and Mitchison, T. J. (2006) *Curr Biol* **16**, R516-517

46. Kirschner, M., and Mitchison, T. (1986) *Cell* **45**, 329-342

47. Inoue, S., and Salmon, E. D. (1995) *Mol Biol Cell* **6**, 1619-1640

48. Blitz, A. L., and Fine, R. E. (1974) *Proc Natl Acad Sci U S A* **71**, 4472-4476

49. Wolff, J. (2009) *Biochimica Et Biophysica Acta-Biomembranes* **1788**, 1415-1433

50. Bernier-Valentin, F., Aunis, D., and Rousset, B. (1983) *J Cell Biol* **97**, 209-216

51. Goswami, C. (2012) *J Neurochem* **123**, 1-13

52. Allen, J. A., Halverson-Tamboli, R. A., and Rasenick, M. M. (2007) *Nat Rev Neurosci* **8**, 128-140

53. Yan, K., Popova, J. S., Moss, A., Shah, B., and Rasenick, M. M. (2001) *J Neurochem* **76**, 182-190

54. Donati, R. J., and Rasenick, M. M. (2005) *Neuropsychopharmacology : official publication of the American College of Neuropsychopharmacology* **30**, 1238-1245

55. Head, B. P., Patel, H. H., Roth, D. M., Murray, F., Swaney, J. S., Niesman, I. R., Farquhar, M. G., and Insel, P. A. (2006) *J Biol Chem* **281**, 26391-26399

56. Clapham, D. E. (2003) *Nature* **426**, 517-524

57. Torok, Z., Crul, T., Maresca, B., Schutz, G. J., Viana, F., Dindia, L., Piotto, S., Brameshuber, M., Balogh, G., Peter, M., Porta, A., Trapani, A., Gombos, I., Glatz, A., Gungor, B., Peksel, B., Vigh, L., Jr., Csoboz, B., Horvath, I., Vijayan, M. M., Hooper, P. L., Harwood, J. L., and Vigh, L. (2014) *Biochim Biophys Acta* **1838**, 1594-1618

58. Parton, R. G., and Del Pozo, M. A. (2013) *Nat Rev Mol Cell Biol* **14**, 98-112

59. Johnson, C. M., Chichili, G. R., and Rodgers, W. (2008) *J Biol Chem* **283**, 29920-29928

60. Rohacs, T., and Nilius, B. (2007) *Pflugers Arch* **455**, 157-168

61. Kwan, H. Y., Huang, Y., and Yao, X. (2007) *Biochim Biophys Acta* **1772**, 907-914

62. Lee, H., and Caterina, M. J. (2005) *Pflugers Arch* **451**, 160-167

63. Moran, M. M., Xu, H. X., and Clapham, D. E. (2004) *Current opinion in neurobiology* **14**, 362-369

64. Talavera, K., Nilius, B., and Voets, T. (2008) *Trends in Neurosciences* **31**, 287-295

65. Damann, N., Voets, T., and Nilius, B. (2008) *Current Biology* **18**, R880-R889

66. Minke, B., and Cook, B. (2002) *Physiological Reviews* **82**, 429-472

67. Numazaki, M., Tominaga, T., Takeuchi, K., Murayama, N., Toyooka, H., and Tominaga, M. (2003) *Proc Natl Acad Sci U S A* **100**, 8002-8006

68. Gunthorpe, M. J., Benham, C. D., Randall, A., and Davis, J. B. (2002) *Trends in pharmacological sciences* **23**, 183-191

69. Numazaki, M., Tominaga, T., Toyooka, H., and Tominaga, M. (2002) *J Biol Chem* **277**, 13375-13378

70. Liu, M., Huang, W., Wu, D., and Priestley, J. V. (2006) *Eur J Neurosci* **24**, 1-6

71. Szoke, E., Borzsei, R., Toth, D. M., Lengl, O., Helyes, Z., Sandor, Z., and Szolcsanyi, J. (2010) *Eur J Pharmacol* **628**, 67-74

72. Picazo-Juarez, G., Romero-Suarez, S., Nieto-Posadas, A., Llorente, I., Jara-Oseguera, A., Briggs, M., McIntosh, T. J., Simon, S. A., Ladron-de-Guevara, E., Islas, L. D., and Rosenbaum, T. (2011) *J Biol Chem* **286**, 24966-24976

73. Goswami, C., Dreger, M., Jahnel, R., Bogen, O., Gillen, C., and Hucho, F. (2004) *J Neurochem* **91**, 1092-1103

74. Goswami, C., and Hucho, T. (2008) *FEBS J* **275**, 4684-4699

75. Ferrer-Montiel, A., Garcia-Martinez, C., Morenilla-Palao, C., Garcia-Sanz, N., Fernandez-Carvajal, A., Fernandez-Ballester, G., and Planells-Cases, R. (2004) *Eur J Biochem* **271**, 1820-1826

76. Sedgwick, S. G., and Smerdon, S. J. (1999) *Trends in Biochemical Sciences* **24**, 311-316

77. Engel, J., and Kammerer, R. A. (2000) *Matrix Biology* **19**, 283-288

78. Conway, S. J. (2008) *Chemical Society reviews* **37**, 1530-1545

79. Moiseenkova-Bell, V. Y., Stanciu, L. A., Serysheva, I. I., Tobe, B. J., and Wensel, T. G. (2008) *Proc Natl Acad Sci U S A* **105**, 7451-7455

80. Kedei, N., Szabo, T., Lile, J. D., Treanor, J. J., Olah, Z., Iadarola, M. J., and Blumberg, P. M. (2001) *J Biol Chem* **276**, 28613-28619

81. Kuzhikandathil, E. V., Wang, H., Szabo, T., Morozova, N., Blumberg, P. M., and Oxford, G. S. (2001) *J Neurosci* **21**, 8697-8706

82. Zhang, F., Liu, S., Yang, F., Zheng, J., and Wang, K. *J Biol Chem*

83. Caterina, M. J., Schumacher, M. A., Tominaga, M., Rosen, T. A., Levine, J. D., and Julius, D. (1997) *Nature* **389**, 816-824

84. Jordt, S. E., Tominaga, M., and Julius, D. (2000) *Proc Natl Acad Sci U S A* **97**, 8134-8139

85. Gavva, N. R., Klionsky, L., Qu, Y., Shi, L., Tamir, R., Edenson, S., Zhang, T. J., Viswanadhan, V. N., Toth, A., Pearce, L. V., Vanderah, T. W., Porreca, F., Blumberg, P. M., Lile, J., Sun, Y., Wild, K., Louis, J. C., and Treanor, J. J. (2004) *J Biol Chem* **279**, 20283-20295

86. Szallasi, A., Cortright, D. N., Blum, C. A., and Eid, S. R. (2007) *Nature reviews. Drug discovery* **6**, 357-372

87. Szallasi, A., and Blumberg, P. M. (1999) *Pharmacological reviews* **51**, 159-212

88. Johnson, D. M., Garrett, E. M., Rutter, R., Bonnert, T. P., Gao, Y. D., Middleton, R. E., and Sutton, K. G. (2006) *Mol Pharmacol* **70**, 1005-1012

89. Chung, M. K., Guler, A. D., and Caterina, M. J. (2008) *Nat Neurosci* **11**, 555-564

90. Voets, T., Droogmans, G., Wissenbach, U., Janssens, A., Flockerzi, V., and Nilius, B. (2004) *Nature* **430**, 748-754

91. Patapoutian, A., Peier, A. M., Story, G. M., and Viswanath, V. (2003) *Nat Rev Neurosci* **4**, 529-539

92. Koplas, P. A., Rosenberg, R. L., and Oxford, G. S. (1997) *J Neurosci* **17**, 3525-3537

93. Mandadi, S., Numazaki, M., Tominaga, M., Bhat, M. B., Armati, P. J., and Roufogalis, B. D. (2004) *Cell calcium* **35**, 471-478

94. Mandadi, S., Tominaga, T., Numazaki, M., Murayama, N., Saito, N., Armati, P. J., Roufogalis, B. D., and Tominaga, M. (2006) *Pain* **123**, 106-116

95. Stender, A. S., Marchuk, K., Liu, C., Sander, S., Meyer, M. W., Smith, E. A., Neupane, B., Wang, G., Li, J., Cheng, J. X., Huang, B., and Fang, N. (2013) *Chem Rev* **113**, 2469-2527

96. Braeckmans, K., Peeters, L., Sanders, N. N., De Smedt, S. C., and Demeester, J. (2003) *Biophys. J.* **85**, 2240-2252

97. Hassler, K., Leutenegger, M., Rigler, P., Rao, R., Rigler, R., Gosch, M., and Lasser, T. (2005) *Optics Express* **13**, 7415-7423

98. Axelrod, D. (2001) *J Biomed Opt* **6**, 6-13

99. Shimomura, O., Johnson, F. H., and Saiga, Y. (1962) *J Cell Comp Physiol* **59**, 223-239

100. Prasher, D. C., Eckenrode, V. K., Ward, W. W., Prendergast, F. G., and Cormier, M. J. (1992) *Gene* **111**, 229-233

101. Chalfie, M., Tu, Y., Euskirchen, G., Ward, W. W., and Prasher, D. C. (1994) *Science* **263**, 802-805

102. Inouye, S., and Tsuji, F. I. (1994) *FEBS letters* **341**, 277-280

103. Tsien, R. Y. (1998) *Annu Rev Biochem* **67**, 509-544

104. Matz, M. V., Fradkov, A. F., Labas, Y. A., Savitsky, A. P., Zaraisky, A. G., Markelov, M. L., and Lukyanov, S. A. (1999) *Nat Biotechnol* **17**, 969-973

105. Lukyanov, K. A., Chudakov, D. M., Fradkov, A. F., Labas, Y. A., Matz, M. V., and Lukyanov, S. (2006) *Methods Biochem Anal* **47**, 121-138

106. Miyawaki, A. (2005) *Neuron* **48**, 189-199

107. Stepanenko, O. V., Verkhusha, V. V., Kuznetsova, I. M., Uversky, V. N., and Turoverov, K. K. (2008) *Curr Protein Pept Sci* **9**, 338-369

108. Chudakov, D. M., Lukyanov, S., and Lukyanov, K. A. (2005) *Trends Biotechnol* **23**, 605-613

109. Shaner, N. C., Steinbach, P. A., and Tsien, R. Y. (2005) *Nat Methods* **2**, 905-909

110. Ormo, M., Cubitt, A. B., Kallio, K., Gross, L. A., Tsien, R. Y., and Remington, S. J. (1996) *Science* **273**, 1392-1395

111. Vinkenborg, J. L., Evers, T. H., Reulen, S. W., Meijer, E. W., and Merkx, M. (2007) *Chembiochem : a European journal of chemical biology* **8**, 1119-1121

112. Niwa, H., Inouye, S., Hirano, T., Matsuno, T., Kojima, S., Kubota, M., Ohashi, M., and Tsuji, F. I. (1996) *Proceedings of the National Academy of American Sciences* **93**, 13617-13622

113. Heim, R., Prasher, D. C., and Tsien, R. Y. (1994) *Proc. Natl. Acad. Sci. U S A* **91**, 12501-12504

114. Wachter, R. M. (2007) *Accounts of chemical research* **40**, 120-127

115. Palm, G. J., and Wlodawer, A. (1999) *Methods in enzymology* **302**, 378-394

116. Bizzarri, R., Nifosi, R., Abbruzzetti, S., Rocchia, W., Guidi, S., Arosio, D., Garau, G., Campanini, B., Grandi, E., Ricci, F., Viappiani, C., and Beltram, F. (2007) *Biochemistry* **46**, 5494-5504

117. Chattoraj, M., King, B. A., Bublitz, G. U., and Boxer, S. G. (1996) *Proceedings of the National Academy of American Sciences* **93**, 8362-8367

118. Lossau, H., Kummer, A., Heinecke, R., PollingerDammer, F., Kompa, C., Bieser, G., Jonsson, T., Silva, C. M., Yang, M. M., Youvan, D. C., and MichelBeyerle, M. E. (1996) *Chem Phys* **213**, 1-16

119. Morise, H., Shimomura, O., Johnson, F. H., and Winant, J. (1974) *Biochemistry* **13**, 2656-2662

120. Patterson, G. H., Knobel, S. M., Sharif, W. D., Kain, S. R., and Piston, D. W. (1997) *Biophys. J.* **73**, 2782-2790

121. McAnaney, T. B., Park, E. S., Hanson, G. T., Remington, S. J., and Boxer, S. G. (2002) *Biochemistry* **41**, 15489-15494

122. Voityuk, A. A., Michel-Beyerle, M. E., and Rosch, N. (1998) *Chem Phys* **231**, 13-25

123. Bonsma, S., Purchase, R., Jezowski, S., Gallus, J., Konz, F., and Volker, S. (2005) *Chemphyschem* **6**, 838-849

124. Elsliger, M. A., Wachter, R. M., Hanson, G. T., Kallio, K., and Remington, S. J. (1999) *Biochemistry* **38**, 5296-5301

125. Bizzarri, R., Nifosi, R., Abbruzzetti, S., Rocchia, W., Guidi, S., Arosio, D., Garau, G., Campanini, B., Grandi, E., Ricci, F., Viappiani, C., and Beltram, F. (2007) *Biochemistry* **46**, 5494-5504

126. Wachter, R. M., Elsliger, M. A., Kallio, K., Hanson, G. T., and Remington, S. J. (1998) *Structure* **6**, 1267-1277

127. Bizzarri, R., Serresi, M., Luin, S., and Beltram, F. (2009) *Anal. Bioanal. Chem.* **393**, 1107-1122

128. Bizzarri, R., Arcangeli, C., Arosio, D., Ricci, F., Faraci, P., Cardarelli, F., and Beltram, F. (2006) *Biophys. J.* **90**, 3300-3314

129. Arosio, D., Garau, G., Ricci, F., Marchetti, L., Bizzarri, R., Nifosi, R., and Beltram, F. (2007) *Biophys. J.* **93**, 232-244

130. Arosio, D., Ricci, F., Marchetti, L., Gualdani, R., Albertazzi, L., and Beltram, F. (2010) *Nat Methods* **7**, 516-518

131. Kuner, T., and Augustine, G. J. (2000) *Neuron* **27**, 447-459

132. Merzlyak, E. M., Goedhart, J., Shcherbo, D., Bulina, M. E., Shcheglov, A. S., Fradkov, A. F., Gaintzeva, A., Lukyanov, K. A., Lukyanov, S., Gadella, T. W., and Chudakov, D. M. (2007) *Nat Methods* **4**, 555-557

133. (!!! INVALID CITATION !!!)

134. Gadella, T. W. (ed) (2008) *FRET and FLIM Techniques*, Elsevier, Amsterdam, The Netherlands

135. Parson, W. W. (2007) *Modern Optical Spectroscopy*, 1st ed., Springer-Verlag, Berlin

136. Valeur, B. (2001) *Molecular Fluorescence: Principles and Applications*, 1st ed., Wiley-VCH, Weinheim

137. Lakowicz, J. R. (ed) (1999) *Principles of Fluorescence Spectroscopy*, Vol.

, Kluwer Academic/Plenum, New York

138. Lakowicz, J. R. (2006) *Principles of Fluorescence Spectroscopy*, 3rd ed., Springer Science, New York, USA

139. Padilla-Parra, S., and Tramier, M. (2012) *Bioessays* **34**, 369-376

140. Jares-Erijman, E. A., and Jovin, T. M. (2003) *Nature Biotechnology* **21**, 1387-1395

141. Shaner, N. C., Campbell, R. E., Steinbach, P. A., Giepmans, B. N., Palmer, A. E., and Tsien, R. Y. (2004) *Nat Biotechnol* **22**, 1567-1572

142. Patterson, G. H., Knobel, S. M., Sharif, W. D., Kain, S. R., and Piston, D. W. (1997) *Biophys J* **73**, 2782-2790

143. Albertazzi, L., Arosio, D., Marchetti, L., Ricci, F., and Beltram, F. (2009) *Photochem Photobiol* **85**, 287-297

144. Bollimuntha, S., Cornatzer, E., and Singh, B. B. (2005) *Vis Neurosci* **22**, 163-170

145. Storti, B., Bizzarri, R., Cardarelli, F., and Beltram, F. (2012) *J Biol Chem* **287**, 7803-7811

146. Lainez, S., Valente, P., Ontoria-Oviedo, I., Estevez-Herrera, J., Camprubi-Robles, M., Ferrer-Montiel, A., and Planells-Cases, R. (2010) *FASEB J* **24**, 1958-1970

147. Goswami, C., Hucho, T. B., and Hucho, F. (2007) *J Neurochem* **101**, 250-262

148. Goswami, C., Schmidt, H., and Hucho, F. (2007) *Febs J* **274**, 760-772

149. Gallego-Sandin, S., Rodriguez-Garcia, A., Alonso, M. T., and Garcia-Sancho, J. (2009) *J Biol Chem* **284**, 32591-32601

150. Toth, A., Wang, Y., Kedei, N., Tran, R., Pearce, L. V., Kang, S. U., Jin, M. K., Choi, H. K., Lee, J., and Blumberg, P. M. (2005) *Life Sci* **76**, 2921-2932

151. Goswami, C., Dreger, M., Otto, H., Schwappach, B., and Hucho, F. (2006) *J Neurochem* **96**, 254-266

152. Sanz-Salvador, L., Andres-Borderia, A., Ferrer-Montiel, A., and Planells-Cases, R. (2012) *J Biol Chem* **287**, 19462-19471

153. Parton, R. G., and Howes, M. T. (2010) *J Cell Biol* **191**, 439-441

154. Murata, T., Lin, M. I., Stan, R. V., Bauer, P. M., Yu, J., and Sessa, W. C. (2007) *Journal of Biological Chemistry* **282**, 16631-16643

155. Brownlow, S. L., and Sage, S. O. (2005) *Thromb Haemost* **94**, 839-845

156. Simons, K., and Toomre, D. (2000) *Nat Rev Mol Cell Biol* **1**, 31-39

157. Bolte, S., and Cordelieres, F. P. (2006) *J Microsc* **224**, 213-232

158. Abbruzzetti, S., Bizzarri, R., Luin, S., Nifosi, R., Storti, B., Viappiani, C., and Beltram, F. (2010) *Photochem Photobiol Sci* **9**, 1307-1319

159. Cheng, W., Yang, F., Takanishi, C. L., and Zheng, J. (2007) *J Gen Physiol* **129**, 191-207

160. Wiseman, P. W., Brown, C. M., Webb, D. J., Hebert, B., Johnson, N. L., Squier, J. A., Ellisman, M. H., and Horwitz, A. F. (2004) *J Cell Sci* **117**, 5521-5534

161. Hebert, B., Costantino, S., and Wiseman, P. W. (2005) *Biophys. J.* **88**, 3601-3614

162. Issa, A. M., Phillips, K. A., Van Bebber, S., Nidamarthy, H. G., Lasser, K. E., Haas, J. S., Alldredge, B. K., Wachter, R. M., and Bates, D. W. (2007) *Current drug safety* **2**, 177-185

163. Kim, S. A., Heinze, K. G., and Schwille, P. (2007) *Nat Methods* **4**, 963-973

164. Nagy, A., Wu, J., and Berland, K. M. (2005) *J Biomed Opt* **10**, 44015

165. Hess, S. T., Huang, S., Heikal, A. A., and Webb, W. W. (2002) *Biochemistry* **41**, 697-705

166. Petersen, N. O., Hoddelius, P. L., Wiseman, P. W., Seger, O., and Magnusson, K. E. (1993) *Biophys J* **65**, 1135-1146

167. Kolin, D. L., and Wiseman, P. W. (2007) *Cell Biochem Biophys* **49**, 141-164

168. Wiseman, P. W., Squier, J. A., Ellisman, M. H., and Wilson, K. R. (2000) *J Microsc* **200**, 14-25

169. Wheeler, D., Sneddon, W. B., Wang, B., Friedman, P. A., and Romero, G. (2007) *J Biol Chem* **282**, 25076-25087

170. Lippincott-Schwartz, J., Snapp, E., and Kenworthy, A. (2001) *Nat Rev Mol Cell Biol* **2**, 444-456

171. Liao, M., Cao, E., Julius, D., and Cheng, Y. (2013) *Nature* **504**, 107-112

172. Cao, E., Liao, M., Cheng, Y., and Julius, D. (2013) *Nature* **504**, 113-118

173. Runnels, L. W., and Scarlata, S. F. (1995) *Biophys. J.* **69**, 1569-1583

174. Levitt, J. A., Matthews, D. R., Ameer-Beg, S. M., and Suhling, K. (2009) *Current opinion in biotechnology* **20**, 28-36

175. Chan, F. T. S., Kaminski, C. F., and Schierle, G. S. K. (2011) *Chemphyschem* **12**, 500-509

176. Bader, A. N., Hoetzl, S., Hofman, E. G., Voortman, J., van Bergen en Henegouwen, P. M., van Meer, G., and Gerritsen, H. C. (2011

) *Chemphyschem* **12**, 475-483

177. Swaminathan, R., Hoang, C. P., and Verkman, A. S. (1997) *Biophys. J.* **72**, 1900-1907

178. Sharma, P., Varma, R., Sarasij, R. C., Ira, Gousset, K., Krishnamoorthy, G., Rao, M., and Mayor, S. (2004) *Cell* **116**, 577-589

179. Patterson, G. H., Piston, D. W., and Barisas, B. G. (2000) *Anal Biochem* **284**, 438-440

180. Chen, Y., Muller, J. D., Ruan, Q., and Gratton, E. (2002) *Biophys. J.* **82**, 133-144

181. Nagy, P., Claus, J., Jovin, T. M., and Arndt-Jovin, D. J. (2010) *Proc Natl Acad Sci U S A* **107**, 16524-16529

182. Ross, J. A., Digman, M. A., Wang, L., Gratton, E., Albanesi, J. P., and Jameson, D. M. (2011) *Biophys J* **100**, L15-17

183. Digman, M. A., Dalal, R., Horwitz, A. F., and Gratton, E. (2008) *Biophys. J.* **94**, 2320-2332

184. Ossato, G., Digman, M. A., Aiken, C., Lukacsovich, T., Marsh, J. L., and Gratton, E. (2010

) *Biophys J* **98**, 3078-3085

185. Gal, J. S., Morozov, Y. M., Ayoub, A. E., Chatterjee, M., Rakic, P., and Haydar, T. F. (2006) *J Neurosci* **26**, 1045-1056

186. Di Rienzo, C., Gratton, E., Beltram, F., and Cardarelli, F. (2013) *Proc Natl Acad Sci U S A*

187. Di Rienzo, C., Gratton, E., Beltram, F., and Cardarelli, F. (2013) *Proc Natl Acad Sci U S A* **110**, 12307-12312

188. Anderson, R. G., and Jacobson, K. (2002) *Science* **296**, 1821-1825

189. Kohler, S., Schaller, V., and Bausch, A. R. (2011) *PLoS One* **6**

190. Slotte, J. P. (2013) *Progress in lipid research* **52**, 424-437

191. Pelkmans, L., Kartenbeck, J., and Helenius, A. (2001) *Nature cell biology* **3**, 473-483

192. Ries, J., Chiantia, S., and Schwille, P. (2009) *Biophys J* **96**, 1999-2008

193. Mundy, D. I., Machleidt, T., Ying, Y. S., Anderson, R. G., and Bloom, G. S. (2002) *J Cell Sci* **115**, 4327-4339

194. Schwille, P., Korlach, J., and Webb, W. W. (1999) *Cytometry* **36**, 176-182

195. Wu, J., and Berland, K. M. (2008) *Biophys J* **95**, 2049-2052

196. Betzig, E., Patterson, G. H., Sougrat, R., Lindwasser, O. W., Olenych, S., Bonifacino, J. S., Davidson, M. W., Lippincott-Schwartz, J., and Hess, H. F. (2006) *Science* **313**, 1642-1645

197. Hess, S. T., Girirajan, T. P., and Mason, M. D. (2006) *Biophys. J.* **91**, 4258-4272

198. Dickson, R. M., Cubitt, A. B., Tsien, R. Y., and Moerner, W. E. (1997) *Nature* **388**, 355-358

199. Sinnecker, D., Voigt, P., Hellwig, N., and Schaefer, M. (2005) *Biochemistry* **44**, 7085-7094

200. Nifosi, R., Ferrari, A., Arcangeli, C., Tozzini, V., Pellegrini, V., and Beltram, F. (2003) *Journal of Physical Chemistry B* **107**, 1679-1684

201. McAnaney, T. B., Zeng, W., Doe, C. F., Bhanji, N., Wakelin, S., Pearson, D. S., Abbyad, P., Shi, X., Boxer, S. G., and Bagshaw, C. R. (2005) *Biochemistry* **44**, 5510-5524

202. Ando, R., Mizuno, H., and Miyawaki, A. (2004) *Science* **306**, 1370-1373

203. Bourgeois, D., and Adam, V. (2012) *IUBMB life* **64**, 482-491

204. Andresen, M., Wahl, M. C., Stiel, A. C., Grater, F., Schafer, L. V., Trowitzsch, S., Weber, G., Eggeling, C., Grubmuller, H., Hell, S. W., and Jakobs, S. (2005) *Proc. Natl. Acad. Sci. U S A* **102**, 13070-13074

205. Andresen, M., Stiel, A. C., Trowitzsch, S., Weber, G., Eggeling, C., Wahl, M. C., Hell, S. W., and Jakobs, S. (2007) *Proc. Natl. Acad. Sci. U S A* **104**, 13005-13009

206. Henderson, J. N., Ai, H. W., Campbell, R. E., and Remington, S. J. (2007) *Proc Natl Acad Sci U S A* **104**, 6672-6677

207. Adam, V., Lelimousin, M., Boehme, S., Desfonds, G., Nienhaus, K., Field, M. J., Wiedenmann, J., McSweeney, S., Nienhaus, G. U., and Bourgeois, D. (2008) *Proc. Natl. Acad. Sci. U S A* **105**, 18343-18348

208. Brakemann, T., Weber, G., Andresen, M., Groenhof, G., Stiel, A. C., Trowitzsch, S., Eggeling, C., Grubmuller, H., Hell, S. W., Wahl, M. C., and Jakobs, S. (2010) *J Biol Chem* **285**, 14603-14609

209. Faro, A. R., Carpentier, P., Jonasson, G., Pompidor, G., Arcizet, D., Demachy, I., and Bourgeois, D. (2011) *J Am Chem Soc* **133**, 16362-16365

210. Bizzarri, R., Serresi, M., Cardarelli, F., Abbruzzetti, S., Campanini, B., Viappiani, C., and Beltram, F. (2010) *J Am Chem Soc* **132**, 85-95

211. Jung, G., Wiehler, J., and Zumbusch, A. (2005) *Biophys J* **88**, 1932-1947

212. Voliani, V., Bizzarri, R., Nifosi, R., Abbruzzetti, S., Grandi, E., Viappiani, C., and Beltram, F. (2008) *J Phys Chem B* **112**, 10714-10722

213. Irie, M. (2000) *Chem Rev* **100**, 1685-1716

214. Andresen, M., Stiel, A. C., Folling, J., Wenzel, D., Schonle, A., Egner, A., Eggeling, C., Hell, S. W., and Jakobs, S. (2008) *Nat Biotechnol* **26**, 1035-1040

215. Bizzarri, R., Signore, G., Nifosi, R., Albertazzi, L., and Storti, B. (2010) *Biophysical Journal* **98**, 181a-181a

216. Brejc, K., Sixma, T. K., Kitts, P. A., Kain, S. R., Tsien, R. Y., Ormo, M., and Remington, S. J. (1997) *Proc Natl Acad Sci U S A* **94**, 2306-2311

217. Habuchi, S., Ando, R., Dedecker, P., Verheijen, W., Mizuno, H., Miyawaki, A., and Hofkens, J. (2005) *Proc. Natl. Acad. Sci. U S A* **102**, 9511-9516

218. Faro, A. R., Adam, V., Carpentier, P., Darnault, C., Bourgeois, D., and de Rosny, E. (2010) *Photoch Photobio Sci* **9**, 254-262

219. Moors, S. L. C., Michielssens, S., Flors, C., Dedecker, P., Hofkens, J., and Ceulemans, A. (2008) *J Chem Theory Comput* **4**, 1012-1020

220. Huang, B., Babcock, H., and Zhuang, X. W. (2010) *Cell* **143**, 1047-1058

221. Hell, S. W., and Wichmann, J. (1994) *Optics letters* **19**, 780-782

222. Klar, T. A., and Hell, S. W. (1999) *Optics letters* **24**, 954-956

223. Hofmann, M., Eggeling, C., Jakobs, S., and Hell, S. W. (2005) *Proc. Natl. Acad. Sci. U S A* **102**, 17565-17569

224. Gustafsson, M. G. (2005) *Proc Natl Acad Sci U S A* **102**, 13081-13086

225. Heintzmann, R., Jovin, T. M., and Cremer, C. (2002) *Journal of the Optical Society of America. A, Optics, image science, and vision* **19**, 1599-1609

226. Rust, M. J., Bates, M., and Zhuang, X. (2006) *Nat Methods* **3**, 793-795

227. Hell, S. W. (2007) *Science* **316**, 1153-1158

228. Dertinger, T., Colyer, R., Vogel, R., Enderlein, J., and Weiss, S. (2010) *Opt Express* **18**, 18875-18885

229. Geissbuehler, S., Dellagiacoma, C., and Lasser, T. (2011) *Biomed Opt Express* **2**, 408-420

230. Dedecker, P., Mo, G. C., Dertinger, T., and Zhang, J. (2012) *Proc. Natl. Acad. Sci. U S A* **109**, 10909-10914

231. Dertinger, T., Colyer, R., Iyer, G., Weiss, S., and Enderlein, J. (2009) *Proc Natl Acad Sci U S A* **106**, 22287-22292

232. Marriott, G., Mao, S., Sakata, T., Ran, J., Jackson, D. K., Petchprayoon, C., Gomez, T. J., Warp, E., Tulyathan, O., Aaron, H. L., Isacoff, E. Y., and Yan, Y. L. (2008) *Proceedings of the National Academy of Sciences of the United States of America* **105**, 17789-17794

233. Abbruzzetti, S., Bizzarri, R., Luin, S., Nifosi, R., Storti, B., Viappiani, C., and Beltram, F. (2010) *Photoch Photobio Sci* **9**, 1307-1319

234. Dedecker, P., Duwe, S., Neely, R. K., and Zhang, J. (2012) *J Biomed Opt* **17**, 126008

235. Zacharias, D. A., Violin, J. D., Newton, A. C., and Tsien, R. Y. (2002) *Science* **296**, 913-916

Acknowledgments

I should like to express my gratitude to the following people for the support and assistance during this research experience.

I wish to thank my advisor, Dr. Ranieri Bizzarri, for his support, enthusiasm and continuous optimism. Thanks to his experience he was able to let me through this work, and he always guided me in the right direction.

I would thank Prof. Fabio Beltram. He gave me the opportunity to work in the NEST laboratory and his precious suggestions stimulate me many times in improving my work.

I should like to thank Dr. Francesco Cardarelli and Carmine di Rienzo for their good friendship and for closely helping me in organizing the measurements and interpreting the experimental results. I gratefully acknowledge as well Paolo Faraci for his constant and precious technical support. During these years I am also indebted for help and stimulating discussions with Dr. Mariagrazia Di Luca, Prof. Cristiano Viappiani, and Dr. Michela Serresi.

I should say a big “thank you” to all the people I had the pleasure to meet at the NEST laboratory and who helped me in many ways: among these I should surely mention Dr. Fabrizio Salomone, Dr. Giovanni Signore, Gerardo Abbandonato, Gianmarco Ferri, Sara Macchi, Dr. Laura Marchetti, Dr. Antonella Battisti, Massimo Morandini, Dr. Teresa de Nadai, and Dr. Lorenzo Albertazzi.

Last but not the least, I would like to thank my family: my parents and my husband for their love, understanding, patience, and endless support.